

UNIVERSITY OF OKLAHOMA
GRADUATE COLLEGE

CATASTROPHIC PROCESS EVENT STRATIGRAPHY OF THE RADER MEMBER IN THE
DELAWARE BASIN

A THESIS
SUBMITTED TO THE GRADUATE FACULTY
In partial fulfillment of the requirements for the
Degree of
MASTER OF SCIENCE

By
TRAVIS WILLIAM MORELAND
Norman, Oklahoma
2018

CATASTROPHIC PROCESS EVENT STRATIGRAPHY OF THE RADER MEMBER IN THE
DELAWARE BASIN

A THESIS APPROVED FOR THE
CONOCOPHILLIPS SCHOOL OF GEOLOGY AND GEOPHYSICS

BY

Dr. John D. Pigott, Chair

Dr. Gerilyn Soreghan

Dr. Kulwadee L. Pigott

Dr. Shannon Dulin

© Copyright by TRAVIS WILLIAM MORELAND 2018
All Rights Reserved.

Acknowledgments

I would like to thank my family for all their support and advice over the past 23 years, which has allowed me to be the person I am today. An enormous thank you to Dr. Pigott as well for his guidance through this research and providing me an opportunity to continue my studies through graduate school. None of this research would have been possible without the previous work conducted by John Hornbuckle and other scientists who examined the Rader Member. Additionally, a huge thank you to Dr. Shi for agreeing to work alongside and perform the modeling through FUNWAVE-TVD, and the University of Delaware for the utilization of the *mills* HPC cluster, as well as the support staff of the *oscer* computer at OU. Thank you to Dr. Lynn Soreghan for her advice and insight toward the Guadalupe Mts. and allowing the use of her laboratory and collection of sieves to calibrate the MATLAB script, and to Daniel Buscombe who originally wrote the DGSA script.

Finally, to all the friends and peers who have provided support over the past few years both at the University of Oklahoma and as field assistance.

Abstract

The Bell Canyon Formation, Middle Rader Member, debris crops out in Guadalupe Mountains (along Highway 62, McKittrick Canyon and vicinity) revealing a Late Guadalupian catastrophic submarine debris slide. The formation contains reefal boundstone clasts, up to ~5m diameter, suspended in a sandy matrix. Above this deposit are two distinct hummocky cross-stratification (HCS) cosets. The overlying 0.3 to 0.5m amplitude and 2m strike wavelength HCS structures exhibit internally poorly graded gravel to silt-sized intraclasts and fossils within a muddy matrix, a vast difference from the lower mega-breccia.

Compared to modern sedimentological investigations which often study the relationships between hydrological parameters and observable bedforms (a forward problem) this investigation utilizes a variety of tools: LiDAR, XRF, thin sections, and grain-size analyses to determine the conditions during deposition from observed bedforms (an inverse problem). Paleobathymetric reconstructions and anoxic XRF indicators indicate that the commonly accepted processes of shallow water storm waves as the origin for these HCS beds is unlikely. Therefore, a deep-water, upper-flow-regime anti-dune interpretation for these bedforms appears to be more likely.

To test this hypothesis, a reconstruction of the decompacted isopachs of two Middle Rader debris slides was conducted for the northwest and eastern sides of the basin. Each of these slides contains an approximate minimum of 50 km³ of sediment. High Performance Computing (HPC) was conducted at the University of Delaware using NHWAVE to model the submarine slides and a fully nonlinear Boussinesq FUNWAVE-TVD program for the wave generation. The numerical models revealed these slides would have created a tsunami wave more than 30m in height with open sea speeds of 185mph, with the ability to generate Froude numbers exceeding

0.84 at water depth greater than 300m. Such hydrologic conditions are consistent with the formation of the observed deep-water anti-dune HCS.

Integrating the event stratigraphy of these results suggests that portions of the pre-fractured Capitan reef became partially exposed and unstable during a global and local sea level lowstand, possibly initiated by earthquakes caused by the Gondwanan-Lurassian collision to the south as likely triggers. Through outcrop analysis, a number of tsunamiites (HCS beds) are observed in the Rader Formation, suggesting multiple mass-failure events which generated tsunami waves and deep-water anti-dune HCS beds on the sea-floor bottom.

Table of Contents

Acknowledgments.....	iv
Abstract	v
Table of Contents.....	vii
List of Tables	ix
List of Figure	x
Chapter 1: Introduction	1
1.1 Problem Definition.....	1
1.2 Tectonic Setting	3
1.3 Geologic Setting.....	6
Chapter 2: Methods.....	8
2.1 Field Methods.....	8
2.2 XRF	9
2.2.1 Background and Field Collection	9
2.2.2 XRF Processing	10
2.3 Light Detection and Range (LiDAR).....	13
2.3.1 Background and Field Collection	13
2.3.2 Processing.....	15
2.4 Digital Grain Size Analysis.....	17
2.4.1 Background and Calibration	17
2.4.2 Processing.....	19
Chapter 3: Results and Observations	20
3.1 Road Cut Location.....	20
3.1.1 Road Cut Field Observations and Thin Section Analysis	20
3.1.2 Road Cut XRF Analysis	25
3.1.3 Road Cut LiDAR Observations	28
3.1.4 Road Cut Digital Grain Size Analysis.....	31
3.2 Creek Bed Location	34
3.2.1 Creek Bed Field Observations and Thin Section Analysis.....	34
3.2.2 Creek Bed XRF Analysis	38
3.2.3 Creek Bed LiDAR Observations.....	40

3.2.4 Creek Bed Digital Grain Size Analysis	42
3.3 Rader Ridge	44
3.3.1 Rader Ridge Field Observations and Thin Section Analysis	44
3.3.2 Rader Ridge XRF Analysis	46
3.3.3 Rader Ridge Distal Digital Grain Size Analysis	48
Chapter 4: Interpretations	49
4.1 Paleo-Redox Conditions	49
4.2 Depositional Processes of the Middle Rader Mega-Breccia	51
4.3 Depositional Processes of the Hummocky Cross Stratified (HCS) Beds.....	55
Chapter 5: Numerical FUNWAVE-TVD.....	61
5.1 Construction of the Paleo-Bathymetry	61
5.2 Static Modeling and Volumetrics of the Final Middle Rader Slides.....	63
5.3 FUNWAVE-TVD Background/Introduction	65
5.4 Inputs and Validations for the Dynamic FUNWAVE-TVD Model	66
5.5 Static Modeling and Volumetrics of the Starting Middle Rader Slides.....	69
5.6 Model Interpretations.....	69
5.6.1 Northwest Slide.....	70
5.6.2 Eastern Slide	74
5.7 Runup Deposit	77
Chapter 6: Petroleum Indications and Analog Reservoirs	79
Chapter 7. Conclusions	80
References	82
Appendix A.....	87

List of Tables

Table 1. A full list of elements the XRF device measured and the 13 total elements that were used in the study.	10
Table 2. The mathematical equations for deriving the four statistical moments. 4.1) the average grain size, 4.2) the grain comparison of largest and smallest grains, 4.3) the internal distribution of grains compared to the mean, 4.4) the concentration of grains compared to the total distribution. $\phi_{\#}$ being the grain size of the total population at the given percentage. (Folk, 1974)	20
Table 3. Thin sections from the Road Cut location to represent the stratigraphy.	23
Table 4. Thin sections from the Creek Bed location which represent the vertical stratigraphy from the Middle to Upper Rader Members.	37
Table 5. Thin sections from the Rader Ridge location which represent the vertical stratigraphy.	45
Table 6. The various dimensions for the northwest and eastern slides. Additional inputs are listed in Appendix A.	65

List of Figure

- Figure 1. A reconstruction of the collision of Laurasia and Gondwana during the Late Permian. The colliding plates created the super continent Pangea. At the collision point (along the equator), the Laurasian plate subducted under the Gondwana plate creating a volcanic arc south of the study area, indicated by the yellow triangles. The red box indicates the location of the following figure. Modified from Scholle, Goldstein, & Ulmer-scholle, 2007.....3**
- Figure 2. Closeup reconstruction of the colliding Laurasia and Gondwana plates. The Delaware Basin is outlined in purple. The basin starts to close off from its connection to the Panthalassa ocean during this time. To the east, the central basin platform separates the Delaware from the Midland basin outlined in green. To the south of the Permian Basin is the volcanic arc which resulted from the subduction of the Laurasian continent. (Blakey, 2013; Hornbuckle, 2017).....3**
- Figure 3. Location of the Rader Member is the 3rd member of the Bell Canyon sands. The Lower Rader Member is correlated to the G23/Y3 units while the Upper Rader Member is correlated to the G24/Y4 units. The upper Guadalupian strata was dated by Nicklen, 2011 to be 262.5 Ma. When compared to the sea level curve of Haq & Schutter (2008) places the interval in the middle of a large-scale sea-level fall. The red line shows the time of formation of the Rader Members in both the Nicklen correlations and the Haq sea level curve, and the blue line shows the location of the Middle Rader slide. Edited from (Haq & Schutter, 2008; Nicklen, Bell, & Huff, 2015).....6**
- Figure 4. An ideal cross section of the Delaware basin showing the coastal deposits on the left and the Delaware Basin deposits on the right. Moving from proximal to distal in the**

basin causes changes in the lithology during a constant time. The solid lines show approximate time horizons which show the correlation of formations at one time. The Yates Formation is the coastal deposit name correlating to the Capitan Limestone at the reef crest correlating to the Bell Canyon and Rader Member in the distal portions of the basin. (Modified from Fall & Olszewski, 2010).....6

Figure 5. Aerial view of the Guadalupe Mountains south east of McKittrick Canyon. The top left corner contains the Capitan Reef Limestone and the sample locations become more distal. The three study locations from proximal to distal are: Rader Ridge Distal, Creek Bed, and Road Cut. (Modified Google Earth and (Tang, 2015).8

Figure 6. A reconstruction of the sampling method modified from British Geological Survey (2010) website. The baseline shows the various scan locations, and red dots show the displacement and scattering of the reflectors on the outcrop wall which are used for correlating multiple scans together. (Hobbs et al., 2010).....13

Figure 7. The far-left graph shows the mineralogy distribution of the samples from the program by Dr. Pigott. The Si/Al graph shows detrital source of silica on the left (brown) and biogenic on the right (green). The right two graphs; V, Mo, and Mn*, show indicators for water redox conditions. Low Mn* (black) indicates anoxic conditions, while high Mn* (blue) indicates more oxic conditions. Mo tends to parallel TOC level suggested by Nance & Rowe, (2015) and Algeo & Rowe, (2012).25

Figure 8. A true color (top) and reflectivity scan (bottom) of the Road Cut location. Three distinct units are observed; Upper Rader Member (top left), the Middle Rader HCS beds (low reflectance), and Middle Rader mega-breccia (below HCS beds). Few limestone boulders can be noted in the true color scan and are masked in the reflectance due to

interference from the road (dust). The reflectance scans show that the HCS beds have a distinctly lower reflectance (-8.60dB to -3.2dB) than the surrounding strata (-0.45dB to 3.60dB).....28

Figure 9. The top image shows a true color scan of the lower portions of the Middle Rader, lower Bell Canyon sands, and Pinery Member's. Top of the lower Bell Canyon sands is indicated by the red line and the top of the Pinery indicated by the light blue line. The lower image shows the reflectance scan of the outcrop. The Pinery Member contains slightly lower reflective material than the lower Bell Canyon sands, and parallel bedding is noted in both the lower Bell Canyon and Pinery, while not in the Middle Rader Member. 30

Figure 10. The grain size distribution from the Road Cut location shows the four statistical moments from the Pinery, Middle Rader, Upper Rader, and upper Bell Canyon Members. The far-right shows thin section stocks under a black light to highlight the changes in abundance of carbonate clasts suspended in the sandy matrix.31

Figure 11. Photo of the three hummocky beds in the Creek Bed location. The top of hummocky bed 1 is indicated by the blue arrows, top of the second bed in green, and top of the third bed in yellow. Between the second and thrid hummocky beds is a thin dark shale. Above the HCS beds are turbidite deposits of the Upper Rader Member.34

Figure 12. The left image shows a cartoon reconstruction of the internal grading of the three hummocky beds. The middle image shows a comparison of relative grain sizes and grading from one bed to another. The right image is the gamma ray curve measured in the field using the hand-held RS-230. There is a gradual increase in GAPI moving from one bed to another, with the shale being the most radioactive.35

Figure 13. The far-left graph shows the mineralogy distribution of the samples from the program by Dr. Pigott. The Si/Al graph shows detrital source of silica on the left (brown) and biogenic on the right (green). The right two graphs; V, Mo, and Mn*, show indicators for water redox conditions. Low Mn* (black) indicates anoxic conditions, while high Mn* (blue) indicates more oxic conditions. Mo tends to parallel TOC level suggested by Nance & Rowe, (2015) and Algeo & Rowe, (2012).38

Figure 14. A true color (top) and reflectivity scan (bottom) of the Creek Bed location. Three sections are present within the scans: Middle Rader mega-breccia bottom half), Middle Rader HCS beds, and the Upper Rader Member (parallel beds in upper half). The HCS beds are marked by the first three beds above the massive mega-breccia, and grade into the Upper Rader Member. Reflectance values are skewed due to the location being an active creek. The outcrop is coated with a lining of mud/clay which has stunted the accuracy of all LiDAR scans except for the true color.40

Figure 15. The grain size distribution from the Creek Bed location showing the four statistical moments in the Middle Rader and Upper Rader Members. Moving from left to right the graphs are; XRF lithology, Mean Grain Size, Sorting, Skewness, and Kurtosis. The far-right shows thin section stocks under a black light to highlight the changes in abundance of carbonate clasts suspended in the sandy matrix.42

Figure 16. The far-left graph shows the mineralogy distribution of the samples from the program by Dr. Pigott. The Si/Al graph shows detrital source of silica on the left (brown) and biogenic on the right (green). The right two graphs; V, Mo, and Mn*, show indicators for water redox conditions. Low Mn* (black) indicates anoxic conditions, while high Mn* (blue) indicates more oxic conditions. Mo tends to parallel TOC level suggested by Nance &

Rowe, (2015) and Algeo & Rowe, (2012). The gray bars indicating sections of heavy cover where no measurements or observations could be obtained.46

Figure 17. The grain size distribution from Rader Ridge Distal showing the four statistical moments in the Lower Rader, Middle Rader and Upper Rader Members. Moving from left to right the graphs are; XRF lithology, Mean Grain Size, Sorting, Skewness, and Kurtosis. The far-right shows thin section stocks under a black light to highlight the changes in abundance of carbonate clasts suspended in the sandy matrix. The gray bars indicate sections of heavy cover where no measurements or observations could be obtained.48

Figure 18. During times of low sea levels, the basin is dominated by sediments which originate from a terrestrial source, deep water fan deposits. Once the sea levels rise, predominant sedimentation is through carbonate reef growth along the crest of the basin. In the deeper portions of the basin, an organic-rich hemipelagic drape (shale) is deposited as a continuous sheet, this is known as the maximum flooding surface. Once sea level falls again, the sedimentation is again dominated by a terrestrial source. Commonly fan-like turbidite gravity flows, and in rare conditions instability of the new carbonate slope can develop causing it to breakoff and slide into the basin. The figure is taken and constructed by Hornbuckle, 2017.51

Figure 19. The left image shows a Neptunian crack near Whites City, NM, with a rock hammer for scale. The right image, taken by Peter Scholle, shows the internal structure of the cement, post-fracturing (healing). Penny for scale. The cement growth pattern suggests that these fractures remain unstable up until the point that they are fully healed. The common orientation of these fractures is to the NE-SW, parallel to the strike of the Capitan reef.53

Figure 20. A comparison of the different variables that are accounted for when a portion of the basin breaks off and slides downward. As the sediment starts to move down a depression forms on the water surface directly above. In front of the slide water builds up and forms a long wave. Modified from (Grilli et al., 2017).....54

Figure 21. The upper three graphs show the decrease in a wave’s ability to disturb sediments on the ocean floor. The lower graph shows the wave amplitude required to agitate ocean floor sediments at increasing depths. To agitate sediments at 300m water depth, surface wave need to be stabilized at 15+m. (Weiss & Bahlburg, 2006).....57

Figure 22. The geomorphology of the Creek Bed showing the thickness of the individual Upper Rader Member Turbidite deposits. Each bed is roughly 5 to 10 cm thick. Photo taken by John Hornbuckle, 2016, and field book for scale.....59

Figure 23. A reconstructed paleo-bathymetry of the Delaware Basin just before the deposition of the Middle Rader Member. The surface was shifted so that the 0-crossing (bold line) aligned with the projected sea level during the Late Guadalupian as indicated by fossil, XRF, and other methods. A maximum water depth is -822 m, and a maximum height is 914 m above sea level. The western depression is the Diablo channel, and the southwest depression is the Hovey channel. The southern Marathon Orogenic Belt was trimmed to 914 m to reduce unnecessary computing.....61

Figure 24. The upper image is a PETREL model of the northwestern shelf slide (exposed Middle Rader Member) colored with the bulk volume of the deposit. The lower image is a PETREL model of the eastern CBP slide (subsurface Middle Rader Member) colored with the bulk volume of the deposit. Both slides have a core of sediment at the contact between the slope and toe of the basin.63

Figure 25. A PETREL reconstruction of the starting Middle Rader Member slides for both the northwestern shelf (upper) and eastern CBP (lower) portion of the basin. Both proximal flat regions are at an elevation of 25m. The shape of the starting slide locations was structured to resemble the final slide isopach thicknesses (figure 24).69

Figure 26. Four images of the propagation of the northwestern tsunami. The top left image shows the initial wave, the blue is the n from figure 25 and the red is the front wave. The top right image is from 1300 seconds (21 minutes), lower left from 2400 seconds (40 minutes), and the lower right at 3800 seconds (63 minutes). The red arrows on the lower right image show two reflection waves traveling in the opposite direction of the first wave. These smaller waves are only up to 10m tall.70

Figure 27. The maximum wave height of the tsunami generated from the northwest slide. The highest waves are located at the epicenter of the failure. The large waves in the southeast corner of the basin are a result of the rebound waves observed in figure 30.71

Figure 28. The location of Froude number greater than 0.84. The depth of these readings ranging from 0 to -300m. The right image is a close up behind the epicenter of the failure. Froude numbers are found to increase with decreasing water depth and reaching a maximum of 3.5.73

Figure 29. Four images of the propagation of the northwestern tsunami. The top left image shows the initial wave, the blue is the n from figure 25 and the red is the front wave. The top right image is from 800 seconds (13 minutes), lower left from 1300 seconds (21 minutes), and the lower right at 2200 seconds (36 minutes). The red arrows on the lower right image show two reflection waves traveling in the opposite direction of the first wave. These smaller waves are only up to 7m tall.74

Figure 30. The maximum wave height of the eastern slide. The tallest waves are found at the epicenter of the failure. along the opposite coast the wave height increases as the water shallows.....75

Figure 31. The location of Froude number greater than 0.84. The depth of these measurements ranged from 0 to -300m. The upper right image is a close up of the northwest coast, and flooding is observed over the island and Froude number up to 3.5 are found. The lower right image is a close up behind the epicenter of the failure. Froude numbers are found to increase with decreasing water depth and reaching a maximum of 3.5 as well.....76

Figure 32. An ideal model for the tsunami run-up deposit by (Shiki, Yamazaki, & Minoura, 2009). The Tna interval represents the first run-up wave going onshore, commonly having an erosional surface at the base. The Tnb section being the subsequent back-flow (return-flow) of sediment rich waters returning to the ocean. The Tnc and Tnd units being the slow down periods where the finer material settles out of suspension and form a thin bed.....77

Chapter 1: Introduction

1.1 Problem Definition

This study attempts an inverse analysis, and will posit the depositional conditions responsible for three hummocky cross stratification (HCS) beds observed directly above the Guadalupian Middle Rader Member mega-breccia slide of the Guadalupe Mountains (Texas) through an investigation of those strata immediately adjacent above and below, and test the hypothesis that the HCS beds are tsunamiites caused by the mass failure of the reef (Hornbuckle, 2017). To test the HCS beds and surrounding strata, four field techniques were utilized: Thin Sections, LiDAR, XRF, and Digital Grain Size Analysis (DGSA). Each of these four tools revealing a different aspect about the Rader Member.

Thin section analysis provided insight into the fossil assemblages within the carbonate clasts to determine where the sediments were originally sourced from. LiDAR scans showed the lateral continuity and vertical differences between each of the Members (Lower/Middle/Upper Rader). Through reflectance analysis changes in composition were highlighted which would not have been easily identified with XRF. XRF geochemical analysis utilized a suite of elements to determine the general source of the sediments and the depositional water redox conditions. Finally, grain size analysis allowed for more accurate observations of how the sediments were changing vertically at each study location.

The principles of sedimentology and hydrology are commonly integrated in ongoing studies of the relationship between flow velocity and water depth. The relationship between these two parameters has historically been explained via the Froude Number, a dimensionless value that constitutes the ratio of inertial and gravitational forces in an open channel (Chanson, 2004). Once sediments are integrated into the system, they form different bedforms according to the

complex interplay of physical forces (characterized by a given Froude Number) during deposition or transportation. As Froude Numbers increase from 0 to 1.0 (0 being completely still water and 1.0 being upper-flow-regime planar bedding), the observed bedforms change from lower flow regime planar beds to ripples to climbing ripples to sand waves to sand dunes. Once the Froude number equals 1.0, the upper-flow-regime takes over (van Rijn, 2018).

The transition from lower to upper flow regime marks the boundary between depositional and erosional water conditions. Froude Numbers >1.0 can destroy underlying bedforms in unlithified sediments. When the Froude Number continues to increase past 1.0, the bedforms transition into anti-dunes (Poos, 2011). Anti-dunes, which propagate upstream opposite water-flow direction are rarely preserved. As the Froude Numbers decrease from upper flow regime to ranges below 1.0, these bedforms will be eroded by the planar beds of the upper-flow-regime ($Fr=1$) (Mulder, Razin, & Faugeres, 2009). Further decreases result in the subsequent deposition of associated lower-flow-regime bedforms ($Fr<1.0$).

This method of study is a classic forward problem, an observed process (i.e. flowing water) results in physical changes (i.e. changing bedforms). When studying ancient rocks, the same processes must be determined in the reverse order (an inverse problem). The geologic record contains preserved bedforms from which the researcher must infer depositional conditions.

1.2 Tectonic Setting

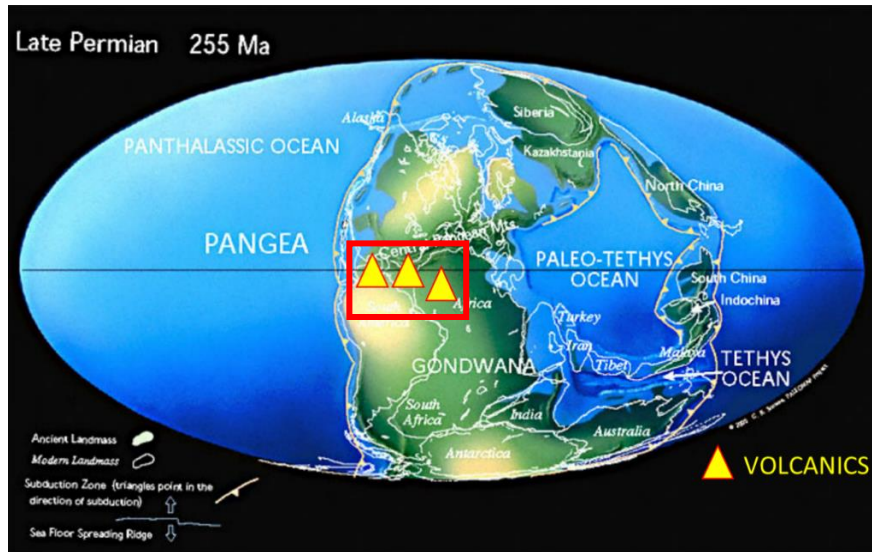


Figure 1. A reconstruction of the collision of Laurasia and Gondwana during the Late Permian. The colliding plates created the super continent Pangea. At the collision point (along the equator), the Laurasian plate subducted under the Gondwana plate creating a volcanic arc south of the study area, indicated by the yellow triangles. The red box indicates the location of the following figure. Modified from Scholle, Goldstein, & Ulmer-scholle, 2007.

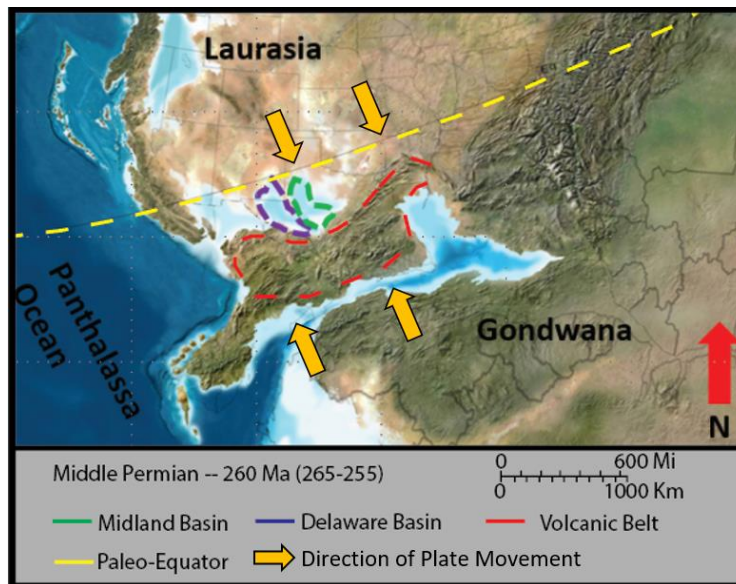


Figure 2. Closeup reconstruction of the colliding Laurasia and Gondwana plates. The Delaware Basin is outlined in purple. The basin starts to close off from its connection to the Panthalassa ocean during this time. To the east, the central basin platform separates the Delaware from the Midland basin outlined in green. To the south of the Permian Basin is the volcanic arc which resulted from the subduction of the Laurasian continent. (Blakey, 2013; Hornbuckle, 2017).

The tectonic evolution of the Delaware Basin has been modeled and detailed by Williams (2013) and Yalcin (2014). The major elements of its evolution are as follows: a regional depression developed in the Proterozoic along the edge of the North American craton (Hills, 1984); initial cooling and shrinking of the crust allowed for the accumulation of Early Ordovician sediments. This primary basin stretched toward the southeastern parts of New Mexico and West Texas (J. E. Adams, 1965), and allowed for the creation of a flat coastal plain that the early Ordovician sea occupied. Toward the middle of the Ordovician, crustal deformation created an approximately 350 mile-wide sag, which grew and became known as the Tobosa Basin (Hornbuckle, 2017). The Tobosa Basin was bounded by the Diablo Arch to the west (modern day Diablo Mountains) and the Texas Arch to the east (forming the eastern shelf of the Midland Basin). From the middle Ordovician through the Mississippian, passive tectonism dominated the region, such that the subsidence and subsequent deepening of the Tobosa Basin is attributed predominately to sediment loading and minor tectonism (J. E. Adams, 1965). The Mississippian marked a change from passive tectonism to compressional “wrenching” tectonism. The collision of Laurasian and Gondwanaian supercontinents drove Laurasian subduction (Figure 1). This subduction, initiated at the start of the Permian, caused large-scale deformation in the form of folding and faulting throughout the region and formed many of the other basins of this time (e.g. Anadarko Basin, Val Verde Basin, and others) (Hornbuckle, 2017). Consequently, the Delaware basin transitioned from a wrench basin into a foreland basin, separated from its sister basins by the recently uplifted central platform ridge, which in time would grow to be the Central Basin Platform of today. As such, the once unified Tobosa Basin, separated now by the central basin ridge, became subdivided into two separate sub-basins, the Delaware Basin to the west and Midland Basin to the East (Figure 2) (J. E. Adams, 1965). Together, these basins later became

known as the greater Permian Basin. Pre-existing planes of weakness from Proterozoic strata were exploited by the tectonic activity and resulted in Delaware Basin tilting approximately 5 degrees to the east. Many of the faults and folds of this region trend SE – NW, a result of the zipper shut of the collision zone.

Continued tectonism through the early Triassic oversaw the regional retreat of the Panthalassa ocean, and consequent subaerial exposure of the sediments and reefs, and eventual deposition of thick evaporite accumulations (i.e. Castille Formation). By the Late Triassic, regional tectonic sagging initiated further subsidence, though nothing as profound as that experienced during hitherto periods of active tectonism. From the Late Triassic through the Early Cretaceous, uplift-driven erosion removed large portions of the Permian sediments. In the middle of the Early Cretaceous, the Sevier orogeny culminated with the formation of the Sevier foreland basin (J. E. Adams, 1965). Subsequently, the Laramide uplift caused the erosional removal of much of those sediments associated with the Sevier orogeny, including sediments dating back to the Early Cretaceous. As such, over the course of the Delaware Basin's evolution, subsidence remained largely controlled by sediment loading with marked pulses of tectonic uplift (Williams, 2013; Yalcin, 2014).

1.3 Geologic Setting

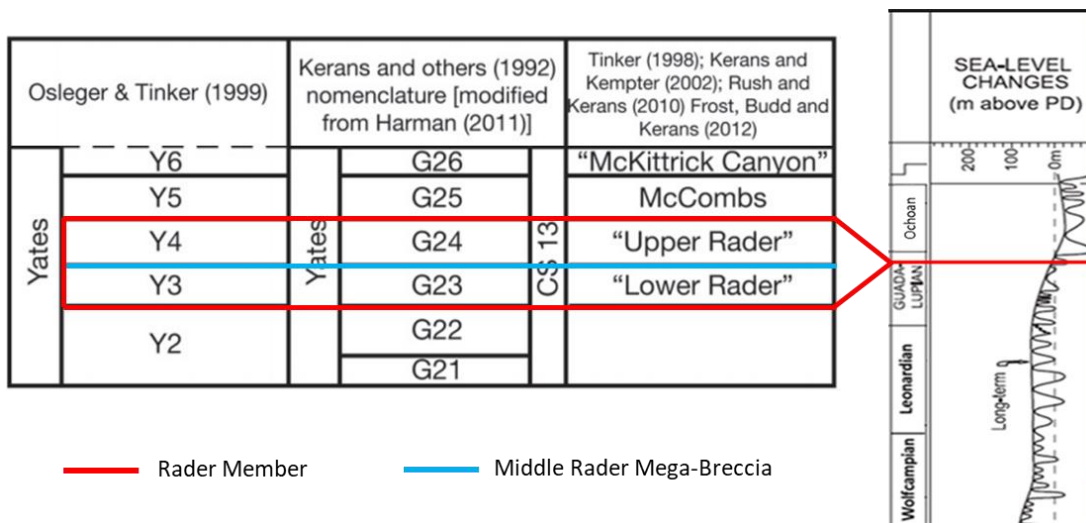


Figure 3. Location of the Rader Member is the 3rd member of the Bell Canyon sands. The Lower Rader Member is correlated to the G23/Y3 units while the Upper Rader Member is correlated to the G24/Y4 units. The upper Guadalupian strata was dated by Nicklen, 2011 to be 262.5 Ma. When compared to the sea level curve of Haq & Schutter (2008) places the interval in the middle of a large-scale sea-level fall. The red line shows the time of formation of the Rader Members in both the Nicklen correlations and the Haq sea level curve, and the blue line shows the location of the Middle Rader slide. Edited from (Haq & Schutter, 2008; Nicklen, Bell, & Huff, 2015).

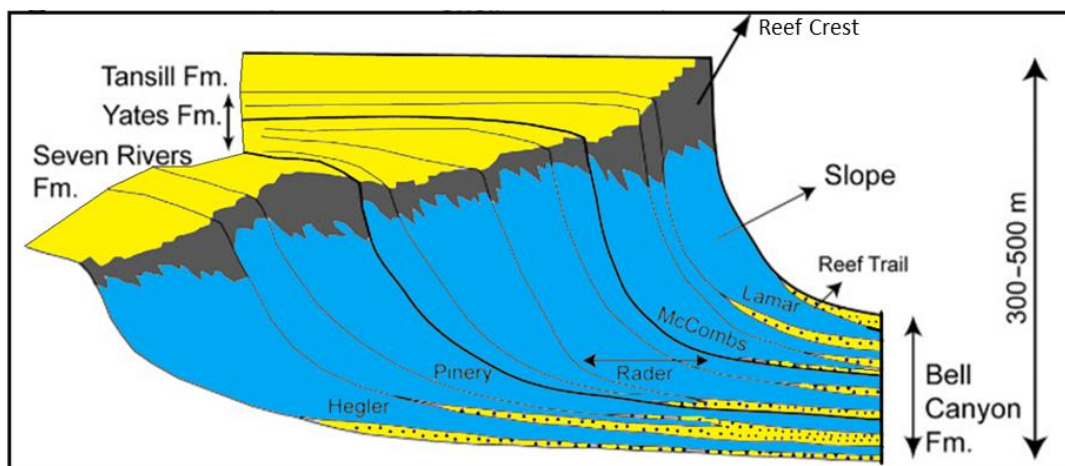


Figure 4. An ideal cross section of the Delaware basin showing the coastal deposits on the left and the Delaware Basin deposits on the right. Moving from proximal to distal in the basin causes changes in the lithology during a constant time. The solid lines show approximate time horizons which show the correlation of formations at one time. The Yates Formation is the coastal deposit name correlating to the Capitan Limestone at the reef crest correlating to the Bell Canyon and Rader Member in the distal portions of the basin. (Modified from Fall & Olszewski, 2010).

With the withdrawal of the Panthalassa ocean, the Delaware basin became isolated from normal oceanic circulation. Consequently, conditions favorable to subaqueous evaporitic deposition prevailed in the Delaware Basin with the resulting deposition of the world-renowned Castille evaporites. This extensive evaporite blanket largely prevented erosional processes associated with subaerial exposure, preserving much of the uppermost Permian strata. Of these strata, atypical deposits were identified within the Bell Canyon Formation, more specifically a basal unit composed of large (e.g. car-sized) carbonate boulders supported in sandy matrix, and an overlying unit encompassing two, possibly three hummocky beds. Collectively, these strata are known as the Middle Rader Member. Considering the control that such a fall in sea level has over slope stability, portions of the Capitan Reef complex consequently experienced structural deformation (i.e. Neptunian fractures). Such fractures occur in sections of the reef near Whites City, NM, and serve as an excellent example of what these features look like (Saller, 2013). Eventually, this deformation culminated in the *en masse* separation of reef section from the basin's margins that was ultimately recorded in the rock record as a mass transport complex manifesting as the mega-breccia of the Middle Rader Member (Hornbuckle, 2017).

The Rader Member is time equivalent to the Yates Formation (Nicklen et al., 2015). The Yates, as backreef deposits, may be understood as the primary source of Rader sediments. Of those Rader sediments, there are three main sub-members: 1) The Lower Rader Member, which is present in the proximal zone of the slope and unique for the bioturbations contained within thin laminations. The Lower Rader Member correlates to the G23 unit from Kerans (1992), and Y3 unit by Osleger & Tinker (1999). 2) The Middle Rader Member, which encompasses the mega-breccia/conglomerate, although that breccia presents solely in the toe of the slope, and the conglomerate in the basin margin. 3) The Upper Rader Member, which shares similarities with

the Lower Rader Member, yet has an increased siliciclastic component up section (Lawson, 1989). This component, correlated to G24 unit from Kerans et al., 1992, and Y4 unit by Osleger & Tinker, 2012 is indicative of persistent and increasing siliciclastic transport into the system. Underlying the Rader Member is a thin interval of Bell Canyon sands evidencing amalgamation surfaces delineating the Pinery Member.

Chapter 2: Methods

2.1 Field Methods

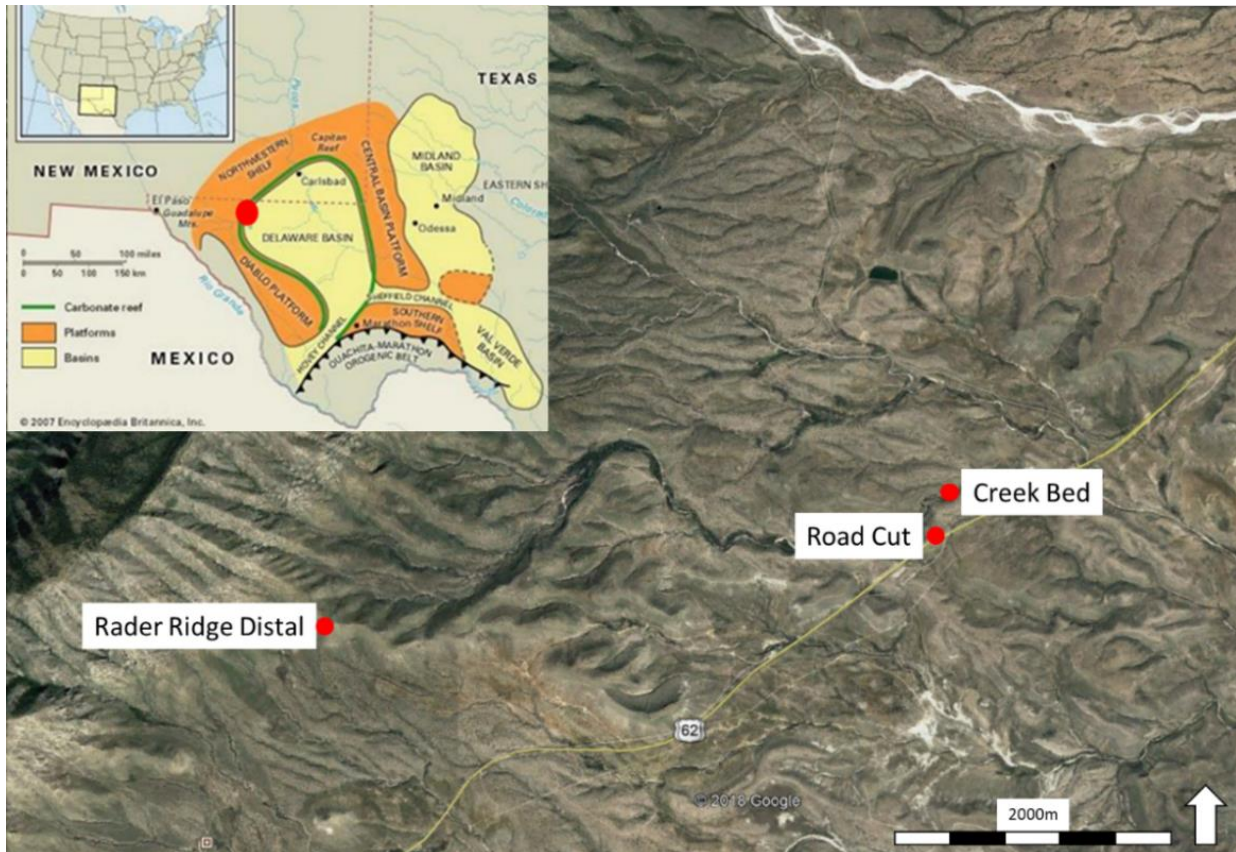


Figure 5. Aerial view of the Guadalupe Mountains south east of McKittrick Canyon. The top left corner contains the Capitan Reef Limestone and the sample locations become more distal. The three study locations from proximal to distal are: Rader Ridge Distal, Creek Bed, and Road Cut. (Modified Google Earth and (Tang, 2015).

Field research and observations were conducted at three locations near and around McKittrick Canyon in the Guadalupe Mountains (Figure 5). From distal to proximal the locations are as follows: Road Cut, Creek Bed, and Rader Ridge. A total of four measured sections were recorded by the previous researcher (Hornbuckle, 2017). Two at the Rader Ridge (proximal and distal), one at the Creek Bed, and one at the Road Cut locations. Additional observations were gathered in this study to aid in the analysis and to note changes from proximal to distal. In contrary to the previous studies, larger, more regional features were observed such as grain distributions proximal vs distal, and boulder abundance.

2.2 XRF

2.2.1 Background and Field Collection

A Thermo Scientific Niton XL3t Ultra Analyzer X-Ray Fluorescence gun was used to measure the elemental abundance of the multiple study areas and surrounding strata. A total of 133 samples from the Road Cut Rader Member, 19 samples from the Creek Bed, 208 samples from the combined Rader Ridge locations (164 from distal and 44 from the proximal area) were collected by John Hornbuckle throughout 2015-2016. Abundance data of 41 elements were measured using the XRF tool, 28 of these elements provided useful insight into the rocks lithologic composition and served as proxies for paleo-water conditions, while the other 13 elements not used were in low concentration or were whose proxies were already being accounted for. The full list of elements measured are as follows;

Table 1. A full list of elements the XRF device measured and the 13 total elements that were used in the study.

MEASURED ELEMENTS			ELEMENTS USED
Molybdenum (Mo)	Tungsten (W)	Scandium (Sc)	Molybdenum (Mo)
Zirconium (Zr)	Copper (Cu)	Potassium (K)	Zirconium (Zr)
Strontium (Sr)	Nickel (Ni)	Sulfur (S)	Strontium (Sr)
Uranium (U)	Cobalt (Co)	Barium (Ba)	Iron (Fe)
Rubidium (Rb)	Iron (Fe)	Antimony (Sb)	Manganese (Mn)
Thorium (Th)	Manganese (Mn)	Tin (Sn)	Chromium (Cr)
Lead (Pb)	Chromium (Cr)	Cadmium (Cd)	Vanadium (V)
Gold (Au)	Vanadium (V)	Palladium (Pd)	Titanium (Ti)
Selenium (Se)	Titanium (Ti)	Silver (Ag)	Magnesium (Mg)
Arsenic (As)	Aluminum (Al)	Niobium (Nb)	Silicon (Si)
Mercury (Hg)	Phosphorous (P)	Bismuth (Bi)	Calcium (Ca)
Zinc (Zn)	Silicon (Si)	Radium (Re)	Potassium (K)
Hafnium (Hf)	Chlorine (Cl)	Tantalum (Ta)	Sulfur (S)
Calcium (Ca)	Magnesium (Mg)		

These elements were chosen by their overall abundance among all the samples and locations and usefulness of determining paleo conditions. On average, the device measured each sample for 210 sec., cycling from; Main Range, High Range, Low Range, and Light Range. The Main, High, and Low Ranges ran for 30 seconds, the Light Range ran for 90 seconds, then the order repeated a second time completed the full 210 second reading (ThermoFisher, 2010). Each sample location is then recorded by the GPS and a small hand sample collected for future reference if needed.

2.2.2 XRF Processing

The use of whole rock inorganic geochemistry is a useful method to quickly analyze paleo-depositional conditions. This geochemistry study summarizes and will expand slightly on the work conducted by Hornbuckle (2017). The use of a suite of proxy elements, opposed to isolated proxy elements, prevents the misrepresentation of data. Multiple sources (Sageman &

Lyons, 2003; Turner, Molinares-blanco, & Slatt, 2015) suggest and encourage the use of multiple elemental proxies for investigation to prevent interpreting diagenetic features.

A program created by Dr. Pigott utilizes the elemental abundances in a rudimentary normative mineralogy assemblage. This program examines the abundance of Fe, S, Mg, Ca, K, Al, and Si to determine mineral proportions of gypsum, dolomite, calcite, quartz, potassium feldspar (Kspar), clay/mica, and pyrite (Pigott, Personal Communication). These minerals, along with other elements, were used as proxies for the depositional conditions.

Terrigenous or siliciclastic inputs are analyzed through their Si, Ti, and Zr elemental proxies, however, Si can be accumulated as detritus or through biogenic precipitation (Sageman & Lyons, 2003). To account for these two origins of Si, it must be used alongside Al in the Si/Al ratio in order to accurately determine its origin. Low Si/Al relating to a detrital source, and a high Si/Al ratio relating to a biogenic source of silica. Both Ti and Zr, are also immobile, meaning elevated amounts of Ti or Zr are indicative of a more terrigenous source (Turner et al., 2015). Declining Ti and Zr measurements generally are associated with retrogradational successions and an increase in these elements associated with progradational successions (Nance & Rowe, 2015); siliciclastic-dominated intervals represent times of low-stand deposition (Turner et al., 2015).

Biogenic carbonates contain a wide array of trace elements. P, Ca, Sr, Mg, and Mn are analyzed congruently to determine a systems carbonate influence, and differentiate the various carbonate minerals (Sageman & Lyons, 2003). Phosphate does not appear to contribute to the carbonate accumulations, due to such low concentrations in this study, but normally helps differentiate phosphatic zones from carbonate zones (Burgi et al., 1988). Magnesium is an important element to include in the carbonate elemental proxy suite to determine

calcite/aragonite from dolomite. Manganese was included in the carbonate suite as it shows covariance with Ca, Sr, and Mg (Crosby, 2015).

A literature study of (Pigott et al., 2007) and (Crosby, 2015) revealed that the paleo-redox conditions can be examined by the elemental suite of Mo, V, Co, Ni, Cu, and Mn*. The use of these trace metals proves useful due to their solubility in oxygenated (oxidizing) waters, and less soluble in oxygen depleted waters (reducing conditions) (Tribovillard et al., 2006). Variations in the natural abundance of V, Cr, U, and Mo provide insight into the oxygen content of the depositional waters (changes from anoxic to oxic) (Hornbuckle, 2017). Changes in the oxygen content can be a result of local factors, lack of circulation within the water column, or global changes, isolation of the basin causing the water column from being replenished. Organometallic complexes (OM) can be represented by the elements of Ni and Cu. Large abundances of Ni and Cu correspond to higher inputs of organic matter, while depleted Ni and Cu correspond to low amounts of organic matter (Tribovillard et al., 2006). Finally, the identification of high organic inputs can be observed by high concentrations of the element U (Pigott et al., 2007).

$$(1) \quad Mn^* = \log \left\{ \frac{Mn_{Sample} / Mn_{PAAAS}}{Fe_{Sample} / Fe_{PAAAS}} \right\}$$

As for the water conditions during the Rader deposition, most researchers agree that the basin during the deposition was anoxic (Fischer & Sarnthein, 1988; Lawson, 1989). This can be observed in the Mn^* proxy (eq 1) where higher values represent more oxic conditions while lower values represent less oxic conditions. Then within the siliciclastic dominated intervals (sandy matrix) show more anoxic trends, which again are obvious in the Mn^* proxy (Hornbuckle, 2017). Mn^* proxy used in Crosby (2015) normalizes the measured Fe and Mn

sample readings to *PAAS* values of the same elements, with negative results indicating anoxic conditions and positive values representing oxic conditions.

In determining paleowater conditions, Molybdenum and Vanadium can be used to indicate the redox conditions. Titanium and Zirconium are attributed typically to continentally derived sources, given that they are hard elements and insoluble. Calcium and Strontium are attributed to carbonate materials. Sr concentrate is a means to determine the difference in the calcite pseudomorphs (aragonite: Sr high, and high/low Mg calcite: Sr low) (Deer, Howie, & Zussman, 2013). Aluminum and Potassium generally form with clays and feldspars and can indicate amounts of weathering. A study by Nance and Rowe (2015) found that within the Permian Basin, the abundance of Mo resembles the general trend of total organic carbon (TOC). For this study, the Mo approximation of TOC will be used to examine trends without determining actual TOC values (Nance & Rowe, 2015).

2.3 Light Detection and Range (LiDAR)

2.3.1 Background and Field Collection

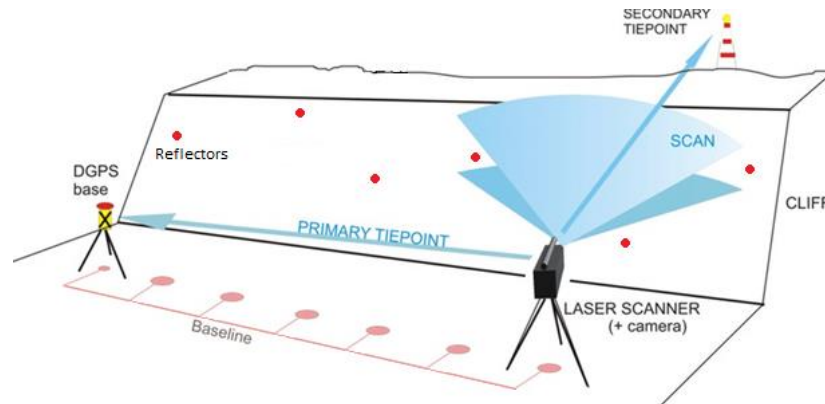


Figure 6. A reconstruction of the sampling method modified from British Geological Survey (2010) website. The baseline shows the various scan locations, and red dots show the displacement and scattering of the reflectors on the outcrop wall which are used for correlating multiple scans together. (Hobbs et al., 2010).

Imaging of the outcrops was acquired using a RIEGL VZ-400 3D terrestrial laser scanner (LiDAR) and associated Nikon D-800 camera. The equipment required includes the RIEGL VZ-400 3D terrestrial laser scanner, tripod, LiDAR battery, four car batteries, LiDAR reflectors, Nikon D100 camera, stool for laptop user, and a laptop with the RiSCAN PRO v2.3 data processor application installed. For data acquisitions, the LiDAR device uses a narrow wavelength infrared laser beam to illuminate the targeted outcrop. The device measures the two-way travel times and the vector ordinance of the beam to determine the distance and placement of the point data. The beams diminish in both amplitude and reflectance, with distance to the target, and are measured and recorded for each data point (RIEGL, 2013). This is repeated for each point of data and these points are stored in a point cloud within the laptop. The Light Detection and Range scanner (LiDAR) was used to scan the two study areas a total of 30 times (21 scans for the road cut, and 9 scans in the creek bed). At each of the 30 scan locations two scans were performed, a 360-degree scan with a resolution of 0.020 degrees and a laser pulse repetition rate (PRR) of 300kHz. A refined high-resolution scan of 0.005 degrees, and PRR of 300kHz was used for the second scan (Hornbuckle, 2017). The first 360 degree scan is used to position the LiDAR relative to the previous scan location and pick up the reflectors on the outcrop wall. The reflectors are 5 cm flat stickers attached to the wall of the outcrops. A minimum of three reflectors are used to stitch two scans together on either side of the LiDAR, six total reflectors per scan (RIEGL, 2013), figure 6 shows a reconstruction of the field setup. This allowed for a three-dimensional triangulation for both the left and right sides of the scan and allow for accurate positioning from one scan location to another. On average the first 360 scan takes roughly 40 minutes to complete, while the higher resolution scans took roughly one hour each.

After completion of the coarse scan, the Nikon camera takes pictures of the region to color the newly obtained point cloud data. Before acquisition of the higher resolution scan, the user manually identifies the location of the reflectors that were previously attached to the walls of the outcrop through the laptop. The LiDAR then performs a high-resolution scan of these locations to narrow down the position of the device.

The second scan, a high-resolution scan, is obtained in the same location as the coarse 360 scan. This is used to focus on the outcrop wall and avoid the non-target areas, designated by the user. Since the first 360 scan positioned the LiDAR with respect to the outcrop, the number of reflectors obtained in the fine scan is not a requirement for positioning anymore. Once the LiDAR completes the second scan and uploads the data to the laptop, the whole station is disassembled and relocated to the next scan position. After the completion of all scan locations, the data are merged into one large data set and retrieval of the field reflectors commences. For additional information on the environmental conditions and setup parameters consult “*Process Sedimentology of the Guadalupian Rader Limestone Delaware Basin*, John Hornbuckle, 2017”.

2.3.2 Processing

The raw LiDAR data is visualized using RiScan Pro v2.3.2 as point cloud data. Each point is located on either a global coordinate system (GPS) or a local scanner’s own coordinate system (SOCS) (RIEGL, 2012). Each scan is imported individually into the viewing window, so that the data can be cropped leaving only the targeted outcrop while reducing the file size.

Each data point is assigned numerous values such as amplitude and reflectance. Amplitude is defined as the maximum extent of a vibration or oscillation, measured from the position of equilibrium (RIEGL, 2012). For this case this is the amplitude of the echo returning

to the LiDAR after rebounding from the outcrop (RIEGL, 2013). The amplitude attribute contains a number of parameters, including the emitted laser pulse peak power and the receiver aperture, but also including point parameters like the target's reflectance and range (RIEGL, 2012). Reflectance is a target related property and is defined as the measure of the proportion of light or other radiation striking a surface that is reflected off it (RIEGL, 2012). The reflectance is the ratio of the amplitude of that target to the amplitude of a white flat target at the same range, oriented orthonormal to the beam axis with a size in excess of the laser footprint (RIEGL, 2012).

Both amplitude and reflectance have setbacks. For amplitude, the distance from a target can change the value received, increased distance results in lower amplitude. While for reflectance, the intersection angle with the outcrop can impact the received value (Adams & Filice, 1967). Previous studies by (Giddens, 2016) and (Garrett, 2015) show that reflectance provides a greater ability to analyze lithology and mineralogy from outcrop than the amplitude measurements. Filtering the LiDAR data after acquisition involves sifting through the point clouds to remove isolated points and error data. Generally, this could be done by examining the various echoes the data contains. Within the data, four echoes are present: single targets, first targets, other targets, and last targets. Typically, the single target is the targeted interval, the group of points that can form a continuous surface in four direction. The first targets are the points which appear before the bulk of the data. These include bugs, vegetation, and other objects that interfere with the beam before reaching the main target. Other targets are points which do not have a continuous surface in three directions, for example the edges of rocks. This echo highlights fractures well. Finally, the Last targets are points of error data that do not match the two-way travel time that the surrounding data contains (RIEGL, 2013).

Once the noise has been removed a terrain filter is applied to remove the unwanted vegetation from the target area. Finally, to reduce the point cloud size an octree filter is added to the coarse scan (360 degree) to provide a more gridded distribution of the points (RIEGL, 2013).

2.4 Digital Grain Size Analysis

2.4.1 Background and Calibration

The grain size calculations were conducted using a MATLAB code (Calibrated Digital Grain Size Analysis) based on Daniel Buscombe Digital Grain Size Analysis script created while with the USGS (Buscombe, 2013). The script uses an image of the sample to calculate the relative grain size. This is done by measuring the number of pixels that are present within one millimeter of the image, this calibrates the image and converts the outputs from pixels to millimeters. Once calibrated the image is converted to a gray scale color bar to minimize the depth changes caused by natural grain stacking offset (Buscombe, 2013). For a more precise measurement a region of interest can be selected on these images for analysis. A rule of thumb from Buscombe suggests that there be roughly 1000 grains visible in the selected region of interest (the more grains, the more accurate the reading) (Buscombe, 2013). To analyze the image, each row of pixels is analyzed separately. The script treats these rows of pixels like wavelets, peaks being pixels of high amplitude (grains) and troughs being pixels of low amplitude (non-grain). A mother wavelet equation is used to identify these grain boundaries and the distance between them (Buscombe, 2013).

$$(2) \text{ Mother Wavelet } W_n(s) = \sqrt{\frac{dy}{s}} \sum_{n'=0}^{n-1} \gamma_n \psi_0^* \left[\frac{(n' - n)dy}{s} \right]$$

Where Δy is the pixel spacing in terms of γ_n (one pixel), (n, s) is the expression of the 2D parameters of spacing. The Mother Wavelet (2) is the summation of a pixel's amplitude, times the displacement from the source (image left edge), then the wavelet transform is weighted by a single pixel (average pixel amplitude) (Buscombe, 2013).

Before the studied samples could be analyzed, the DGSA script needed to be calibrated to ensure its accuracy. To do so, a series of four samples from various locations (Trout, New Foundland; Dry Tortugas, Florida; Eritrea, Red Sea; and Algeria, sand dunes) were sieved and weighed. The four samples were weighed to get a starting weight, then were imaged using a DinoLite camera using 20x magnification. The samples were then placed in a Gilson Company hand operated sieve shaker and shaken for 15 minutes (Folk standard (Folk, 1974)). Once sieved, the individual pans were weighed again to calculate the percent of the sample each sieve contained. The separated sieve samples were imaged again using the same parameters as before, 20x magnification. The sieved images were then processed through the DGSA script and a millimeter pixel ratio of 0.0144mm/pxl was used. The output measurements were then converted to phi to get a normal distribution of the data. The ϕ (phi) scale is the standard used when examining grain size distribution. The more negative a grain is on the scale, the larger diameter it has, while the more positive a grain is the smaller it is. The 0 crossing is equal to 1mm.

The DGSA outputs were compared to the measured sieve results to determine a correction factor for the DGSA script:

$$(3) \quad CDGSA = 0.6787 * (DGSA) + 0.0153$$

2.4.2 Processing

Twentytwo samples were gathered and made into thin sections from the Road Cut location, 9 from the Creek Bed location, and 4 from the Rader Ridge location. These were imaged using the DinoLite digital microscope and processed using the DGSA script. Each sample was imaged in six different matrix locations to provide an accurate average while moving vertically up the outcrop. The matrix was defined as the grains holding up, and suspending, the larger carbonate reefal material, and did not include the actual clasts.

From the corrected DGSA (CDGSA) script the four statistical moments can be calculated; mean grain size, sorting, skewness, and kurtosis. Mean grain size (4.1) is defined as the average diameter of the grain within a sample. Typically, the grain size of the sample is controlled by the grain size of the source material and the energy which transports the sediments (Folk, 1974). If a location is only sourced by sediments from 2-3 ϕ , then the observed sediments will be within 2-3 ϕ .

The second moment, sorting (4.2), is defined as the distribution and range of the different grain diameters (Folk, 1974). The main controlling factors again being the source material, time, and transport energy. Source material is relating to the original sediments that the deposit is composed from. Time being the length of disturbance by waves or other medium. Periodic waves typically being more poorly sorted while continuous waves or streams can produce a well-sorted sand. Finally, the transport energy is somewhat related to the time. The higher the energy the larger the grains that can be transported and suspended (Folk, 1974).

The third and fourth statistical moments, skewness (4.3) and kurtosis (4.4), inform how close the data is to a normal Gaussian distribution (Folk, 1974). Sediments that originated from one source such as beach sands or deltas tend to have a relatively close Gaussian distribution.

Sediments that originated from two or more sources such as lagoon clays or multi-provenance rivers show large skewness and kurtosis readings (Folk, 1974).

Table 2. The mathematical equations for deriving the four statistical moments. 4.1) the average grain size, 4.2) the grain comparison of largest and smallest grains, 4.3) the internal distribution of grains compared to the mean, 4.4) the concentration of grains compared to the total distribution. $\phi_{\#}$ being the grain size of the total population at the given percentage. (Folk, 1974)

Graphical Mean (4.1)	$M_Z = (\phi_{16} + \phi_{50} + \phi_{84})/3$
Graphical Sorting (4.2)	$\sigma_G = (\phi_{16} + \phi_{84})/2$
Graphical Skewness (4.3)	$Sk_{q\phi} = \frac{(\phi_{16} + \phi_{84} - 2\phi_{50})}{(\phi_{84} + \phi_{16})}$
Graphical Kurtosis (4.4)	$K_G = \frac{\phi_{95} + \phi_5}{2.22 * (\phi_{75} + \phi_{25})}$

Chapter 3: Results and Observations

3.1 Road Cut Location

3.1.1 Road Cut Field Observations and Thin Section Analysis

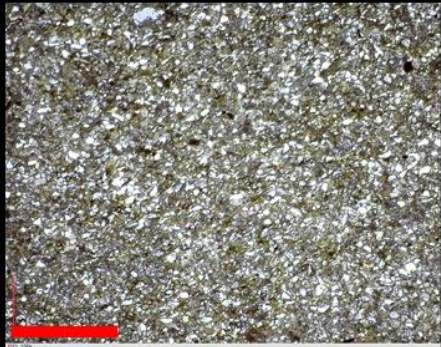
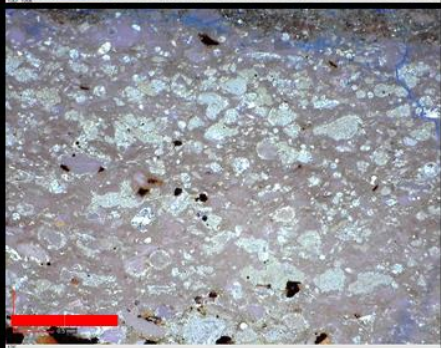

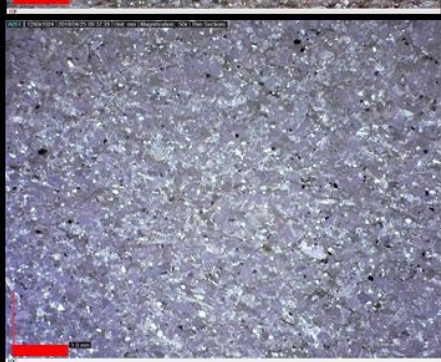
The highway 62 road cut location is both the most well-known outcrop of the Rader Member and the most distal of all the studied areas. Located 5.5km southwest of the entrance to McKittrick Canyon, the outcrop stretches 242 m laterally and contains 18.2 m of vertical stratigraphy. The lowest unit is the Pinery Member, which only the uppermost 1.2 m can be observed. Above this 4.5 m of section is composed of the lower Bell Canyon sands, then the Middle Rader Member occupies the above 3.9m of section. The Upper Rader Member the next 4.9m, and finally, the last 3.3m is comprised of the upper Bell Canyon sandstone.

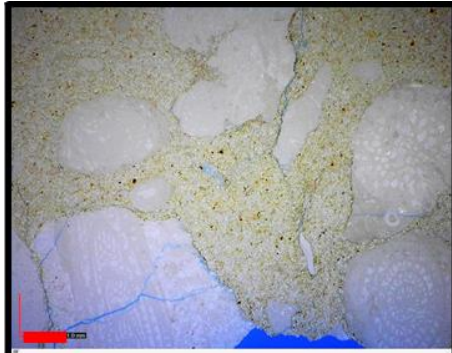
The Pinery and Upper Rader Members are both composed of thin, parallel laminated, sandstones and siltstones. The beds/laminations range in thickness from 5-10 cm. No fossils or reefal clasts are observed within both units. The lower Bell Canyon sands are composed of 5-20 cm, amalgamated, parallel beds. No observable fossils are noted in the Member. The Middle Rader Member, the mega-breccia, contains limestone boulders up to 5m in diameter suspended in a sandy matrix. Within the matrix there is no apparent grading among the grains/inclusions and a lack of internal amalgamation surfaces. The matrix contains a wide variety of clast sizes. Any clasts larger than -8ϕ ($>256\text{mm}$) were classified as boulders and not considered part of the matrix, as defined by the standard grain size classification (Wentworth, 1922). An erosional contact separated the Middle Rader Member from the lower Bell Canyon sands. Above the mega-breccia (separating the Middle and Upper Rader Members) two distinct hummocky beds are present. These beds contain a fining upward sequence with large clasts of fossils and rip-up material suspended in a muddy matrix. There is a sharp boundary between these HCS beds and the mega-breccia, while the contact with the Upper Rader Member is more of a gradational contact. Within the Upper Rader Member, roughly 5m above the hummocky beds is another hummocky bed. A total of 3 other hummocky beds can be found within the Upper Rader Member separated by the thin turbidite deposits. None of these hummocky beds contain a mega-breccia or conglomerate below them.

Samples were gathered and made into thin section at this location and analyzed to determine the fossil assemblages of the different Rader Members. This aided in determining the source of the deposit with respect to the ancient reef. Of the 23 thin sections gathered, 8 are featured below in stratigraphic order, with the Pinery at base and the Upper Rader Members at the top. The key observations were that the fossil assemblages were dominantly from the reef

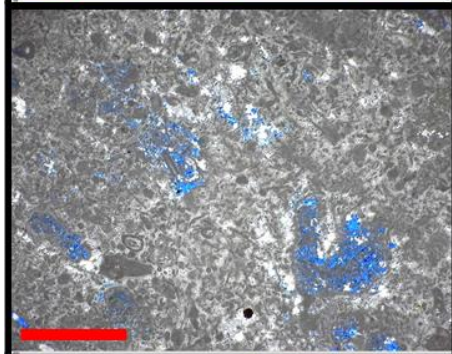
crest, while the Middle Rader Member contained the addition of few back-reef clasts. These included mostly mud pellets and ooids. A shift in matrix styles can be noted from the fine sand/silt of the Pinery and Upper Rader Members to the sandy matrix of the Middle Rader Member. Within the Middle Rader Member, the HCS beds were dominantly composed of larger clasts suspended in a muddy matrix, while the mega-breccia was a sandy matrix which suspended the broken reef fragments.

Table 3. Thin sections from the Road Cut location to represent the stratigraphy.

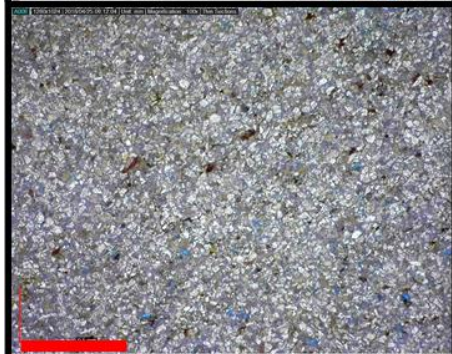
	<ul style="list-style-type: none"> • Upper Rader • Well sorted quartz grains in a muddy carbonate matrix. • Abundant organic matter is entrained within the sample. • No vertical grading is observed. • Minor amounts of dolomitization. • No fossils are observed.
	<ul style="list-style-type: none"> • Upper Rader Debrite • Very fossiliferous containing fusulinids, bryozoans, foraminifera, crinoid stocks, sponge spicules, and brachiopod spines both broken and whole. • Partial calcite replacement of fossils. • Minimal 1-2% porosity. • Very poorly sorted
	<ul style="list-style-type: none"> • Upper Rader • Fining upward sequence. • Lower, coarse, material include brachiopod spines, radiolarians, crinoids, and sponge spicules which are suspended in an organic rich matrix. • Upper, finer, material include radiolarians and sand grains suspended in an organic rich matrix. • No observable porosity. • Abundant organic matter.
	<ul style="list-style-type: none"> • HCS 1 Top • Grains are mostly composed of larger pellets and smaller quartz grains. • Fossils include brachiopod spines, crinoid stems, radiolarian, and sponge fragments. • Matrix is composed of carbonate mud. • No observable porosity. • No vertical gradation and matrix/clasts are poorly sorted throughout. ■ 1mm



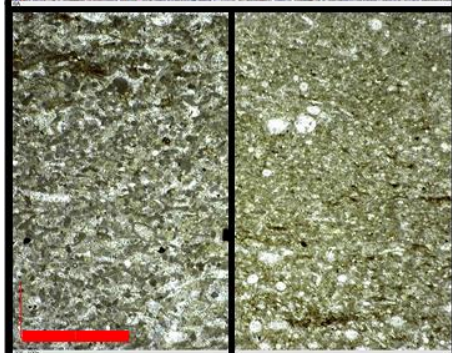
- **Mega-Breccia Matrix**
- Sandy matrix suspending 4-8mm sized inclusions of pre-lithified reefal clasts.
- Other clasts include muddy pellets.
- Hydrocarbon staining is present around many of the reef clasts.



- **Mega-Breccia Boulder**
- Porosity is dominantly located along edges of the sample.
- 15% porosity.
- Contains patches of mudstone and packstone.
- Fossils include Ostracod fragments, ooids (concentric cortex), and Peloids.



- **Mega-Breccia Matrix**
- Composed mostly of quartz grains.
- Porosity ranges from 1-2%, mostly from the dissolution of less stable grains.
- Dark patches is organic material.
- Minor signs of compaction from deformed mica grains
- No fossils.
- Quartz grains are cemented with calcite.
- Framework is grain supported.



- **Pinery**
- Sharp contact between lower and upper sections.
- Lower half is more fossiliferous.
- 15% in the lower half and 10% for the upper half
- Minimal porosity.
- Fossils include brachiopods, radiolarians, and crinoid stocks.
- Both sections fine upward from coarse sediments to very fine. ■ 1mm

3.1.2 Road Cut XRF Analysis

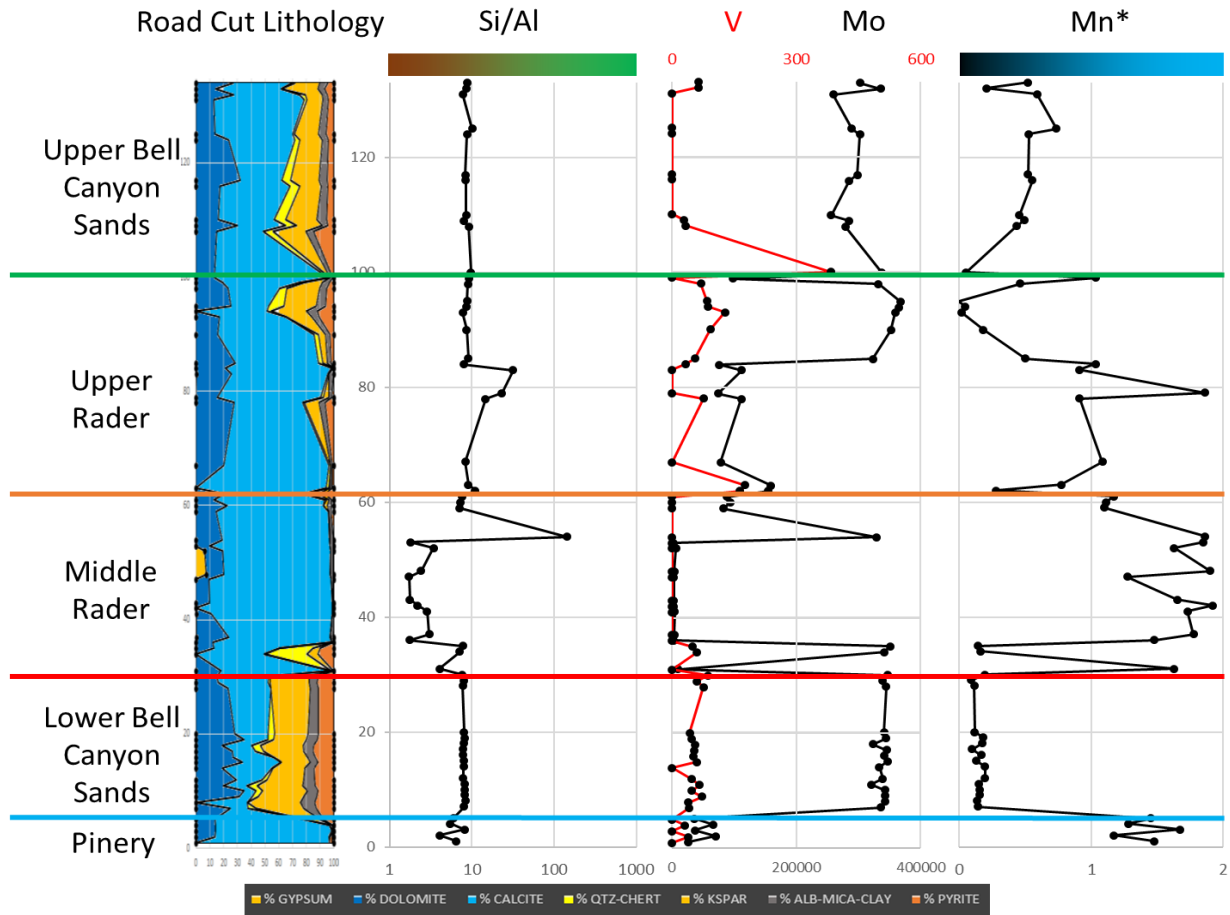


Figure 7. The far-left graph shows the mineralogy distribution of the samples from the program by Dr. Pigott. The Si/Al graph shows detrital source of silica on the left (brown) and biogenic on the right (green). The right two graphs; V, Mo, and Mn*, show indicators for water redox conditions. Low Mn* (black) indicates anoxic conditions, while high Mn* (blue) indicates more oxic conditions. Mo tends to parallel TOC level suggested by Nance & Rowe, (2015) and Algeo & Rowe, (2012).

Whole rock geochemistry of the Road Cut location reveals that the Pinery Member is mostly composed of calcite, with minor amounts of dolomite and other minerals. For the Pinery Member there is a minimal amount of TOC suggested by the Mo abundance, as suggested by Nance & Rowe (2015). Other researchers found that the Ni/Al ratio also mirrors the TOC trends (Algeo, 2004), but due to the lack of continuity of the Ni data the ratio was disregarded. The

origin of the sediments is mostly derived from a detrital source with a mix of minor biogenic silica Si incorporated, indicated by the Si/Al ratio. The comparison of the low V and Mo along with the high Mn* suggest that the Pinery Member was deposited in sub-oxic condition (Hornbuckle, 2017).

The lower Bell Canyon Member sand portion is composed mostly of potassium feldspar fragments and terrigenous sediments. There is an elevated amount of TOC indicated by the Mo abundance. The detrital v biogenic signature is very similar to the Pinery Member, dominantly detrital with a mix of biogenic input. The depositional water conditions were vastly different from the oxic Pinery Member. The low V, high Mo, and low Mn* point to the water column being anoxic during the sand's deposition.

The Middle Rader Member, mega-breccia, is mostly composed of calcite with minor amounts of dolomite, and trace amounts of other minerals. The lower and upper portions of the unit contain higher amounts of TOC signatures, while the middle portion contain minimal amounts of TOC indicators. The sediments are sourced from a more detrital location than the previous two Members, indicated by the lower Si/Al ratio. The water redox conditions are quite complex. The lower and upper portions have signatures of anoxic waters while the middle portion shows oxic waters. An explanation for this observation is that the sediments in this deposit originated from a proximal source higher up in the water column (a sub-oxic zone). When the sediments were transported, the already existing deep-water sediments (anoxic) were incorporated into the new deposit (the lower anoxic reading). As more and more sediments enter into the system the sub-oxic concentrations over power the anoxic reading, resulting in the sub-oxic reading of the middle portion. Finally, as the energy lessens the anoxic elemental signatures begin to dominate again.

The Upper Rader Member was deposited during the period when the basin is reacclimating to the post-catastrophic event. Compositionally, the lower half of the Upper Rader Member is made up of mostly calcite and dolomite while the upper half has the inclusion of more terrigenous sediments. The TOC indicators are moderate and increase upward. For the main source of sediments, they are a mix of detrital (lower and upper portions) and biogenic (middle peak). This middle biogenic signature is the second hummocky bed isolated from the lower hummocky beds associated with the Middle Rader mega-breccia. The biogenetic signature is recorded from the abundance of fossils and other inclusions within the deposit. The water column conditions are a mix of both sub-oxic and anoxic, the lower half shows more oxygenated waters but transitions to anoxic in the upper half of the Member.

The upper most sands, upper Bell Canyon Member, closely resemble the lower section of the Bell Canyon sands (just above the Pinery Member). By this point in the deposition the basin has returned to its normal status. The TOC indicators have returned to abundant amounts. The sediments are mostly detrital with some biogenic inputs, identical to the lower Bell Canyon sands. V and Mo abundances have also normalized, low V and high Mo concentrations. As for the Mn* value, there is still a gradual shift from sub-oxic to anoxic conditions at the top of the measured section.

3.1.3 Road Cut LiDAR Observations



Figure 8. A true color (top) and reflectivity scan (bottom) of the Road Cut location. Three distinct units are observed; Upper Rader Member (top left), the Middle Rader HCS beds (low reflectance), and Middle Rader mega-breccia (below HCS beds). Few limestone boulders can be noted in the true color scan and are masked in the reflectance due to interference from the road (dust). The reflectance scans show that the HCS beds have a distinctly lower reflectance (-8.60dB to -3.2dB) than the surrounding strata (-0.45dB to 3.60dB).

Figure 8 shows two LiDAR scans of the Road Cut southern wall. The true color, top image, highlights that the Upper Rader Member contains parallel beds of distal turbidite deposits, while no structures are observed in the Middle Rader Member. Numerous limestone boulders occur within the mega-breccia, these are the gray inclusions in the tan sandy matrix. Bedding reappears in the lower right of the image where the stratigraphy enters the lower Bell Canyon sand unit, as indicated by the red line.

A reflectance scan of the outcrop, lower image of figure 8, reveals that the mega-breccia and layered turbidites (Upper Rader Member) contain relatively the same reflectance values. These values ranged from -0.45dB to 3.60dB in the mega-breccia and Upper Rader Member, while the hummocky beds range from -8.60dB to -3.2dB. When compared to thin section and XRF measurements this reflectance difference was correlated to higher concentration of mud within the hummocky beds. This is from the sand grains reflecting more energy than the muds resulting in a higher reflectance reading by the LiDAR. In a study conducted by Burton et al (2011) found that sands reflect considerably more light than shales/muds. Sands average roughly 24% reflectance, while muddy shales reflect approximately 9% of the original transmitted energy (Burton, Dunlap, Wood, & Flaig, 2011). Above and below the Middle Rader Member, the layered turbidite deposits have similar LiDAR signatures.

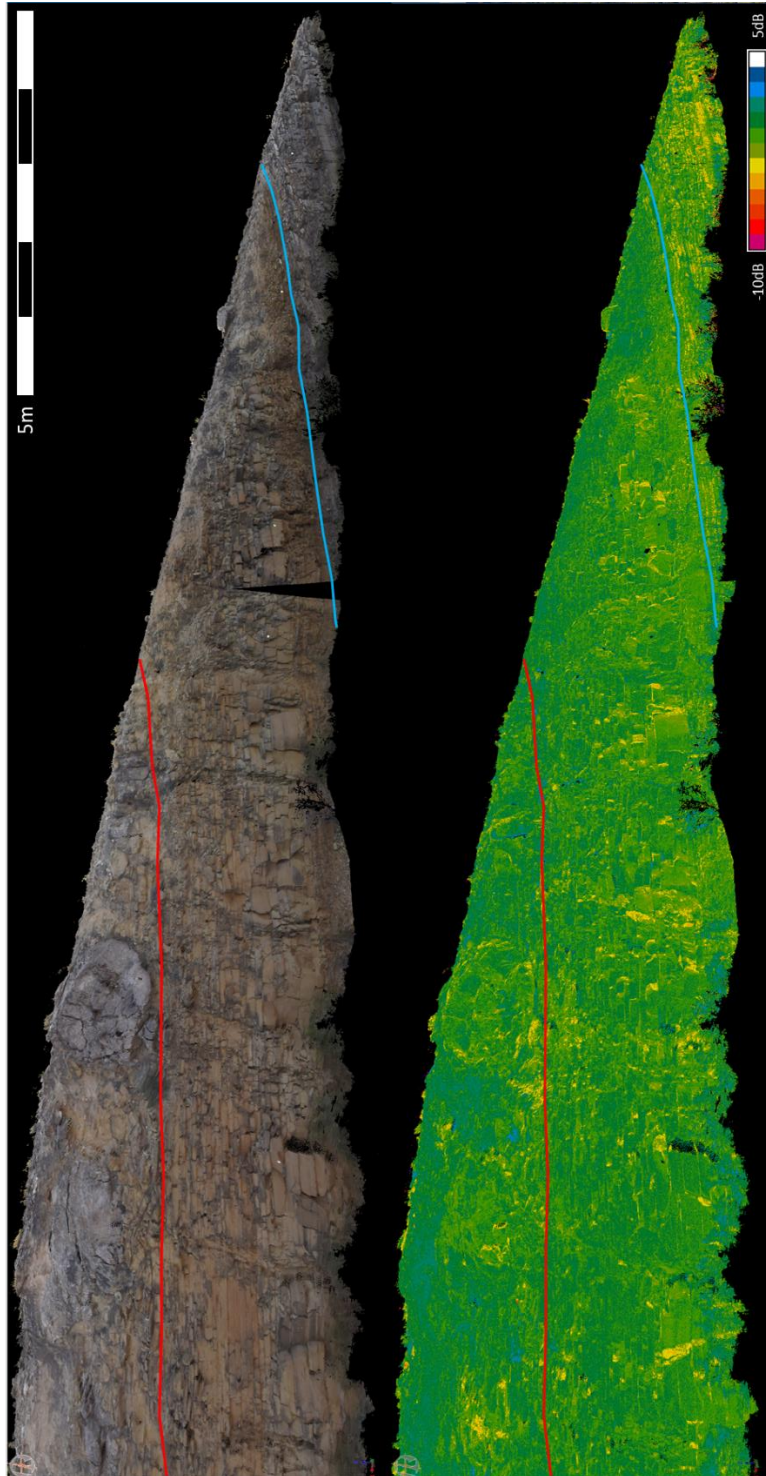


Figure 9. The top image shows a true color scan of the lower portions of the Middle Rader, lower Bell Canyon sands, and Pinery Member's. Top of the lower Bell Canyon sands is indicated by the red line and the top of the Pinery indicated by the light blue line. The lower image shows the reflectance scan of the outcrop. The Pinery Member contains slightly lower reflective material than the lower Bell Canyon sands, and parallel bedding is noted in both the lower Bell Canyon and Pinery, while not in the Middle Rader Member.

Figure 9 shows the Pinery Member with a sharp upper contact with the lower Bell Canyon sands, indicated by the light blue line. Being composed of finer grains than the Bell Canyon sands, the Pinery Member shows lower amounts of reflectance than the Bell Canyon sands and Middle Rader mega-breccia. The bed thickness of the Pinery Member is typically 3-8cm, while the lower Bell Canyons sand layers are 5-20cm thick. The transition from the lower Bell Canyon sands into the Middle Rader Member is most noted as the disappearance of layering and bedding and indicated by the red line. Additional observations from the LiDAR scans show that the lower Bell Canyon sands are fractured vertically, while the Pinery and Middle Rader Members are not.

3.1.4 Road Cut Digital Grain Size Analysis

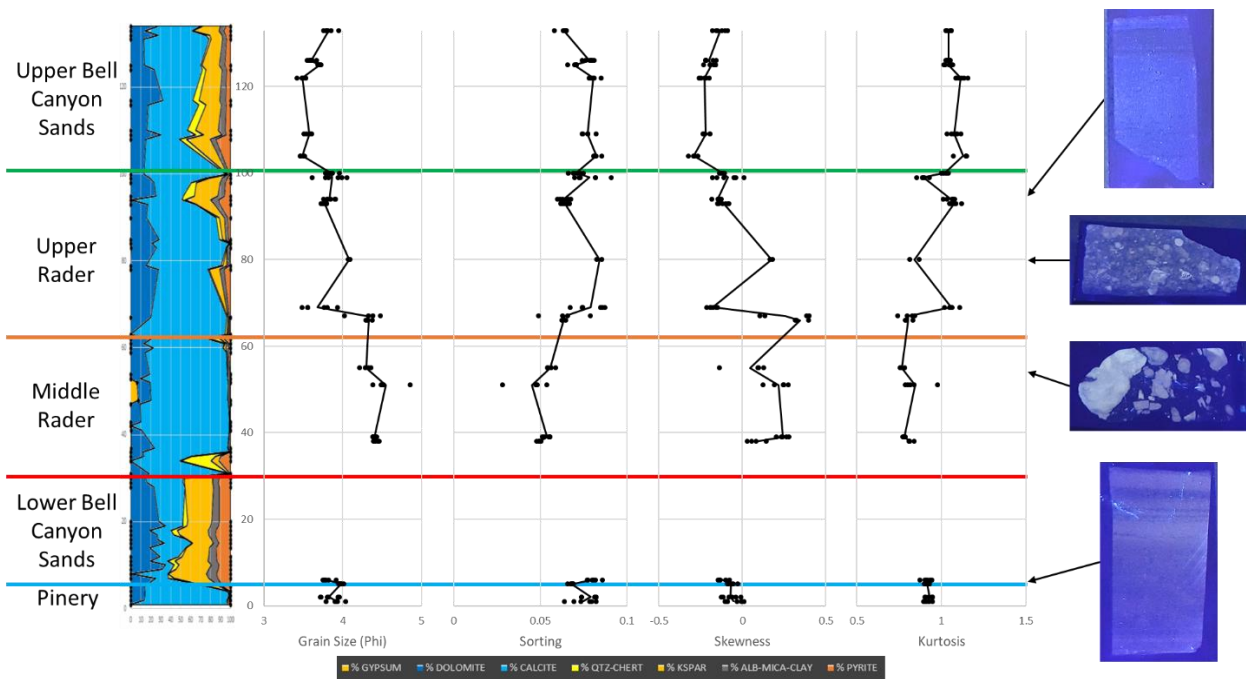


Figure 10. The grain size distribution from the Road Cut location shows the four statistical moments from the Pinery, Middle Rader, Upper Rader, and upper Bell Canyon Members. The far-right shows thin section stocks under a black light to highlight the changes in abundance of carbonate clasts suspended in the sandy matrix.

Twentytwo matrix samples were analyzed from the Road Cut location. Again, the matrix was defined as the grains holding up, and suspending, the larger carbonate reefal material, and did not include the actual clasts.

The bottom four samples were taken in the Pinery Member and show a uniform grain size distribution with an average grain size of 3.88ϕ . The sorting of the sample's trend opposite with the grain size distribution, as the grains get finer, the sorting increases. The skewness of the Pinery Member samples have an average of -0.07 . This negative value indicates that the grain distribution is negatively skewed and within the grain distribution there are more fine grains than coarse grains. Finally, the Kurtosis, averages 0.91 . Since this is less than 1.0 the samples distribution is considered platykurtic (Folk, 1974). Platykurtic samples have a wide grain distribution as compared to samples whose kurtosis is greater than 1.0 (Leptokurtic) and have a concentrated grain distribution.

Moving up into the Middle Rader Member, mega-breccia, no apparent gradation grain size changes are observed, and it has an average grain size of 4.41ϕ . As for the hummocky beds, they are internally graded and fine upwards, which can be observed in more detail within the Creek Bed. The mega-breccia does not show any major changes in sorting. As for the skewness, the mega-breccia is positively skewed and has an average value of 0.14 . This positive value means that the grain distribution is positively skewed, the grain distribution contains more coarse grains than fine. Similar to the Pinery Member, the Middle Rader Member has a kurtosis value of 0.80 , making the sample platykurtic, and giving the Middle Rader Member a more even distribution of grains than the Pinery Member.

The Upper Rader Member starts off with finer grained sediments then abruptly shifts to coarser sediments around sample depth 67 in figure 10. Overall the average grain size is 3.98ϕ .

Within the Upper Rader Member, the sorting is more uniform and becomes less sorted up section. The transition from the finer (lower) portion also shows a slight change in the grain skewness where the trend moves to more negatively skewed, but then normalizes. The lower two samples have an average skewness of 0.30 while the upper four have an average skewness of -0.13. There is a shift from positively to negatively skewed samples. Similar to the skewness, the kurtosis also shows a transition from the lower two samples being platykurtic (>1) and the upper four samples being leptokurtic (<1). The average values being 0.81 for the lower, and 1.02 for the upper section. At depth 80, in figure 10, there is a peak different from the trend around it. This sample is from the second debrite bed. The shift in textural readings indicate a major change in the depositional energy.

The upper portion of the Bell Canyon sands show a uniform average grain size that starts to fine upward at the top of the section. The average grain size is 3.64ϕ , the coarsest of the Road Cut location. The sorting, like the previous intervals, mirrors the grain size trend. The grains become more well sorted in the upper portion. The skewness averages -0.19, the most negatively skewed of the outcrop. Finally, the kurtosis averages 1.06 and is leptokurtic, meaning the grains are concentrated in one main grain size.

Reviewing the analytical data of the CDGSA data from the Road Cut creates an interesting question: Why does the Middle Rader mega-breccia contain the smallest mean grain size? Typically, with a mass transport deposit this is not the response one would expect. There are two ways to decrease the mean grain size of a sample. Assuming one has a normal distribution, the first is to lower the abundance of coarse material by subtraction, and the second is to increase the abundance of finer material by addition. By examining the other statistical moments, the answer can be made clear as to which of these the Middle Rader mega-breccia is

undergoing. The Middle Rader Member is positively skewed meaning that within the distribution of the sample there is an increase in distribution of finer material. To aid with this, the kurtosis of the Middle Rader Member shows it to be on the platykurtic side. This means that the grain distribution and abundance is closer to uniform across the board rather than one grain size dominating the system. Finally, these observations are confirmed once more with the Middle Rader Member being the least sorted of the observed Members from this location.

3.2 Creek Bed Location

3.2.1 Creek Bed Field Observations and Thin Section Analysis



Figure 11. Photo of the three hummocky beds in the Creek Bed location. The top of hummocky bed 1 is indicated by the blue arrows, top of the second bed in green, and top of the third bed in yellow. Between the second and third hummocky beds is a thin dark shale. Above the HCS beds are turbidite deposits of the Upper Rader Member.

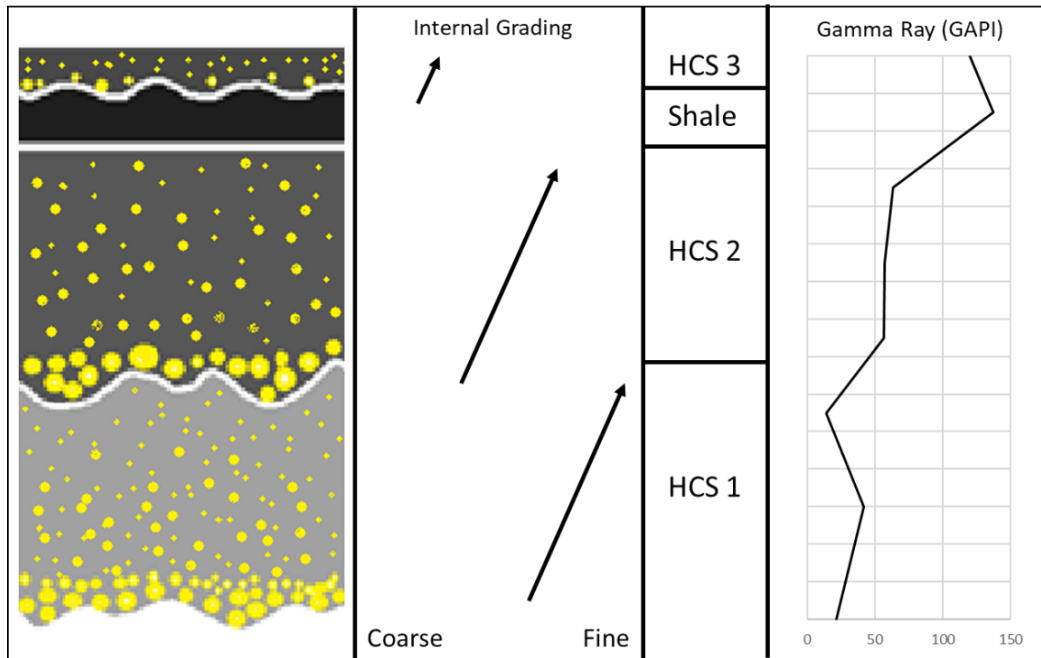


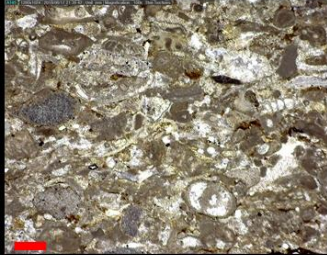
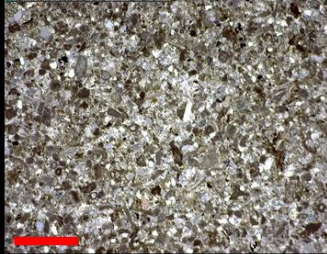
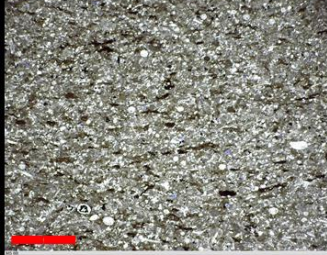
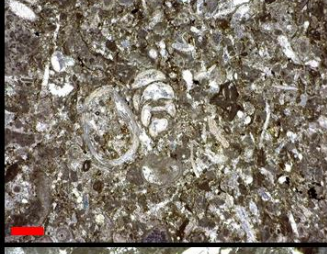
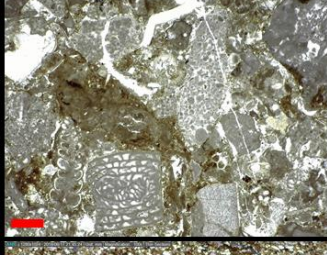
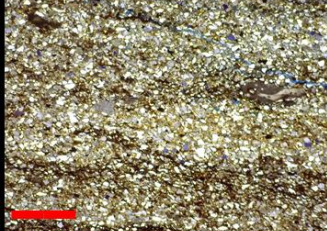
Figure 12. The left image shows a cartoon reconstruction of the internal grading of the three hummocky beds. The middle image shows a comparison of relative grain sizes and grading from one bed to another. The right image is the gamma ray curve measured in the field using the hand-held RS-230. There is a gradual increase in GAPI moving from one bed to another, with the shale being the most radioactive.

Located 450m north of the Road Cut outcrop, the Creek Bed consisted of 15.5m of well exposed stratigraphy of the Lower, Middle, and Upper Rader Members. The matrix of the Middle Rader mega-breccia shows a homogeneous gamma-ray signature with an average of 93GAPI units. While gamma-ray values increase within the hummocky beds (Figure 12). The GAPI curve was determined by using the standard by Ellis and Singer (1987). The approximately 5 cm shale bed between hummocky beds 2 and 3 has a gamma-ray reading of 137GAPI units, the highest reading at the outcrop. The three hummocky beds are observed to be three separate packages of fining upward sequences. Numerous fossil clasts are at the base of beds 1 and 2, while bed 3 contains larger observable shell fragments (middle of figure 12). Laterally, hummocky bed 1 has a 2m wave length and an amplitude of 0.3m, HCS 2 has a

wavelength of 2m and an amplitude of 0.2m, and HCS 3 has a wavelength of 2m and an amplitude of 0.05m (figure 11). Each bed moving up contains the roughly the same wavelength, but the amplitudes decrease vertically. The outcrop contains fewer boulders than the Road Cut. This is due to the creek weathering the matrix and dislocating some of the smaller boulders and leaving the larger ones. The boulder that remain attached to the wall show morphological features of the sands forming envelopes around the bounders. This indicates that the limestone clasts were not rolling down the slope to their current location, rather these boulders were plowing through (moving along with) the sands as one massive slide.

A total of 12 thin sections were collected at this location, of these 5 are shown below which represent a stratigraphic column. The mega-breccia is at the base and the Upper Rader Member is at the top of the shown samples. Similar to the previous location, these thin sections were analyzed to determine the source of the deposit relative to the ancient reef.

Table 4. Thin sections from the Creek Bed location which represent the vertical stratigraphy from the Middle to Upper Rader Members.

	<ul style="list-style-type: none"> • HCS 3 • Contains large clasts suspended in a muddy matrix. • Lateral organic pathways connecting grains. • Lower half contains a muddy matrix while the upper half is a more organic rich matrix. • More radiolarian are present in the upper organic rich half.
	<ul style="list-style-type: none"> • HCS 2 Middle • Moderately sorted reef clasts with a sand/mud matrix. • Sand grains are well sorted and sub-rounded. • Minor amounts of hydrocarbon staining along bedding. • Minor amounts of porosity in fractures. • Clasts and grains are suspended in the matrix. • Few crinoid stocks and a handful of other fossil assemblages.
	<ul style="list-style-type: none"> • HCS 1 Top • No porosity is observed. • Dominantly composed of quartz grains with a muddy matrix. • Partial calcite replacement of grains and clasts. • Minor decreasing sand concentration upward. • Organic rich laminations. • Few radiolarians are present with no other fossils.
	<ul style="list-style-type: none"> • HCS 1 Middle • Fining upward sequence • Base contains large clasts and fossils. • Most fossils are unbroken, and clasts are parallel to bedding. • Sand grains are sub-rounded. • Little to no porosity is observed.
	<ul style="list-style-type: none"> • HCS 1 Base • Poorly sorted fossils with a muddy matrix. • No observable porosity. • Few of the reef clasts are from previous MTC deposits which have been redeposited (middle oval grain).
	<ul style="list-style-type: none"> • Mega-Breccia Matrix • Increasing amounts of organic material vertically. • Few large clasts of reef material. • No fossils are observed. • 5% porosity mostly located in fractures and dissolved grains.

3.2.2 Creek Bed XRF Analysis

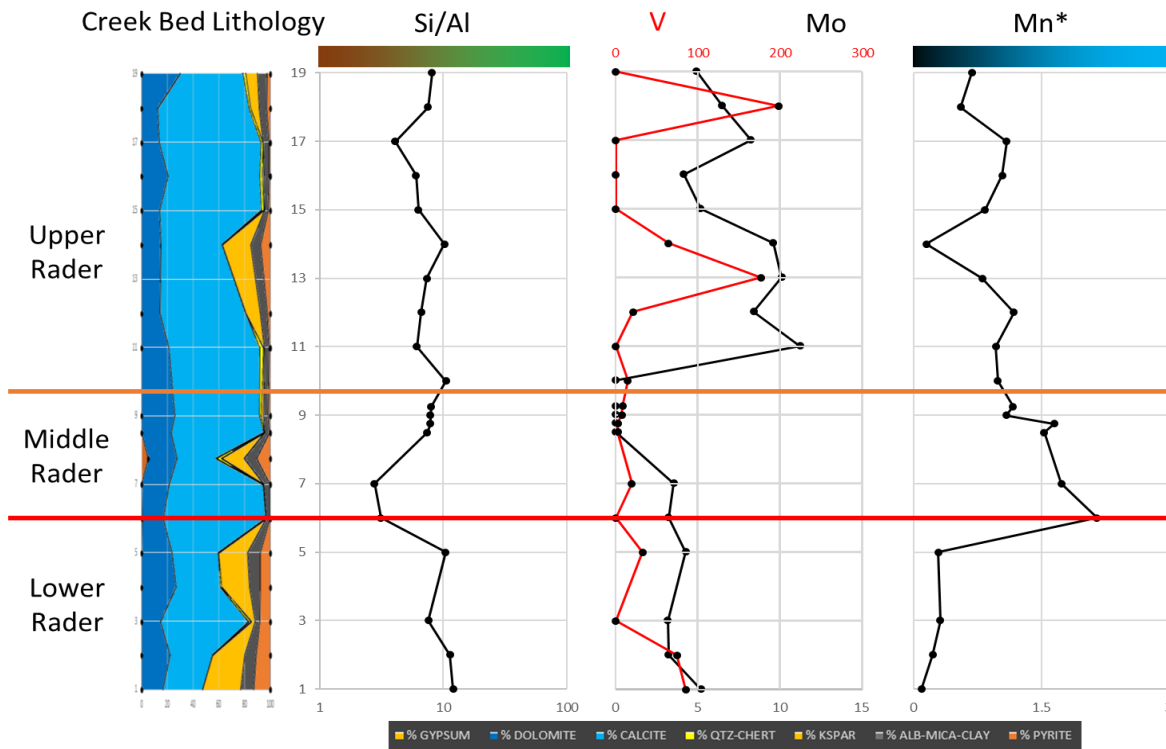


Figure 13. The far-left graph shows the mineralogy distribution of the samples from the program by Dr. Pigott. The Si/Al graph shows detrital source of silica on the left (brown) and biogenic on the right (green). The right two graphs; V, Mo, and Mn*, show indicators for water redox conditions. Low Mn* (black) indicates anoxic conditions, while high Mn* (blue) indicates more oxic conditions. Mo tends to parallel TOC level suggested by Nance & Rowe, (2015) and Algeo & Rowe, (2012).

The Creek Bed XRF geochemistry contains limited data owing to the late discovery and lack of usable XRF data from the 2016-2017 study. Nine additional samples were examined within the Middle Rader Member, but due to the epoxy used in thin section making distorted the XRF results these could not be compared to the previous geochemical study, except for the trace elemental abundances. All results from this location have been interpreted from the data collected in 2015-16.

The lower most observed section is the Lower Rader Member is composed of even parts silicates and carbonates. The Member contains minor amount of TOC indicated by the Mo

abundance. The Si/Al ratio resembles the Road Cut, indicating a dominantly detrital input with minor amounts of biogenic silica Si. The abundance of V is low, while Mo averages <5ppm, considerably lower than the previous measured section. On the other hand, the Mn* factor does resemble the Road Cut. As stated previously, no one element is used as a proxy to determine the paleo-conditions during deposition. Since V and Mn* are suggestive of anoxic waters, the abnormal Mo was ruled out.

The Middle Rader Member has mostly the same elemental proxy signatures as the Road Cut. Since both the Mo and Si/Al ratio are similar to the previous study location, then the difference can be attributed to the aluminum Al concentration. Possibly being removed due to the location being an active creek. Two additional points were included into the proxy analysis for this section but were not included for the lithology assessment. The added samples were measured with the XRF back at the university, after being made into a thin section. The thin section stocks were the actual samples measured and contained a silica rich epoxy which distorted the main elemental results. A correction was applied to the new samples to match them to the previously gathered samples and remove the signature of the epoxy. The clustering of samples at the top of the Middle Rader Member are the three hummocky beds. These beds are closely related to the underlying mega-breccia in terms of trace elements.

The Upper Rader Member is composed mostly of carbonate minerals with minor inclusions of terrigenous material. The average abundance of TOC indicators increases from the Lower and Middle Rader Members. The detrital to biogenic source fluctuates a bit but is mostly detrital based. The paleo-redox conditions also fluctuate, but the interval is in the basinal rebound phase where it is reacclimating after the chaotic event.

3.2.3 Creek Bed LiDAR Observations



Figure 14. A true color (top) and reflectivity scan (bottom) of the Creek Bed location. Three sections are present within the scans: Middle Rader mega-breccia bottom half), Middle Rader HCS beds, and the Upper Rader Member (parallel beds in upper half). The HCS beds are marked by the first three beds above the massive mega-breccia, and grade into the Upper Rader Member. Reflectance values are skewed due to the location being an active creek. The outcrop is coated with a lining of mud/clay which has stunted the accuracy of all LiDAR scans except for the true color.

The upper part of figure 14 shows a LiDAR, true color image of the Creek Bed. A sharp contact between the mega-breccia and hummocky beds can be observed about half way up the scan. The contact between the hummocky beds and the Upper Rader Member turbidites is a gradational contact. Within the mega-breccia, the lower half of the image, a dark algae is growing on the face of the outcrop. This interferes with the LiDAR reading since the beam cannot penetrate past the surface features. This interference can be observed more predominantly in the reflectance attribute, lower figure 14. The algae appear as a very absorbent material and has a low reflectance value of -9dB. In addition to the algae, due to the location being an active creek bed the outcrop walls are also covered in a thin layer of mud/clay. This thin coating masks the unique signatures of the different units. The distinctly low reflectance of the hummocky beds observed at the Road Cut are covered up and do not stand out at this location. Above the hummocky beds, beyond the reach of the creek processes, the layered turbidites are highlighted by alternating high and low reflectance values. Similar to the Road Cut, the reflectance values for the Upper Rader Member ranges from -0.45dB to 3.60dB. The contact between the hummocky beds and the Upper Rader Member is easier to observe through reflectance than the true color image.

3.2.4 Creek Bed Digital Grain Size Analysis

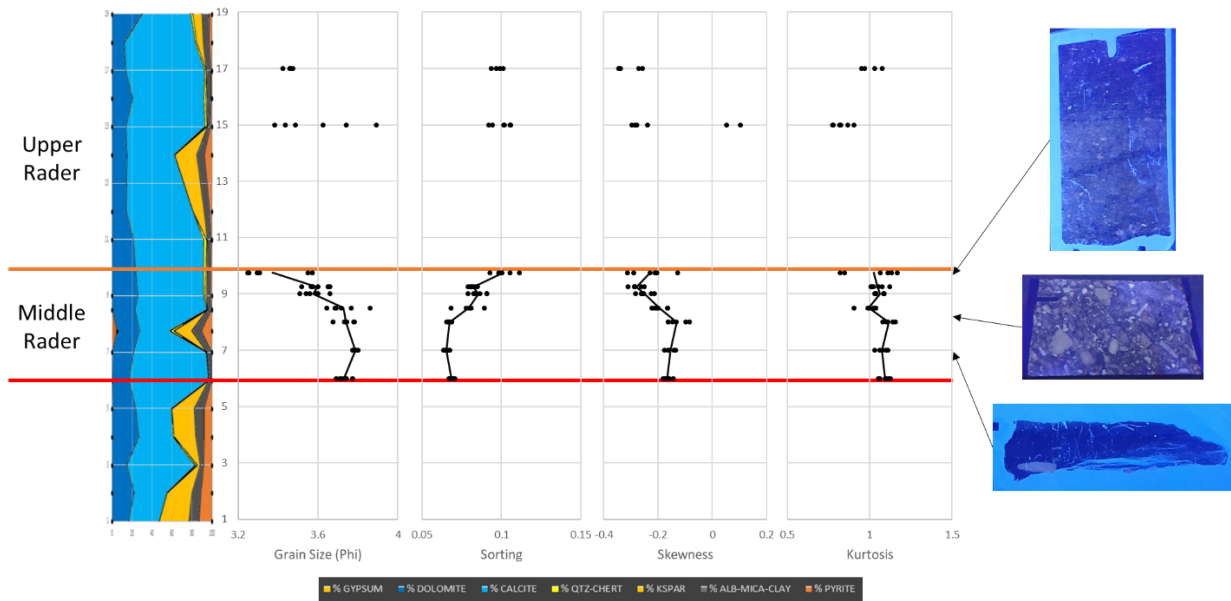


Figure 15. The grain size distribution from the Creek Bed location showing the four statistical moments in the Middle Rader and Upper Rader Members. Moving from left to right the graphs are; XRF lithology, Mean Grain Size, Sorting, Skewness, and Kurtosis. The far-right shows thin section stocks under a black light to highlight the changes in abundance of carbonate clasts suspended in the sandy matrix.

Of the ten samples taken from the Creek Bed location, nine could be processed through the Digital Grain Size Analysis (DGSA) script. The exception being the lowest sample from the hummocky 1 bed since the average grain size was too large to accurately be measured by the script, as mentioned before needing approximately 1000 grains for an accurate measurement.

Within the mega-breccia, the grains have a relatively consistent distribution. Average grain size in this interval is 3.75ϕ . Moving into the three hummocky beds, each bed contains less fine material than the previous bed. The average grain size changes from 3.68ϕ in hummocky bed 1, 3.59ϕ in hummocky bed 2, and 3.37ϕ in hummocky bed 3. The sorting of the Middle Rader Member mirrors the trend of the mean grain size, and the samples become more poorly sorted moving vertically upward. All the Middle Rader Member have a negative skewness with

an average value of the mega-breccia being -0.15, and the hummocky beds transition from -0.22 to -0.27. This skewness change correlates to the observed grain size shift and indicates that the average grain size is not increasing, rather the abundance of finer grains is being depleted, resulting in the same mean grain size trend. The mega-breccia has a kurtosis of 1.09, then drops to 0.99 at the middle of the first hummocky bed. This boundary transitions from a leptokurtic distribution in the mega-breccia to a mesokurtic distribution in the hummocky beds. Moving through the hummocky beds the kurtosis gradually moves toward the leptokurtic distribution.

Similar to Road Cut DGSA (3.1.4), the Middle Rader mega-breccia is observed to contain the smallest mean grain size, and the same conclusion of the addition of finer material can be made from the other statistical moments. As for the HCS beds, it was interpreted that the finer grains were being removed vertically resulting in the coarsening upward sequences observed.

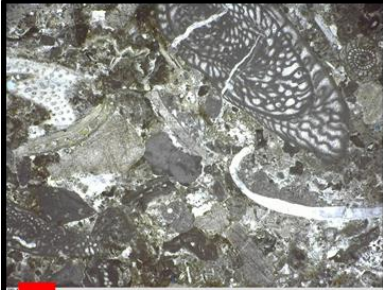
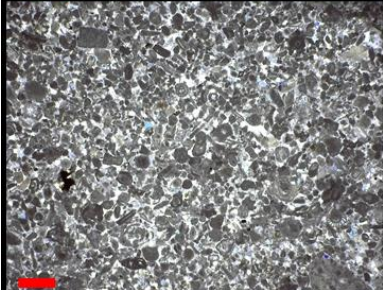
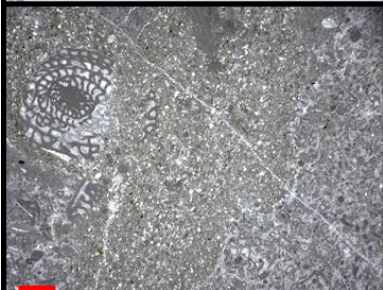
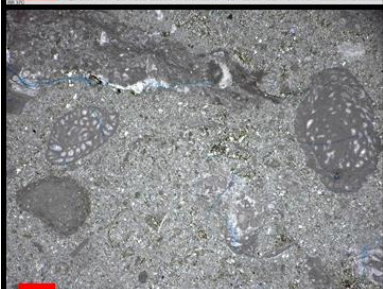
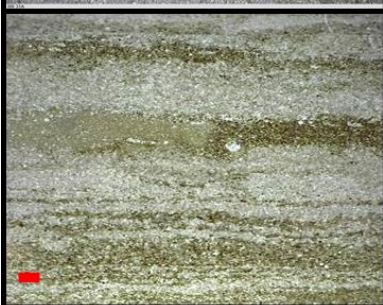
Two samples were taken from the Upper Rader Member but due to the separation of the data points, no definitive conclusions could be made. Though the average grain size and distribution does mimic the measured Road Cut location.

3.3 Rader Ridge

3.3.1 Rader Ridge Field Observations and Thin Section Analysis

Two Rader Ridge sections were examined 2km to the northwest of the Creek Bed (Figure 5), the proximal section being 450m closer to the reef than the distal section. Vertically the proximal section measured 15.8m of stratigraphy containing the Middle and Upper Rader Members. The distal section measured 63.7m of vertical stratigraphy containing the Lower through Upper Rader Members. Due to slope conditions, portions of the section were covered up and had to be skipped during the descriptions in the previous study. Hand samples were only collected at the distal location and thus the proximal section has been omitted from this discussion. 5 thin section were gathered at this location and are shown below.

Table 5. Thin sections from the Rader Ridge location which represent the vertical stratigraphy.

	<ul style="list-style-type: none"> • Upper Rader Debrite • Poorly sorted grains with a muddy matrix. • Large angular clasts of broken fossils, mud, and breccia. • Fossils include brachiopod spines, forams, bryozoan fragments, sponge spicules, fusulinids, and trilobite shells. • No porosity is observed in the sample.
	<ul style="list-style-type: none"> • Upper Rader • Mud pellets compose the vast majority of the sample with few quartz grains. • Minimal porosity is present. • Fossils include brachiopods, sponge fragments, forams, bryozon, and girvanella. • Few clasts of pre-lithified back reef material (peloidal wackestone).
	<ul style="list-style-type: none"> • Mega-breccia Matrix • Very large carbonate clasts suspended in a dolomite matrix. • Clasts contain back reef fossil assemblages, and rip-up clasts from previous MTC deposits. • Fossils include crinoid stems, radiolarians, ooids, sponge fragments, and broken forams.
	<ul style="list-style-type: none"> • Mega-breccia Matrix • Very poorly sorted • Dolomite matrix • Clasts are composed of various broken fossils and suspended in the matrix (wackestone). • Smaller clasts are mostly composed of rip-up muds. • Fossils include forams, brachiopod spines, fustulinids, and sponge spicules. • Porosity is present along clasts edges.
	<ul style="list-style-type: none"> • Lower Rader • Gradual fining upward sequence with carbonate clasts at the base grading into silty muds/sands at the top. • Laminations of organic rich zones (darker) and non-organic rich zones (lighter). • Essentially no porosity is observed. • Erosional surface is present between layers. • Radiolarians are the dominant fossil assemblage. <p>1mm</p>

3.3.2 Rader Ridge XRF Analysis

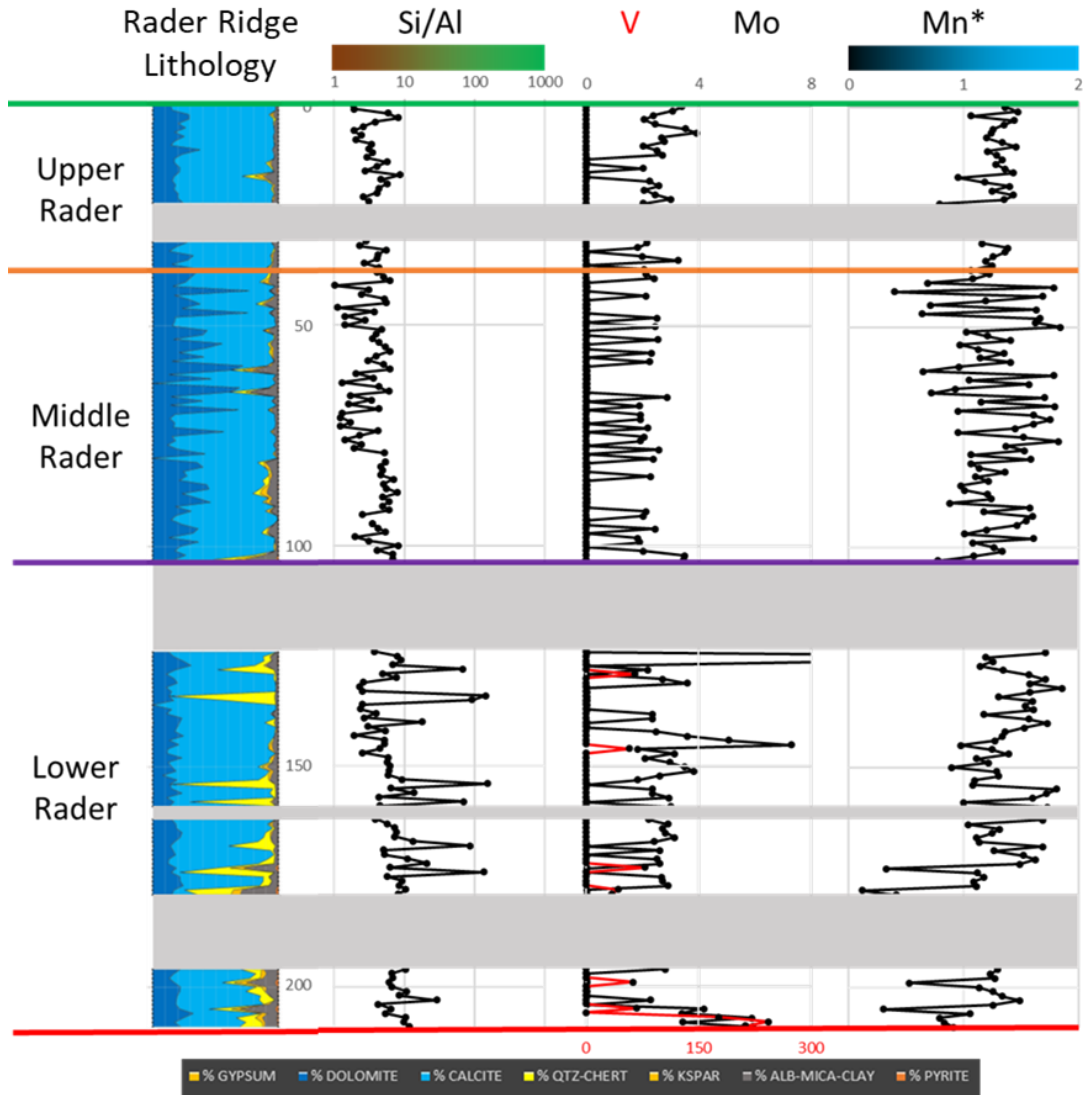


Figure 16. The far-left graph shows the mineralogy distribution of the samples from the program by Dr. Pigott. The Si/Al graph shows detrital source of silica on the left (brown) and biogenic on the right (green). The right two graphs; V, Mo, and Mn*, show indicators for water redox conditions. Low Mn* (black) indicates anoxic conditions, while high Mn* (blue) indicates more oxic conditions. Mo tends to parallel TOC level suggested by Nance & Rowe, (2015) and Algeo & Rowe, (2012). The gray bars indicating sections of heavy cover where no measurements or observations could be obtained.

The distal portion of the Rader Ridge location was split into five segments with the base starting at the top of the lower Bell Canyon sands (base of the Lower Rader Member).

The Lower Rader Member is primarily composed of calcite with thin beds of a silica-based deposit. Elemental TOC indicators gradually increase in abundance vertically through the section, suggesting changing conditions or input material. The thin silica-based beds are a result of increased biogenic activity in the region as indicated by the Si/Al ratio. The carbonate materials, on the other hand, are from a detrital source. The Lower Rader Member contains the only occurrences of vanadium V, and slightly elevated abundances of Mo. Vertically through the section the Mn* factor gradually increases. This increase is potentially a result of the water column becoming more oxic.

The Middle Rader Member is mostly composed of carbonate material with minor amounts of clay/mica minerals. There are two different elemental signatures present within this section. The first is located in the bottom 10 samples within the Middle Rader Member, and above the 23rd sample to the top of the section in figure 16. The second signature are from the samples 11 through 23, indicated by the “block” of clay/mica rich composition. The clay/mica depleted samples have higher TOC indicators and have more of a detrital source. The clay/mica rich samples have little to no TOC indicators and are more biogenically sourced. The whole Middle Rader Member contains a low order of detection of vanadium V. The Mo occurs as isolated alternating peaks. These Mo peaks correlate to dolomite rich lithologies. The Mn* reading is chaotic moving vertically upward, though the overall average suggests oxic conditions.

The upper most Member, the Upper Rader Member, closely matches the Middle Rader Member with the difference being the lack of dispersion within the Mn* reading.

3.3.3 Rader Ridge Distal Digital Grain Size Analysis

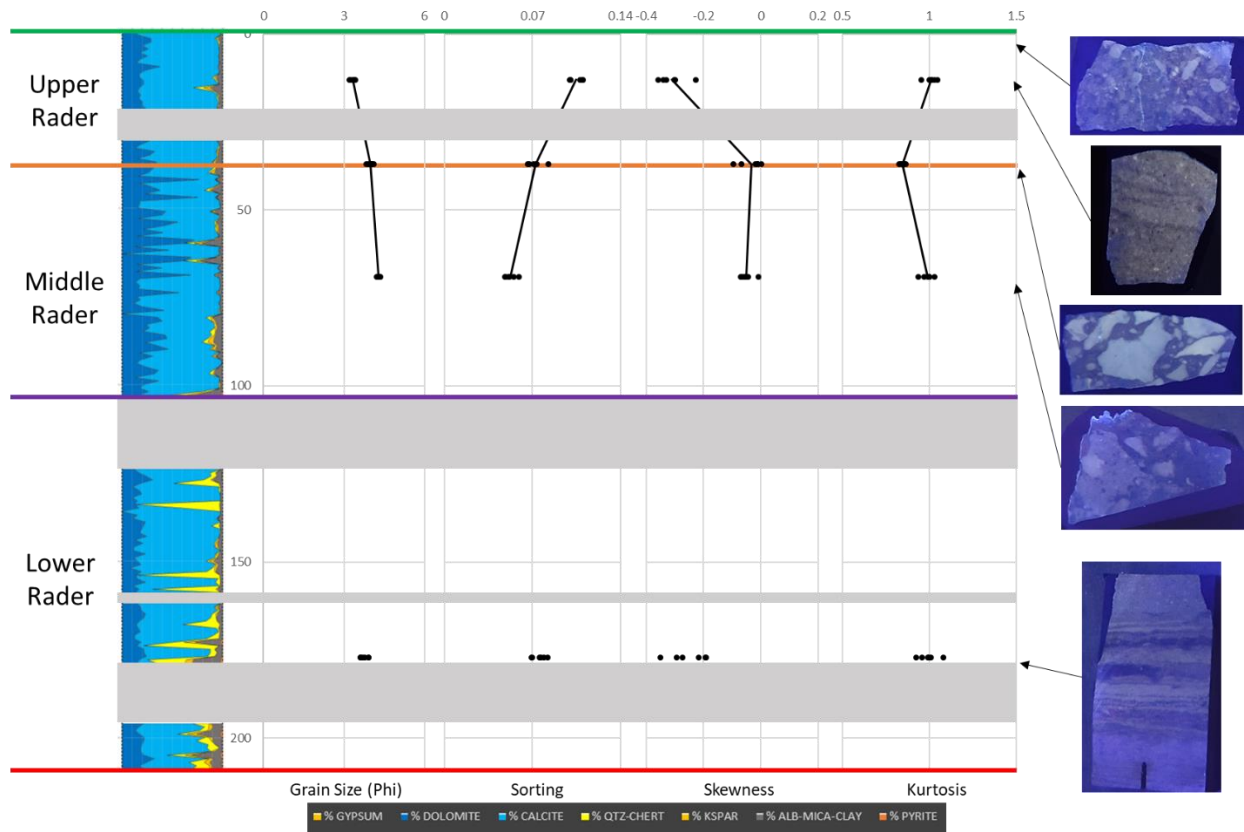


Figure 17. The grain size distribution from Rader Ridge Distal showing the four statistical moments in the Lower Rader, Middle Rader and Upper Rader Members. Moving from left to right the graphs are; XRF lithology, Mean Grain Size, Sorting, Skewness, and Kurtosis. The far-right shows thin section stocks under a black light to highlight the changes in abundance of carbonate clasts suspended in the sandy matrix. The gray bars indicate sections of heavy cover where no measurements or observations could be obtained.

Four of the five thin sections obtained from the Distal Rader Ridge location could be processed through the DGSA script. The sample omitted was the Upper Rader Member debrite, table 4. Despite being separated vertically, trends can still be noted. The base of the location, the Lower Rader Member, contains a similar grain size 3.75ϕ . The sorting is slightly less sorted than the Middle Rader Member. The Lower Rader Member is negatively skewed at -0.25 and has a kurtosis of 0.99 making the grain distribution essentially mesokurtic. The Middle Rader Member

shifts to a slightly finer mean grain size of 4.13ϕ . The sorting through this interval became worse, though only two samples were taken. The Middle Rader Member has a more evenly distributed grain skewness of -0.04 while the kurtosis changes from 0.98 to 0.84 at the top of the interval. This change in kurtosis is from a mesokurtic to platykurtic distribution. The Upper Rader Member sample shows a slight increase in mean grain size to 3.31ϕ , while the sorting becomes worse (more poorly sorted). There is a major change to the skewness from the Middle to Upper Rader Member. The Upper Rader Member more closely resembles the Lower Rader Member with a skewness of -0.30. Like the skewness the kurtosis also resembles the Lower Rader Member with a value of 1.01.

Chapter 4: Interpretations

4.1 Paleo-Redox Conditions

The Rader Member is determined to be a sub-oxic to anoxic condition during its time of deposition in the Late Guadalupian. In Algeo & Rowe, (2012), reduced Molybdenum and anoxic conditions occur around 30% of the relative water depth. For the Delaware basin this would be approximately 275 meters below sea level. Thin section analysis from the Lower and Upper Rader Members, show fossil assemblages of benthic foraminifera which require some amounts of oxygen to persist (Wilson & Schieber, 2015).

As stated previously, a suite of various elements was used to discern the paleo-redox conditions during the time of deposition, these included: Mo, Co, V, Ni, Cu, and Mn* (Crosby, 2015). For determining variations in oxygen content V, Cr, Co, and Mo are the most sensitive to these changes. Mo and V are two of the most commonly used elemental proxies to determine whether conditions are oxidizing or reducing due to their immobility and independence from

detrital fluxes (Turner et al., 2015). Redox conditions are when the demand for oxygen exceeds supply, or, when restricted water column circulation prevents oceanic oxygen renewal (Tribovillard et al., 2006). However, this could be a result of the “basin reservoir effect” as stated by Algeo and Rowe (2012). Ni and Cu are commonly in association with organometallic complexes, thus when these elements are in higher concentrations, they are used as markers of high organic matter input into the basin (Tribovillard et al., 2006).

Mo and V values tend to be suppressed mostly into isolated peaks. This supports more evidence for sub-oxic conditions, as opposed to anoxic conditions. However, during the deposition of the Rader Member, the Delaware Basin was becoming separated and restricted from the Panthalassa Ocean. This increasing restriction is interpreted to be the main cause of low Mo and V readings due to a lack of replenishment of these elements into the separated basin (Algeo & Rowe, 2012).

4.2 Depositional Processes of the Middle Rader Mega-Breccia

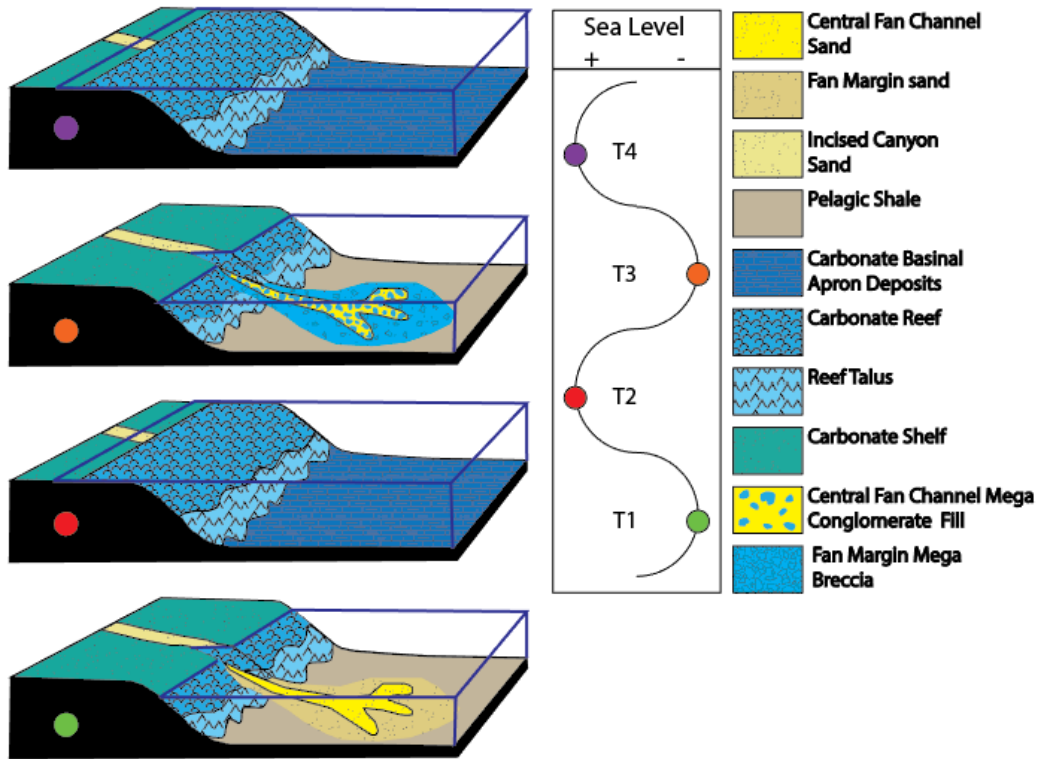


Figure 18. During times of low sea levels, the basin is dominated by sediments which originate from a terrestrial source, deep water fan deposits. Once the sea levels rise, predominant sedimentation is through carbonate reef growth along the crest of the basin. In the deeper portions of the basin, an organic-rich hemipelagic drape (shale) is deposited as a continuous sheet, this is known as the maximum flooding surface. Once sea level falls again, the sedimentation is again dominated by a terrestrial source. Commonly fan-like turbidite gravity flows, and in rare conditions instability of the new carbonate slope can develop causing it to breakoff and slide into the basin. The figure is taken and constructed by Hornbuckle, 2017.

A visualization of the Rader Member's deposition by Hornbuckle (2017) relates the changes in sedimentation styles explained by Vail and Galloway (Galloway, 1989; Vail, 1987). During low sea level times (T1) deep-water fans are deposited in the basin and are composed mostly of terrigenous sands and other eroded sediments. Once sea level rises and the system becomes a high stand time (T2), the growth of the system is predominantly through the carbonate reef, while sediment sourced from the land are restricted/depleted in the basin. These sands tend

to build up behind the reef crest and form shallow water deltas. Along with the carbonate growth, a thin organic rich shale layer is draped over the deeper portions of the basin, this is known as the condensed section associated with a maximum flooding surface (Galloway, 1989). When sea level begins to fall once again (T3) those sands that were deposited behind the shelf along with terrigenous sands are transported down the slope and into the basin as turbidite gravity flows. These flows can be initiated through a variety of different means. Common causes being seismic or other geophysical causes for the sediments to be agitated or falling sea level causes the pore pressure developed during a high stand time to be out of balance with the overburden pressure from the lower water column and cause fractures. When this occurs large portions of sediments and reef can become unstable and fracture. The change from high stand (T2, T4) to low stand (T1, T3) is a very cyclical processes and is well documented and studied globally (Galloway, 1989; Nance, 2007; Saller, 2013; Sarg, 1988; Tinker, 1998; Vail, 1987).

Nicklen, Bell, and Huff (2015) correlated the basin deposits (i.g. Pinery, Rader Members) to the back-reef sands (i.g. Yates, Tansill Formations) defined by Tinker (1998) (Figure 3). As stated previously, the Lower Rader Member was correlated to Y3 (Yates 3), the Upper Rader Member to Y4 (Nicklen et al., 2015). Taking this a step further the Y3 unit was determined to be deposited in a high stand time with a fall in sea level at the very top of the unit (Tinker, 1998). The Y4 unit was interpreted to be deposited under the same style of sea level changes (Tinker, 1998). Given that the end of Y3 was falling sea level (T2 to T3), and the start of Y4 was rising sea level (T3 to T4), then the boundary between the two is interpreted to be a low stand time (T3), and correlative to the Middle Rader Member (Figure 18).

Evidence for seismic activity can be observed within the Brushy Canyon road cut as soft sediment deformation (personal communication with Dr. Pigott; Saller, 2013). The occurrence of

these seismites indicates that seismic activity continued well past the Carboniferous, and that earthquakes could be a trigger for the sudden failure of the Capitan Reef. Located near Whites City, NM, are numerous Neptunian dikes which indicate large scale fracturing of the reef (Figure 19).



Figure 19. The left image shows a Neptunian crack near Whites City, NM, with a rock hammer for scale. The right image, taken by Peter Scholle, shows the internal structure of the cement, post-fracturing (healing). Penny for scale. The cement growth pattern suggests that these fractures remain unstable up until the point that they are fully healed. The common orientation of these fractures is to the NE-SW, parallel to the strike of the Capitan reef.

These fractures are commonly orientated parallel to the strike of the Capitan Reef Complex. Meaning the major direction of failure is perpendicular to the reef trend, which promotes mass shedding of reef material into the basin. The fractures themselves are mostly

filled with carbonate mud shortly after forming, and later cemented with a variety of carbonate cements. The fracture will remain unstable until the cementation processes is complete, starting at the edge and migrating and works inward (observed as the growth lines leading toward the middle in figure 19).

Seismic activity (Brushy Canyon seisimite), and presence of Neptunian fractures in the Capitan Reef (figure 19), the Middle Rader mega-breccia is determined to be the result of a mass reef failure during a low sea level time (Hornbuckle, 2017; Lawson, 1989). This failure displaced large boulders of previously lithified reefal material, along with an enormous volume of sand. The total energy of this slide was many magnitudes greater than the normal sediment gravity flows which occurred before and after. The small and typical gravity flows are recorded as the Lower and Upper Rader Member turbidite deposits.

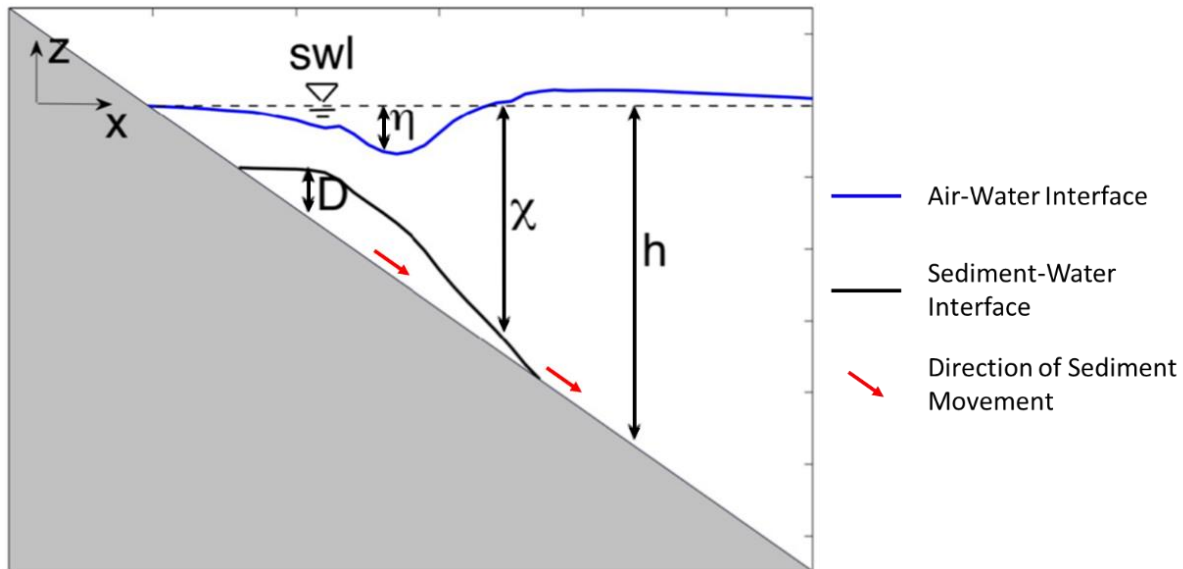


Figure 20. A comparison of the different variables that are accounted for when a portion of the basin breaks off and slides downward. As the sediment starts to move down a depression forms on the water surface directly above. In front of the slide water builds up and forms a long wave. Modified from (Grilli et al., 2017).

When a portion of the basin slope fails, it not only disturbs the subaqueous sediments, but the sudden movement of sediments can disturb the surface of the water. Figure 20 is a representation constructed by Jim Kirby (2016) describing the different dynamic variables occur during these landslides. As sediments start to move down slope, the water column is also pulled down (n) (as to avoid a vacuum developing between the top of the slide and the bottom of the water column). As the slide travels down the slope, the deeper water column is displaced causing it to rise, noted as being higher than the swl (still water level) in figure 20. This higher sea level will propagate outward from the source in all directions as a tsunami wave. A tsunami wave is defined as long water waves of small steepness generated by impulsive geophysical events on the ocean floor or at the coastline (Synolakis, 1987). As this wave propagates outward, the depression initially caused by the failing sediments rebounds and forms the maximum wave height. This large wave does not propagate like the initial wave does, rather diminished back to normality.

4.3 Depositional Processes of the Hummocky Cross Stratified (HCS) Beds

The Middle Rader mega-breccia was the result of the catastrophic failure of the Capitan Reef. However, the depositional processes of the hummocky cross stratified beds immediately above this mega-breccia is poorly understood. Previous analysis determined that the HCS beds were a result of turbidite flows and labeled as the “Bull Head Turbidite” (Hornbuckle, 2017; Lawson, 1989). Hummocky Cross Stratification (HCS) by itself does not point to a unique depositional environment or condition. There are three common processes that can result in these bedforms. 1) HCS beds can be indicative of shallow shelf storm deposits. The mixing of unidirectional and bidirectional flows (Weiss & Bahlburg, 2006). 2) HCS beds can be indicative

of deep-water sediment gravity flows (turbidites) (Mulder et al., 2009). 3) HCS beds can be indicative of upper flow regime bedforms (antidunes) (Middleton, 1965; Prave & Duke, 1990). In order to determine the correct processes of deposition, we first need to review the known depositional conditions:

- Boulders within the mega-breccia are composed of cemented reef fossils. Suggesting a subaqueous slide but inclusions contains trace amounts of subaerial-near surface indicators as determined by back reef inclusions from thin section.
- A paleo-water depth was interpreted to be a maximum of 900m and a minimum of 300m.
- The mega-breccia matrix contains a lack of shallow water fossils, while the boulders contain abundant shallow water fossils.
- No evidence of bioturbation within the HCS beds, or mega-breccia matrix.
- XRF proxies suggest anoxic to sub-oxic water conditions of the Lower, Middle, and Upper Rader Member.

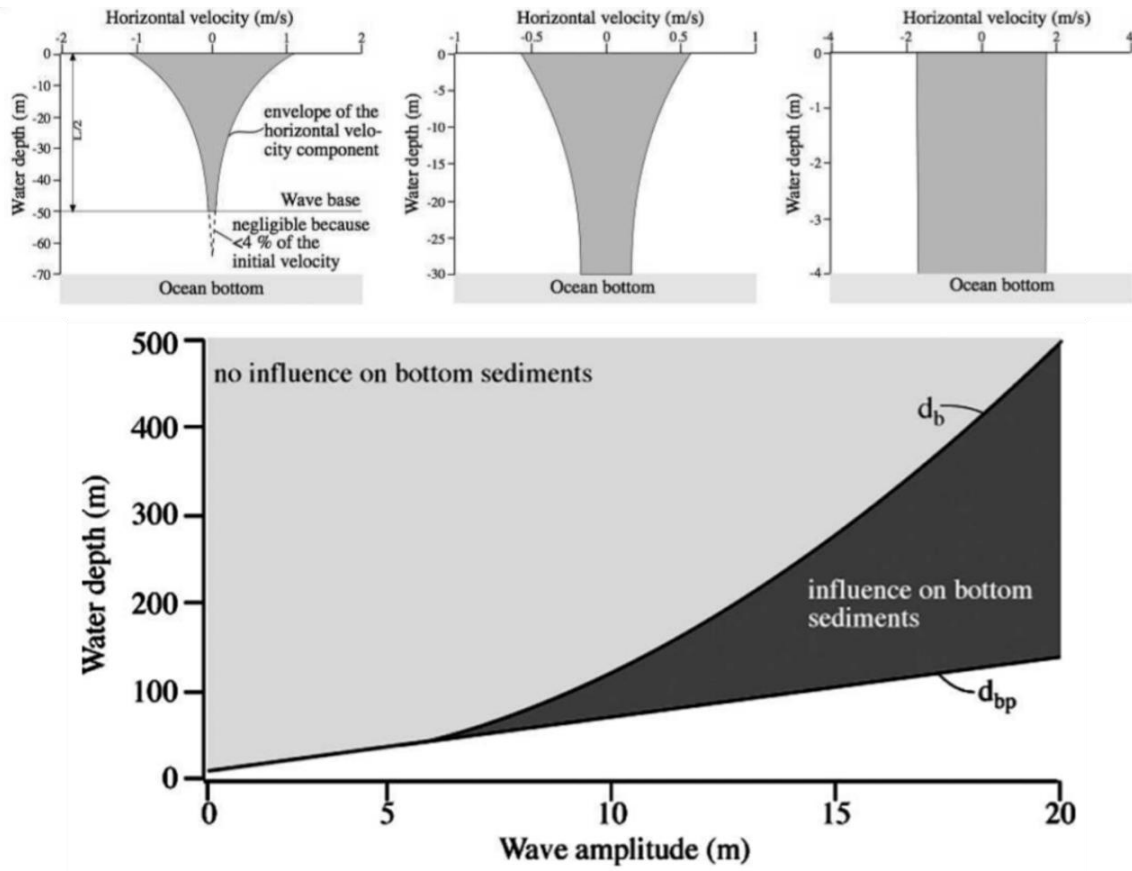


Figure 21. The upper three graphs show the decrease in a wave’s ability to disturb sediments on the ocean floor. The lower graph shows the wave amplitude required to agitate ocean floor sediments at increasing depths. To agitate sediments at 300m water depth, surface wave need to be stabilized at 15+m. (Weiss & Bahlburg, 2006).

The first possible processes for depositing the Middle Rader HCS beds is through storm agitation. Weiss and Bahlburg (2006) conducted a study on the decrease in horizontal velocity with increasing water depth. In shallow waters (0-4 meters), storm waves are able to disrupt sediments with no decrease in velocity vertically. When water depths were increased to intermediate depths (0-30 meters) the horizontal velocity noticeably decreased but was still able to disturb sediments at the ocean bottom. When the water depth was increased to 70 meters, deep-water, sediments only to 50m were agitated. This is known as the storm wave base (Weiss & Bahlburg, 2006). With increasing storm power (surface wave velocity, and wave height) sediments at deeper depths can be agitated, but only to a certain point. Following the trend of the

data storm waves in excess of 18 meters would need to be sustained in order to agitate sediments at 300+m of water (the depth of the Middle Rader HCS beds) (Weiss & Bahlburg, 2006). In recorded history the largest storm surge only reached 10.1 meters in height (Ali, 1999), discouraging the idea that the Middle Rader HCS beds were deposited by storm waves.

The second possible processes for depositing the Middle Rader HCS beds is through deep-water turbidite gravity flows. Through a 2009 study conducted by Thierry Mulder, examined a series of HCS-like deposits in Western Pyrenees, France. These deposits were from a paleowater-depth of 1,000+m and found exclusively within the Tc interval of a Bouma sequence (Mulder et al., 2009; Myrow, Fischer, & Goodge, 2002). Other requirements for these deep-water HCS deposits were that they are composed completely of fine-sand to silt-sized grains. Paleo-hydrologic conditions for these HCS-like deposition was interpreted to be a narrow window of low-energy (Mulder et al., 2009), owing to the lateral extent of these deposits being only a few decimeters.



Figure 22. The geomorphology of the Creek Bed showing the thickness of the individual Upper Rader Member Turbidite deposits. Each bed is roughly 5 to 10 cm thick. Photo taken by John Hornbuckle, 2016, and field book for scale.

Despite the Middle Rader hummocky beds being deposited in similar water depths to the HCS-like depots described by Mulder (2009), a number of other features did not match the constraints. These being (1) Middle Rader HCS beds contained clasts described in thin section and DGSA (3.2.2 and 3.2.5) being larger than the fine-sand to silt-size restriction described by Mulder. (2) That the Middle Rader HCS beds are laterally continuous and can be found in both proximal/distal locations, suggesting a much wider window of hydrological conditions. (3) The transition from the second Middle Rader HCS bed into the shale unit is a sharp contact, the deposits for turbidite flows would be expected to grade into this shale unit, transitioning from Bouma sequence Tc to Td to Te. (4) The vast majority of the Lower and Upper Rader Member

are made up of distal turbidites. These tend to be around 2-5cm in thickness and be composed of fine to silty sand grains. This composition is vastly different from what is found in the three hummocky beds and the numerous debrite deposits (figure 22).

Although not all of Mulder's (2009) findings are to be disregarded as possible deposition of the Middle Rader hummocky beds. As previously mentioned, when Froude number increases from 0 to 1.0, the observed bedforms change from lower flow regime planar beds to ripples to climbing ripples to sand waves and then to sand dunes. Once the Froude number is equal to 1, the upper flow regime planar beds take over. These water conditions are the transition from depositional waters ($Fr < 1.0$), where sediments can buildup, to erosive waters ($Fr > 1.0$), where the flow picks up and transports large amounts of sediment. Froude Numbers > 1.0 are able to destroy the underlying, and previously created bedforms. If the Froude Number continues to increase past 1.0, the bedforms transition into anti-dunes. These are dunes which propagate upstream (opposite direction as the flow) (Mulder et al., 2009). As the anti-dune generating Froude Number starts to decrease again, these bedforms will be eroded by the upper flow regime planar beds ($Fr = 1$). After the destruction by the upper planar beds, lower regime bedforms will occur once again, commonly removing all trace of their existence except for an erosive lower surface. In rare cases upper flow regime bedforms can be preserved. If water velocity were to decrease fast enough, the erosional processes will not have enough time to remove the anti-dune features (Prave & Duke, 1990).

Chapter 5: Numerical FUNWAVE-TVD

5.1 Construction of the Paleo-Bathymetry

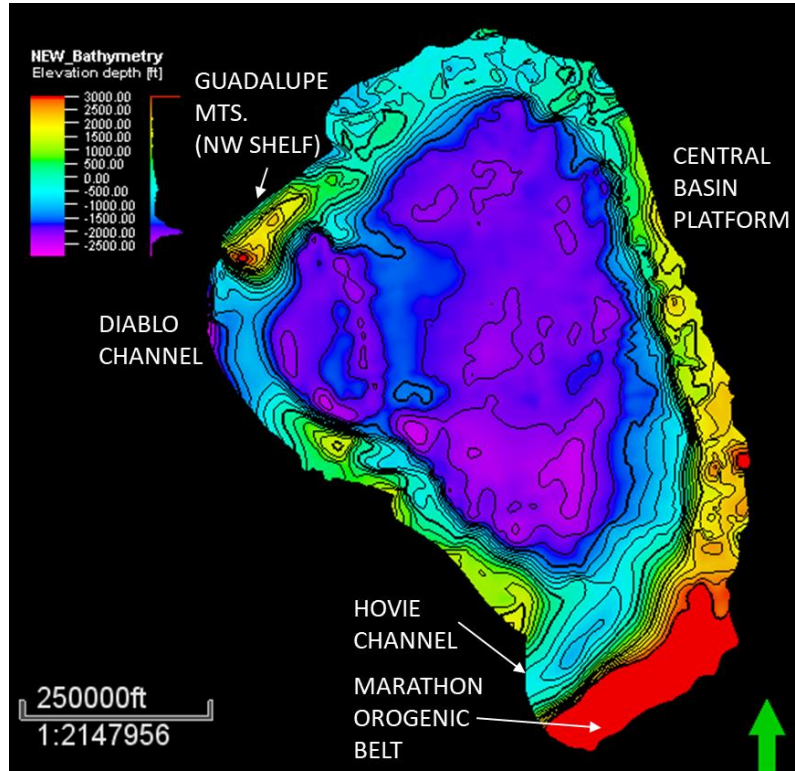


Figure 23. A reconstructed paleo-bathymetry of the Delaware Basin just before the deposition of the Middle Rader Member. The surface was shifted so that the 0-crossing (bold line) aligned with the projected sea level during the Late Guadalupian as indicated by fossil, XRF, and other methods. A maximum water depth is -822 m, and a maximum height is 914 m above sea level. The western depression is the Diablo channel, and the southwest depression is the Hovie channel. The southern Marathon Orogenic Belt was trimmed to 914 m to reduce unnecessary computing.

The reconstruction of the paleo-bathymetry surface during the Leonardian utilized a series of structural and isopach maps gathered from the Delaware Basin. The triangulation processes focused on correct alignment of Loving County and the Pecos River along the southern border. Structure maps showed the elevation/depth of the top of the Capitan reef, and were taken from the Texas Water Development Board “*Capitan Reef Complex Structure and Stratigraphy*”

(Standen, Finch, Williams, Lee-Brand, & Kirby, 2009). Although this isn't the exact reef from which the Middle Rader Member deposits were sourced, the latest Capitan Reef still serves as a good proxy for the bathymetric profile. For the Bell Canyon Sands (deeper/interior parts of the basin), both structure and isopach maps were taken from Scholle (2007).

After triangulation, the contours were digitized in PETREL to generate a 3-dimensional surface. During the digitization processes a few key assumptions were made. (1) No folds or fault offset was accounted for. (2) The removal of sediments due to weathering (erosion) was disregarded. (3) The basin contained a uniform dip. (4) The basin was decompacted uniformly.

To correct for the tectonic uplift of the basin, a wedge with a 5° dip to the east was subtracted from the modern bathymetry surface (Scholle et al., 2007). This subtraction removed the tectonic uplift and flattened the basin to its original orientation while still maintaining the internal structures.

After the tectonic correction, isopach maps of the upper two Bell Canyon sub-members were subtracted from the Bathymetry surface (Lamar and McCombs), each isopach removing approximately 30-45 meters of sediment. Once both sub-members were removed the top of the target layer was achieved (top of the Middle Rader Member). The isopach maps by Scholle (2007) showed the known Middle Rader slide to the northwest portions of the basin, but also show a second slide in the eastern edge of the basin. This second slide is entirely subsurface, so no field measurements are possible. Due to this, both the known/measured northwestern slide, and the subsurface eastern slide was assumed to be compositionally identical and treated as separate events.

The paleo-bathymetry surface was compared to both the modern Guadalupe Mountains and known Late Guadalupian features to determine its accuracy. Brown and Loucks (1993)

observed that the slope of the Capitan Reef Complex decreased basinward. The upper slope ranges from 55°-37°, the lower slope 37°-12°, and the toe of slope 9°-2° (Brown and Loucks, 1993). These slopes, along with their distances from the reef crest closely matched the reconstructed Delaware Basin. Figure 23 shows the position of the key geological features (e.g. the Hovey Channel, Diablo Channel, Central Basin Platform).

5.2 Static Modeling and Volumetrics of the Final Middle Rader Slides

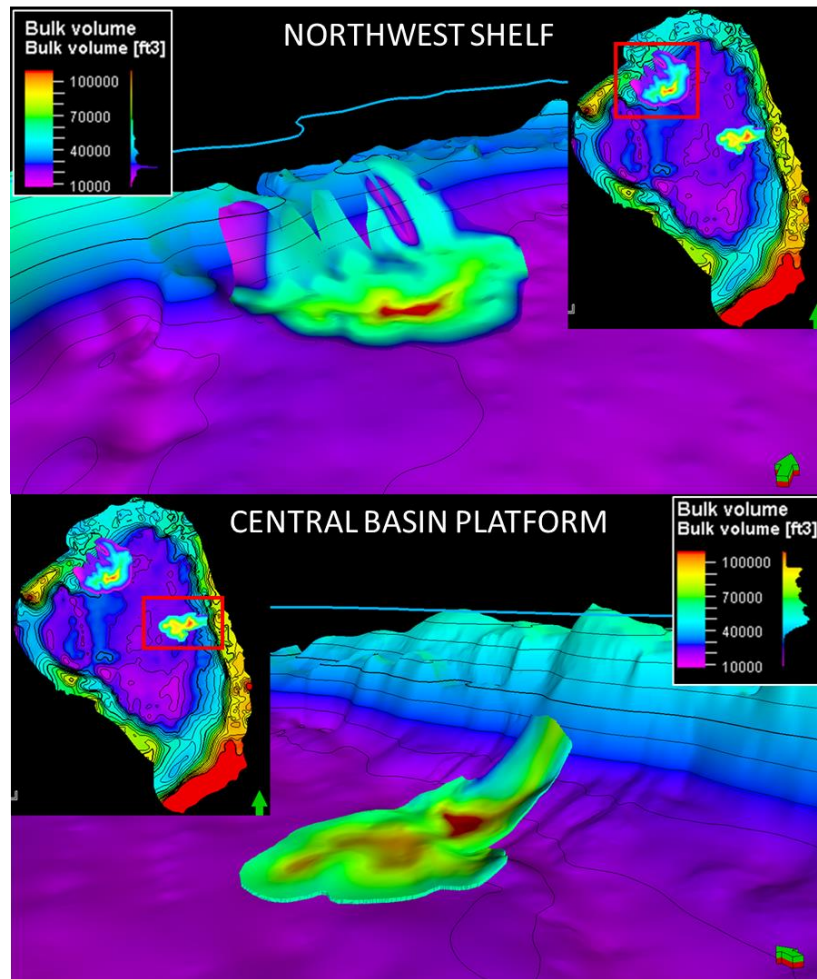


Figure 24. The upper image is a PETREL model of the northwestern shelf slide (exposed Middle Rader Member) colored with the bulk volume of the deposit. The lower image is a PETREL model of the eastern CBP slide (subsurface Middle Rader Member) colored with the bulk volume of the deposit. Both slides have a core of sediment at the contact between the slope and toe of the basin.

A PETREL model of the two flows was generated after reconstructing the paleo-bathymetric surface. This model utilized only areas containing sufficient data to digitize. This method of data exclusion produced the abrupt truncation of the deposit causing the volumes to be smaller than reality. A grid size of 250x250 feet was used as the areal coverage, and 100 internal layers were generated between the top and bottom surfaces (32.1 million cells in the NW Flow [figure 24 upper], and 12.8 million cells in East Flow [figure 24 lower]).

Before finalization of the flow volumes, both slides were decompacted assess their original volume and thickness before overlying strata compacted these deposits. The values for modern depth, volume, height, and width were taken from the original PETREL models. The modern porosity is 5% (Lawson, 1989). The height and volumes were decompacted by assuming an original porosity of 43%, based on assuming the flows are composed of 1/9 reefal material, and 8/9 sand/mud matrix. The reefal material is assigned an original porosity of 30% and the matrix contained 45% original porosity (Perry, 2016). This resulted in an original total porosity of 43% before compaction and was equated by:

$$(6) \quad Z_y = \frac{Z_t(1 - \phi_t)}{(1 - \phi_y)}$$

Z_t is the thickness of the modern strata, ϕ_t is the observed porosity the modern strata, ϕ_y is the predicted initial porosity, and Z_y is the decompacted thickness (Personal communication with Dr. Pigott). For a full list of the final slide volumetrics examine table 6.

Table 6. The various dimensions for the northwest and eastern slides. Additional inputs are listed in Appendix A.

	NW Flow	East Flow
Height (m)	Zt = 22m Decompacted = 36.66m	Zt = 32m Decompacted = 53.33m
Width (m)	54194m	27329m
Length (m)	46091m	44796m
Slope (deg)	Reef- 40° Basin- 5-7°	Reef- 40° Basin- 5-7°
Outrun Angle (deg)	-180°	-180°
Volume (km ³)	Vt = 34.37km ³ Decompacted = 57.28km ³	Vt = 23.84km ³ Decompacted = 54.73km ³
Terminal Velocity (m/s)	36.71	36.71

5.3 FUNWAVE-TVD Background/Introduction

FUNWAVE-TVD (Total Variation Diminish) is an open source, Unix-based, fully nonlinear code for modeling and simulating surface waves within a controlled computer environment. FUNWAVE is based on an underlying Boussinesq wave equation. The equation was originally developed by Joseph Boussinesq in 1872 to approximate the movements of water waves with no sediment incorporated, an ideal situation of one density (FUNWAVE-TVD workshop, 2018). Since then, the FUNWAVE developers have incorporated the addition of different densities of sediments as well as a dynamic dispersion term. The TVD adaption of the program enables the total variation of the wave energy to not increase over time (kinetically or potentially) (FUNWAVE-TVD workshop, 2018). For a more in-depth explanation of the source code and theory of development, reference *'FUNWAVE-TVD Fully Nonlinear Boussinesq Wave Model with TVD Solver Documentation and User's Manual (Version 3.0)'*.

The majority of the two Middle Rader Member slides were modeled by Dr. Fengyan Shi at the University of Delaware and Center for Applied Coastal Research. As one of the

developers, Dr. Shi's expertise and skill using FUNWAVE-TVD to model the wave propagation allowed for highly accurate, and realistic simulations of these catastrophic events. The running and processing of the models used a High-Performance Computing (HPC) cluster at the University of Delaware, the *mills* computer. Running on a total of 256 processors to generate the wave propagation for both the Northwest and Eastern shelves. To improve realistic accuracy, a spherical based code was implemented instead of the normal Cartesian based code. The spherical code, in short, incorporates the curvature of the Earth when propagating a wave over vast distances, while the Cartesian based waves uses an idealistic flat earth model (typically used for smaller scale experiments and idealistic experiments) (FUNWAVE-TVD workshop, 2018).

For the modeling of the landslide, NHWAVE, was used (a branch of FUNWAVE which models sediment landslides instead of fluids). The two programs accounted for a variety of parameters: depth from the still water level (swl) to the starting bathymetry surface, the depth from the swl to the top of the slide sediment water interface, the depth-averaged horizontal velocity vector, horizontal gradient, dynamic viscosity, density of sediment and water, gravity, and the manning coefficient for the slide-substrate bottom friction (Grilli et al., 2017) (figure 20).

5.4 Inputs and Validations for the Dynamic FUNWAVE-TVD Model

1) Water Depth

Two paleowater depths were estimated, one for the average depth of the Capitan Reef Complex, and one at the top of the Middle Rader Member slide. An estimation that the average depth of the Capitan Reef was 85 meters below sea level during the Late Guadalupian (Hunt, Fitchen, & Kosa, 2003). This water depth aligns with the known photic zone needed to sustain reef growth (Burgi et al., 1988). Newell, (1973) estimated a

water depth of the Rader Member to be 500m deep 2 km from the rim of the shelf. Yet, there is no definitive conclusion on the paleowater depth of the top of the Rader Member. Though some authors project that it was >300m deep (Adams 1937; King, 1948; Lawson, 1989). To examine this further, modern field observations placed the basin deposits at approximately 914 m deep. This was taken from measuring the elevation of the road cut deposits and the elevation of the nearby Capitan Reef plus 50-85m. To validate these measurements several modern examples were studied as well: the Great Barrier Reef, and the Caribbean. Both locations have a difference in relief of roughly 1520-1820m, and a water depth of <1219 m. A final water depth was placed at 400m above the top of the Rader slide.

2) Density

To properly model the relationship between sediment and water properties, a correct understanding of the densities must be determined. There are three different materials which need to be considered; reef, sands, and the sea water. The Capitan Reef Complex is predominately of calcitic and dolomitic minerals (J. E. Adams, 1965). To aid with the simplification of modeling the reef, it was assumed to be completely composed of calcite. Calcite is known to have a mineral density of 2.71 (Messineo, 1989). The second material to be determined was the sand grains. Being composed of dominantly quartz, a grain density of 2.65 was used (Messineo, 1989). However, these sand grains have not yet lithified into sandstones, and are still loosely sitting on the ocean floor. Each individual grain has a density of 2.65, but the sand body as a whole has a density closer to 1.93 (Messineo, 1989). The final member to be considered is the density of the sea water. A

typical 1.025 was used since it provided an average of different sea water (Messineo, 1989).

3) Out-Run Angle

Out-run angle determines if the flows were constricted or free to move according to the bathymetry and gravitational inputs. An angle of -180° was assigned to the two slides.

This indicates that the flows are completely unrestricted and are flowing perfectly out of the channel. (Schnyder et al., 2016)

4) Froude Number

As mentioned in previous sections, anti-dunes are capable of forming at $Fr > 1.0$.

However, a study conducted by Poos, (2011), suggested that anti-dunes are capable of forming at Froude numbers as low as 0.84. For the modeling, a buffer was added to examine the location and depths of Froude numbers as low as 0.84.

5) Porosity

This porosity was taken by examining thin section and outcrop composition to determine the sand to carbonate ratio. By assuming the flows are composed of 1/9 reefal material, and 8/9 sand to mud a more accurate general porosity can be made. The reefal material having an original porosity of 30% and the sands having 45% original porosity (Perry, 2016). This resulted in an original total porosity of 43% before compaction and was equated by (eq 6).

For additional input values see Appendix A.

5.5 Static Modeling and Volumetrics of the Starting Middle Rader Slides

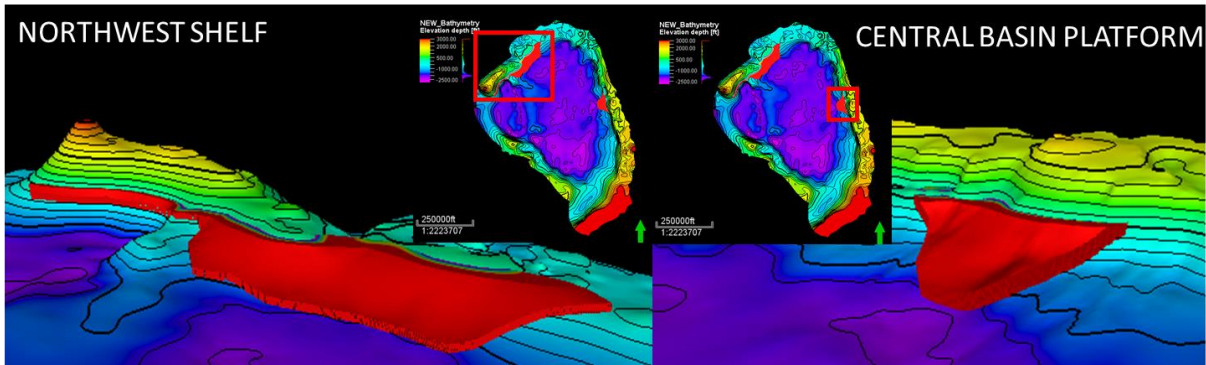


Figure 25. A PETREL reconstruction of the starting Middle Rader Member slides for both the northwestern shelf (upper) and eastern CBP (lower) portion of the basin. Both proximal flat regions are at an elevation of 25m. The shape of the starting slide locations was structured to resemble the final slide isopach thicknesses (figure 24).

The majority of the model volumetrics were taken from the two PETREL 3D models. Figure 25 shows the hypothesized starting locations of the two slides. These were mostly generated from copying the bathymetry floor of the region and elevating it up to a certain point. To aid in realism, a flat cutoff was inserted 25m (~80ft) above sea level. This prevented sediments from originating greater than 25 meters inland. The x-y area of each starting spoon was then sculpted to show a realistic starting shape while still retaining the same volume and distributions of the decompacted debris flows (Table 6). These starting locations were used as inputs for the NHWAVE modeling to determine how the sediments flowed down the slope.

5.6 Model Interpretations

All models were generated in a series of time slices through FUNWAVE-TVD. A postprocessing script in MATLAB was used to visualize and generate the different movies/images shown below. The majority of the scripts were written by The University of Delaware Center for Applied Coastal Research alongside the US Army Core of Engineers.

5.6.1 Northwest Slide

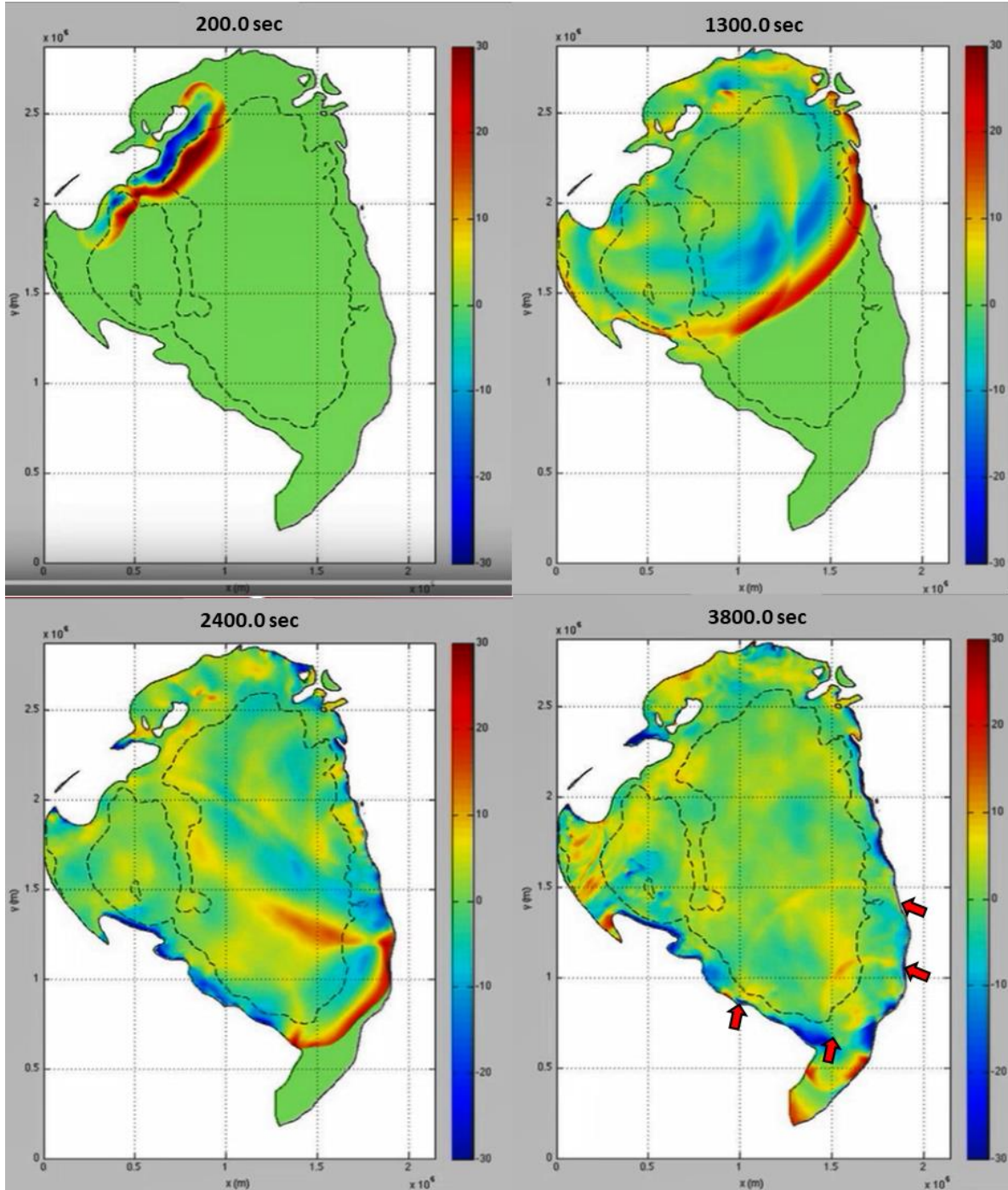


Figure 26. Four images of the propagation of the northwestern tsunami. The top left image shows the initial wave, the blue is the n from figure 25 and the red is the front wave. The top right image is from 1300 seconds (21 minutes), lower left from 2400 seconds (40 minutes), and the lower right at 3800 seconds (63 minutes). The red arrows on the lower right image show two reflection waves traveling in the opposite direction of the first wave. These smaller waves are only up to 10m tall.

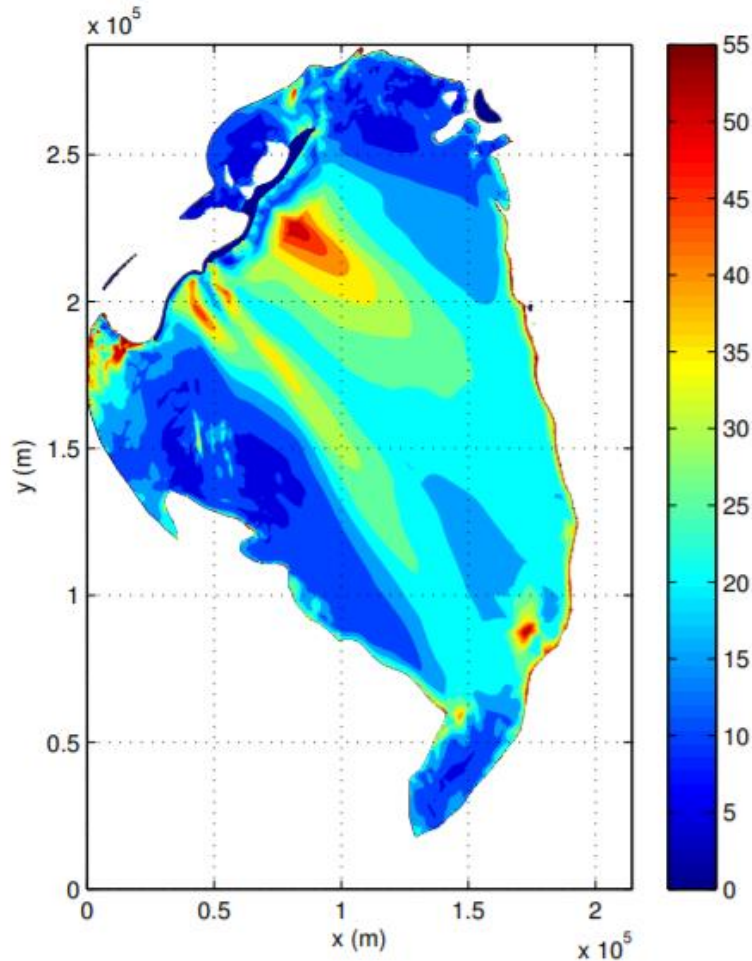


Figure 27. The maximum wave height of the tsunami generated from the northwest slide. The highest waves are located at the epicenter of the failure. The large waves in the southeast corner of the basin are a result of the rebound waves observed in figure 30.

The northwest slide contained 57.28 km^3 of sediment flowing into the basin with the core located just east of the Guadalupe Mountains. This failure resulted in the propagation of a solitary wave 30m tall and diminishing to 20m in height at the opposite side of the basin. The wave traveled at approximately 82m/s across the majority of the basin. The coast line slowed the velocity down, but maximum current speeds were in excesses of 45m/s. Four times are shown in figure 26 (200, 1300, 2400, and 3800 seconds). The hotter colors indicate growth of the water from the swl (still water level) and cooler colors being the depression caused by the slide, n in

figure 20. When the slide first fails, a depression is formed which then propels the 30m lead wave. The depression is then filled in and rebounds to form the maximum wave height of 55m. This wave does not propagate like the lead wave, rather just disperses and forms a series of small waves. The tsunami takes roughly 40 minutes to reach the opposite side of the Delaware Basin. Along the eastern and western coasts of the basin, the wave sweeps across which dampens its ability to run-up onto the shore. The maximum run-up wave would occur directly behind the failure or at the southeast (opposite) coast of the basin. Once the wave makes contact with the southern coast, two (possibly three) small rebound waves, each no more than 10 meters propagate back toward the northwest. These are indicated by the red arrows in the 3800 second time image of figure 26.

The maximum wave height, figure 27, shows that the tallest waves occur along the coast line and at the core of the slide. An odd pocket of tall waves is located in the northwest “bay”. This is likely not an actual feature but a result of the design of the basin creating an artificial harbor resonance. Defined as the forced oscillation of a confined water body connected to a larger water body (Martinez & Naverac, 1988). Higher waves in the southeast are a result of the rebounding waves indicated by the lower right of figure 26. The wave heights tend to be more dominant the closer they are to being parallel to the direction of slide failure (southeast direction). Run-up waves along shore are in excess of 40 meters in height, which would have caused massive amounts of destruction and potentially cause other portions of the shelf to become unstable and collapse.

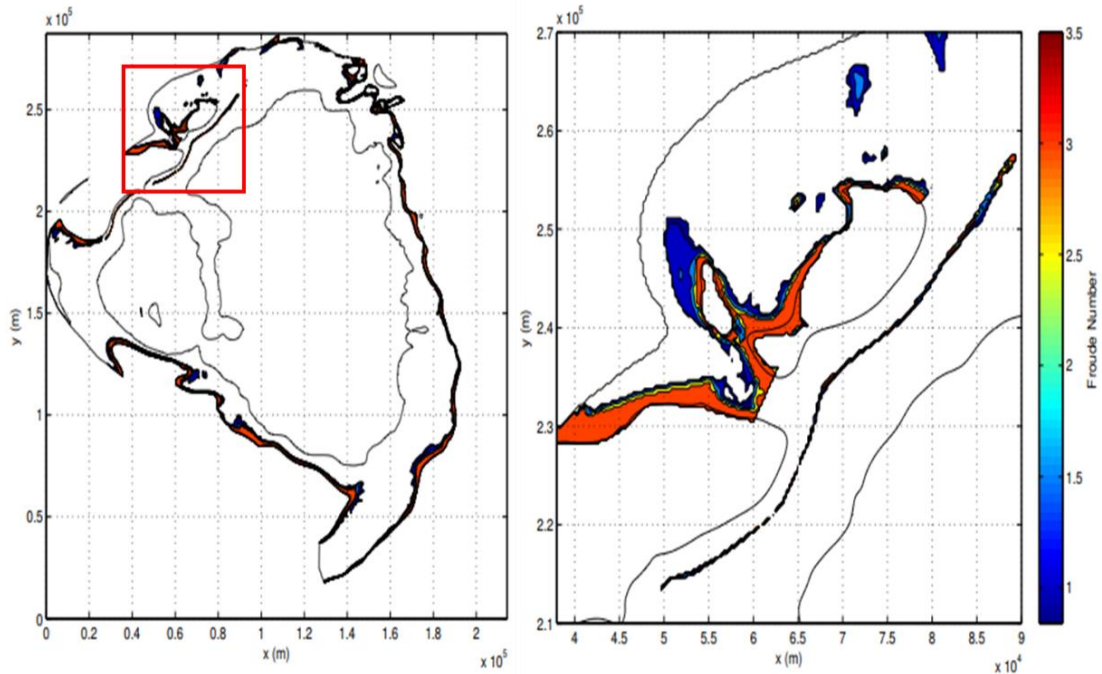


Figure 28. The location of Froude number greater than 0.84. The depth of these readings ranging from 0 to -300m. The right image is a close up behind the epicenter of the failure. Froude numbers are found to increase with decreasing water depth and reaching a maximum of 3.5.

While a majority of the sediments in the deeper portions of the basin remain undisturbed, the solidary wave disturbs sediments proximal to the coast. Froude numbers >0.84 line the basin and extend downward to water depths of 250 meters. As the water depth shallows, the Froude numbers increase up to 3.5 in the shallower regions. As stated in section 1.1 Froude numbers >1.0 enable the deposition of anti-dunes, and a study by Southard & Boguchwal, (1990), allows us to decrease this to 0.84. Thus, the detection of $Fr > 0.84$ at depths as low as 250m suggests that the Middle Rader HCS beds reflect anti-dune water conditions. The right half of figure 28 shows the distribution of Froude numbers directly behind the failure. The run-up wave is shown to encroach up the back side of the exposed portion of the basin. Though the distribution of the Fr is not very much, the depths at which they occur is more important.

5.6.2 Eastern Slide

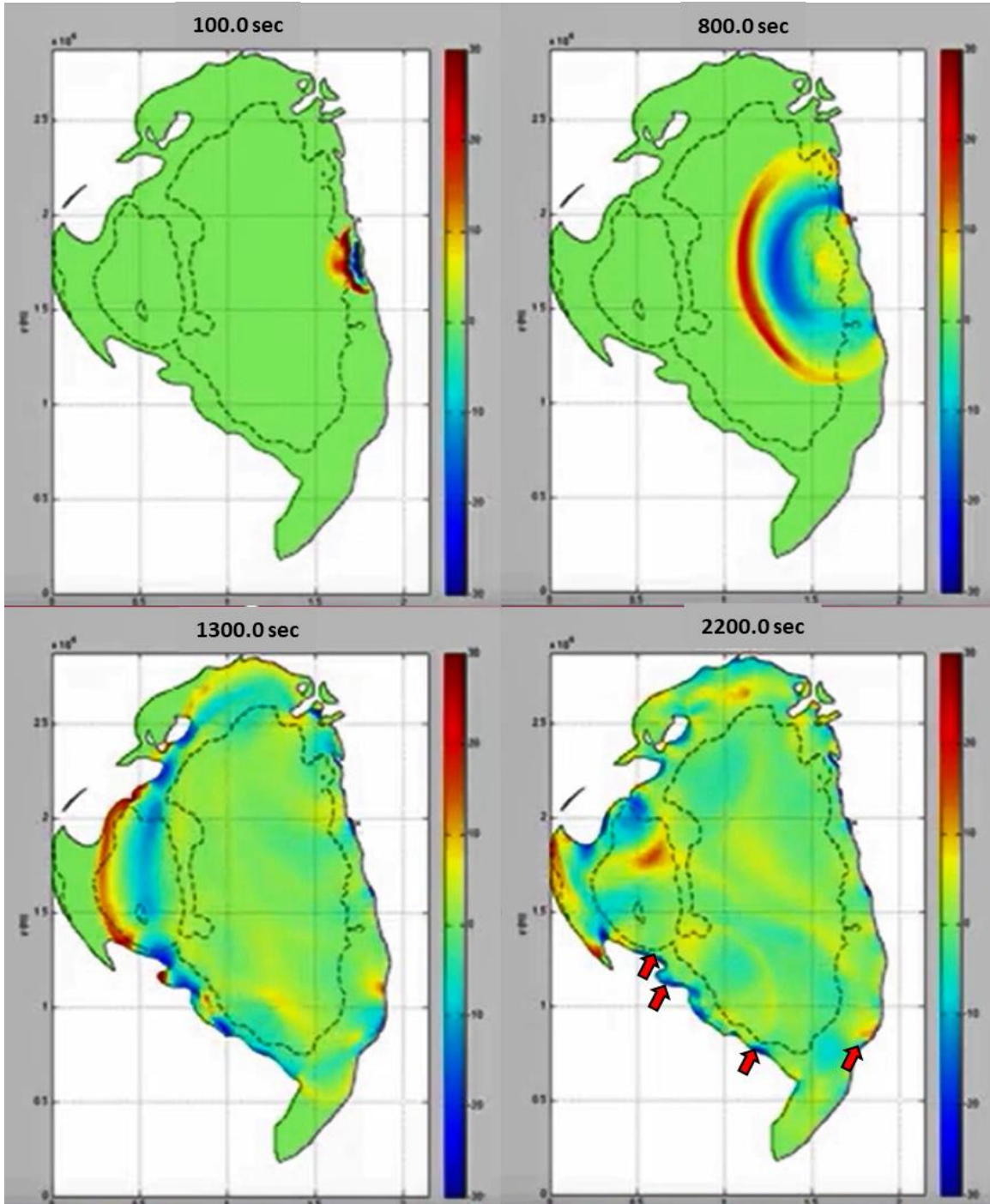


Figure 29. Four images of the propagation of the northwestern tsunami. The top left image shows the initial wave, the blue is the n from figure 25 and the red is the front wave. The top right image is from 800 seconds (13 minutes), lower left from 1300 seconds (21 minutes), and the lower right at 2200 seconds (36 minutes). The red arrows on the lower right image show two reflection waves traveling in the opposite direction of the first wave. These smaller waves are only up to 7m tall.

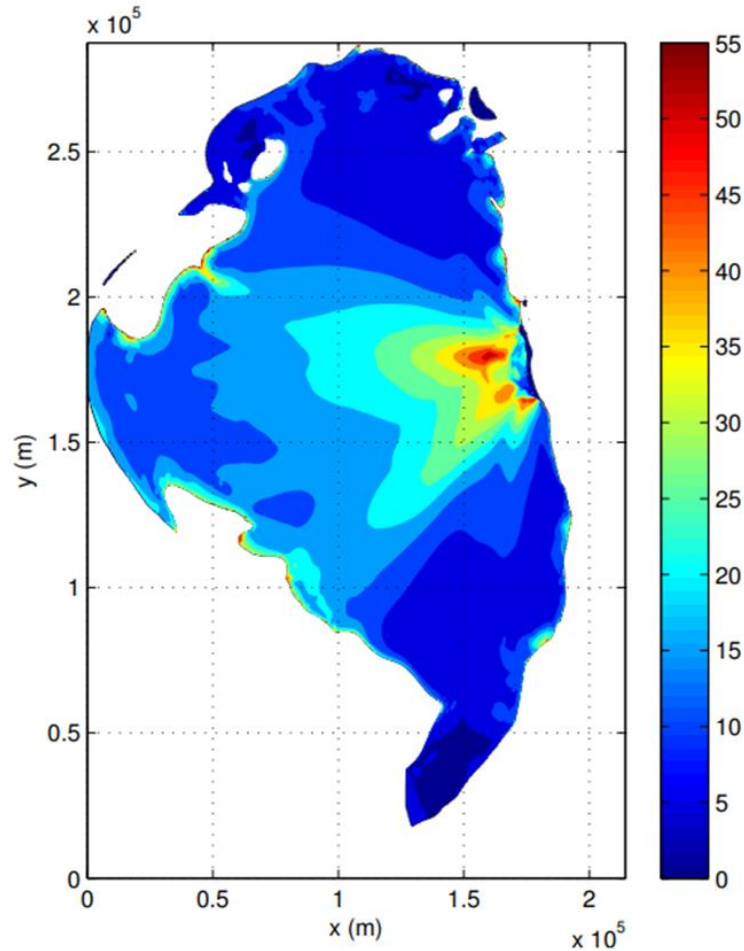


Figure 30. The maximum wave height of the eastern slide. The tallest waves are found at the epicenter of the failure. along the opposite coast the wave height increases as the water shallows.

The eastern flow is the simpler of the two slides owing to its location and relative shape of the final/starting slides. Smaller than the northwestern slide, only 39.73 km^3 of sediment, the eastern slide appeared to be more focused as the debris entered the basin, potentially only originating from one channel (figure 24 lower). From figure 29, the falling sediment can be seen to create a depression/void of water initially which is immediately infilled by a 55-meter wave. Similar to the northwestern wave, it is not this rebound that propagates to form the tsunami wave, rather the long wave generated by the push-up of the sliding sediment that becomes the

lead wave and propagates outward in all direction. The wave contains similar properties to the northwester wave, traveling at roughly 185mph in the open ocean, and diminishing in wave height as it propagates westward. The wave takes 2200.0 seconds (36.6 minutes) for it to reach the western portion of the basin. Only two rebound waves are observed to travel from the western coast, indicated by the red arrows in the lower right of figure 29. The height of this wave is less than 10 meters. Due to the shape of the basin, being wider in the north south direction, the lead tsunami wave has more room to expand in circumference which causes a decrease in its energy. By the time the tsunami wave reaches the western coast it has already lost a majority of its energy and does not run-up as far.

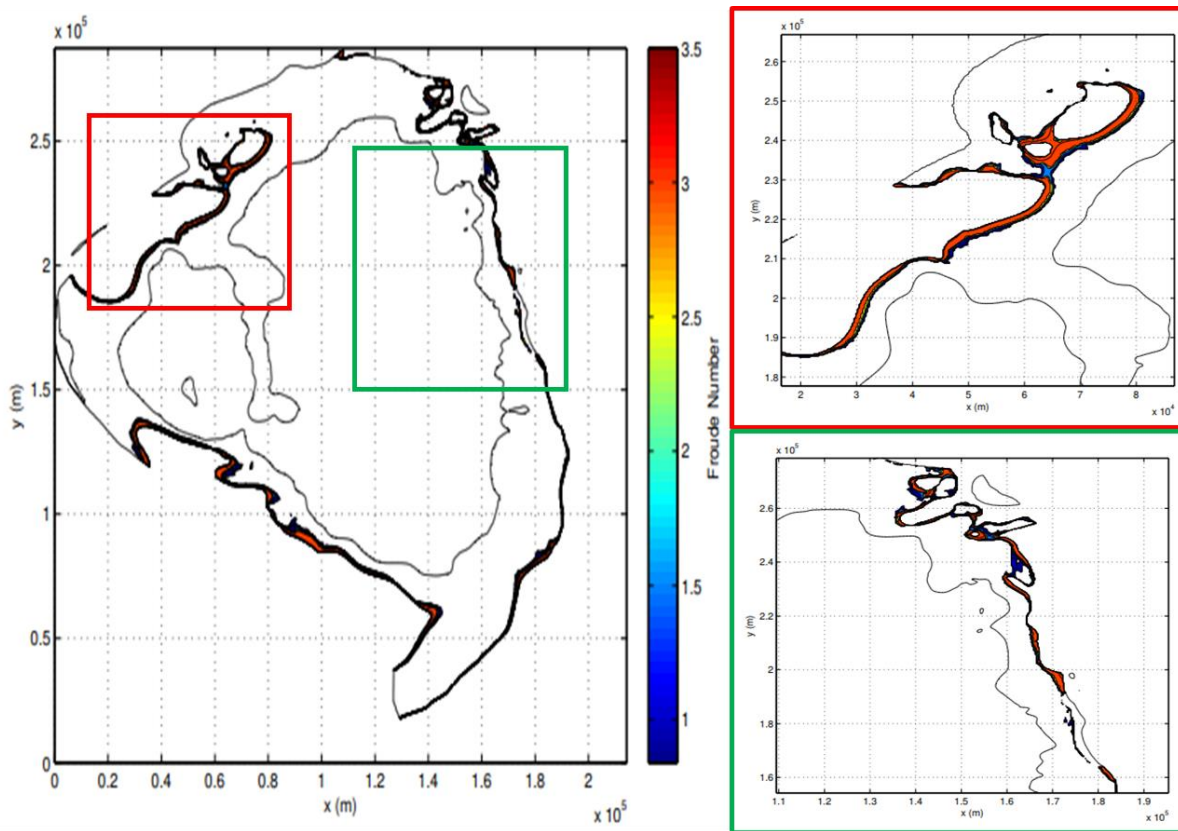


Figure 31. The location of Froude number greater than 0.84. The depth of these measurements ranged from 0 to -300m. The upper right image is a close up of the northwest coast, and flooding is observed over the island and Froude number up to 3.5 are found. The lower right image is a close up behind the epicenter of the failure. Froude numbers are found to increase with decreasing water depth and reaching a maximum of 3.5 as well.

Location and values of the Froude numbers mimic those produced by the northwest slide. Again, Froude numbers greater than 0.84 can be observed at water depths greater than 250 meters and increase as waters shallow. The western inlet of the basin does not show any Froude numbers >0.84 . This is because the tsunami wave lost its energy as it traveled this distance. As stated above, though the distance is less than the northwest slide, the ability to expand to the north and south stretched the energy of the tsunami causing it to have less energy per meter.

5.7 Runup Deposit

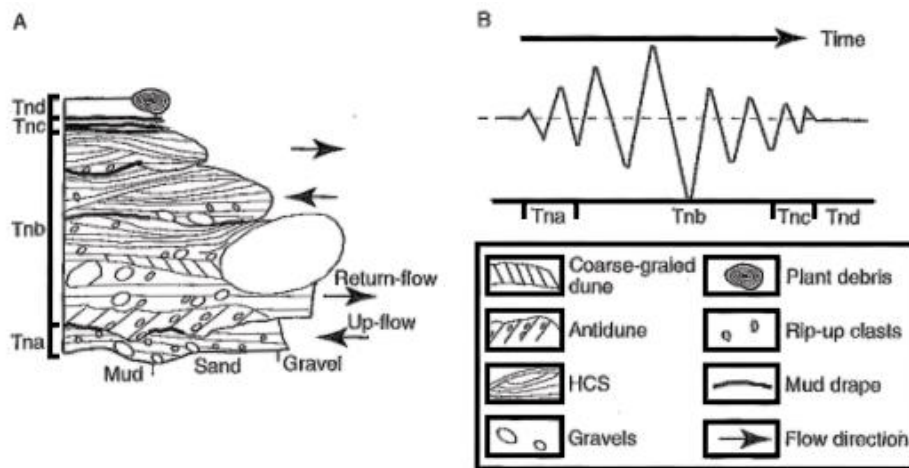


Figure 32. An ideal model for the tsunami run-up deposit by (Shiki, Yamazaki, & Minoura, 2009). The Tna interval represents the first run-up wave going onshore, commonly having an erosional surface at the base. The Tnb section being the subsequent back-flow (return-flow) of sediment rich waters returning to the ocean. The Tnc and Tnd units being the slow down periods where the finer material settles out of suspension and form a thin bed.

Tsunami waves deposit their sediments in two ways, the up-flow (run-up), when the wave propagates onto the land, and the return-flow (back-flow), when the wave velocity is halted by gravity and the slope and returns to the sea. This run-up deposit was described by Clague & Bobrowsky, 1993 as “having a sheet-like morphology, moderately well sorted, generally

massive, sharply bounded at the top and bottom and ranging in thickness from a few millimeters to 0.3m”, this deposit is depicted as *Tna* in figure 32. The figure shows the internal features commonly found and the order of sediments within an ideal tsunami deposit. Other researchers describe these deposits containing a mixture of land and ocean biota. Commonly these deposits can be found far inland, in some cases 3-4 miles (Dawson & Shi, 2000). Dawson and Shi conducted a study which compared modern tsunami run-up deposits on the US western coast to ancient deposits in Scotland and Norway. The tsunami surges carried fine grained sands up to 0.75km inland despite the waters being unable to disturb or erode the underlying marsh sediments (Dawson & Shi, 2000). The ancient tsunami deposits were described as “layers consisting of a gray micaceous silty fine sand that frequently occurs as a tapering wedge of sediment that rises in altitude inland... The deposit generally rests upon an erosional surface... this stratigraphic unconformity is marked by rip-up structures and the incorporation of many intraclasts of eroded material within the sediment wedge.” (Dawson & Shi, 2000).

Although these run-up deposits can be identified, their location and thickness cannot be used to determine the upper limits of the tsunami wave (Dawson & Shi, 2000). This is where the FUNWAVE-TVD and other studies model the upper limits of the run-up wave with changes in tsunami height and slope angle. Synolakis (1987) modeled the wave run-up by tsunamis. By using a plane sloping beach with differing angles, the maximum run-up could be measured for a simple case due to the removal of topography. The experiment produced near perfect solitary waves with a tail that did not exceed 2% of the wave height (Synolakis, 1987). Conclusions of the study found that solitary waves with longer wave amplitudes were measured further inland while shorter wave amplitudes did not run-up as far. As to be expected the lower the slope of the beach the further the solitary wave would be able to propagate inland.

As for the Middle Rader Member slides, evidence for the run-up deposits has yet to be entertained. Through FUNWAVE-TVD modeling these tsunamiites should be observable within the Yates and other back reef formations. From the scale of the tsunami waves generated the onshore deposits would be approximately at a minimum 5-10cm thick and contain numerous reef/carbonate biota while the surrounding strata would lack these fossils and contain terrigenous biota.

Chapter 6: Petroleum Indications and Analog Reservoirs

The petroleum potential of t mass transport complexes has been detailed by Hornbuckle (2017). For the Middle Rader Member shows a high potential for being an excellent hydrocarbon reservoir in the subsurface for several reasons. (1) The grains of the matrix are fairly well sorted and contain roughly 5% porosity. (2) Hydrocarbons have stained portions of the matrix and show migration pathways. (3) The HCS beds above the mega-breccia have minimal porosity, and fracturing. (4) Lower formations are known sources for hydrocarbon production (Bone Springs). Other mass failure deposits have proven to be excellent producers elsewhere in the basin.

The Mescalero Escarpe field is a very productive Bone Springs equivalent breccia located on the northern slope edge of the Delaware Basin. The field was deposited by a series of “shedding” events where the reef became unstable and deposited large boulders/clasts in the deeper part of the basin (Saller, Barton, & Barton, 2012). With each sheading event the reservoir interval of the field thickened, resulting in 30 meters at the thickest. Differing from the Rader Member, with each event in the Mescalero field an amalgamation surface or boundary layer can be observed in core, while the Rader mega-breccia is one massive unit. Core studies show that

the Mescalero field contains an average porosity of 5.1% and a permeability of 2mD (BEG). While pockets of up to 14% porosity are present (Saller et al., 2012).

Similar carbonate submarine fans have shown to be excellent hydrocarbon reservoirs (Shen, Farid, & Mcpeek, 2008). The eastern flow studied is in alignment with the Twofreds oil field located at the southern edge of Loving county. Since its discovery in 1957 the Twofreds field has produced 15.2 million barrels of oil and 12.7 billion cubic feet of gas (Flanders & DePauw, 1993). This field was described to be located stratigraphily in the middle of the Bell Canyon Sands (Flanders & DePauw, 1993), could be the current producer of the eastern Middle Rader Member slide.

Chapter 7. Conclusions

The Rader Member was deposited as an accumulation of distal turbidite gravity flows with exception of the Middle Rader Member. This abnormal unit was the result of episodic/catastrophic sedimentation due to reef instability. Through outcrop investigation and numerical modeling, the following conclusions can be made with reasonable certainty:

1. Paleo-water depths of the observable Rader ranged from 300 to 900 meters, while portions of the reef were at a depth of 85 meters.
2. Redox proxies from XRF suggest anoxic to sub-oxic water condition. This would enable the preservation of any organic material that would have entered the zone through sediment flows.
3. The Rader Member was deposited during a time of sea level low stand. This resulted in the deposition of small turbidite deposits forming the Lower and Upper Rader Members. Elevated seismic activity due to the proximity of a major orogenic zone provided a

possible trigger for the catastrophic failure of the Capitan Reef. This failure resulted in the large sediment slide that is the Middle Rader mega-breccia.

4. The catastrophic sedimentation of the mega-breccia provided favorable anti-dune forming conditions. These flow conditions resulted in the three HCS beds above the mega-breccia. The resulting tsunami wave showed an ability to agitate sediments as low as 300m of water depth, confirming that the HCS beds are directly linked to the mega-breccia, and not a separate event.
5. The lower most HCS bed is the result of the initial run-up wave caused by the tsunami, while the second HCS bed is caused by the returning-flow, commonly carrying sediments from onshore. The thin shale separating the third HCS bed suggests that there was a brief period of calm before the third HCS bed was deposited. This bed possibly could be the result of a separate failure elsewhere in the basin, potentially initiated by the collision of the first tsunami wave.
6. HCS beds found at water depths greater than 300m are not formed by storm waves, rather by tsunami or other large solitary waves.

References

- Adams, J. B., & Filice, A. L. (1967). Spectral reflectance 0.4 to 2.0 microns of silicate rock powders. *Journal of Geophysical Research*, 72(22), 5705–5715. <https://doi.org/10.1029/JZ072i022p05705>
- Adams, J. E. (1965). Stratigraphic-Tectonic Development of Delaware Basin, 49, 2140–2148.
- Algeo, T. J. (2004). Can marine anoxic events draw down the trace element inventory of seawater? *Geology*, 32(12), 1057–1060. <https://doi.org/10.1130/G20896.1>
- Algeo, T. J., & Rowe, H. (2012). Paleooceanographic applications of trace-metal concentration data. *Chemical Geology*, 324–325, 6–18. <https://doi.org/10.1016/j.chemgeo.2011.09.002>
- Ali, A. (1999). Climate Change Impacts and Adaptaion Assessment in Bangladesh. *Climate Research*, 109–116. <https://doi.org/10.5296/jpag.v8i1.12648>
- Blakey, R. T. (2013). Paleogeography and Geologic Evolution of North America. Retrieved from <http://cpgeosystems.com/gloaltex2.html>
- Brown, A. A., & Loucks, R. G. (1993). Influence of sediment type and depositional processes on stratal patterns in the Permian Basin-margin Lamar Limestone, McKittrick Canyon, Texas. *AAPG MEMOIRS 57: Carbonate Sequence Stratigraphy: Recent Developments and Applications*, (unit 2), 133–156.
- Burgi, L., Jeandupeux, O., Hirstein, A., Brune, H., Kern, K., Yoon, H. S., ... Jin, Y. (1988). Photic Zone Euxinia During the Permian-Triassic Superanoxic Event. *Phys. Rev. Lett*, 87(9), 4898. <https://doi.org/10.1126/science.1106911>
- Burton, D., Dunlap, D. B., Wood, L. J., & Flaig, P. P. (2011). LiDAR Intensity as a Remote Sensor of Rock Properties. *Journal of Sedimentary Research*, 81(5), 339–347. <https://doi.org/10.2110/jsr.2011.31>
- Buscombe, D. (2013). Transferable wavelet method for grain-size distribution from images of sediment surfaces and thin sections, and other natural granular patterns. *Sedimentology*, 60(7), 1709–1732. <https://doi.org/10.1111/sed.12049>
- Chanson, H. (2004). *Hydraulics of Open Channel Flow: An Introduction (2nd Edition)*.
- Clague, J. J., & Bobrowsky, P. T. (1993). Evidence for a Large Earthquake and Tsunami 100-400 Years Ago on Western Vancouver Island, British Columbia. *Quaternary Research*, 41, 176–184.
- Crosby, C. (2015). *Depositional History and High-Resolution Sequence Stratigraphy of the Leonardian Bone Spring Formation, Northern Delaware Basin, Eddy and Lea Counties, New Mexico*. Oklahoma.
- Dawson, A. G., & Shi, S. (2000). Tsunami deposits. *Pure and Applied Geophysics*, 157(6–8), 875–897. <https://doi.org/10.1007/s000240050010>
- Deer, W. A., Howie, R. A., & Zussman, J. (2013). *Rock-Forming Minerals*.

- Fall, L. M., & Olszewski, T. D. (2010). Environmental Disruptions Influence Taxonomic Composition of Brachiopod Paleocommunities in the Middle Permian Bell Canyon Formation (Delaware Basin, West Texas). *Palaios*, 25(4), 247–259. <https://doi.org/10.2110/palo.2009.p09-091r>
- Fischer, A. G., & Sarnthein, M. (1988). Airborne silts and dune-derived sands in the Permian of the Delaware Basin. *Journal of Sedimentary Research*, 58, 637–643.
- Flanders, W. A., & DePauw, R. M. (1993). Updated case history: performance of the Twofreds Tertiary CO2 project. *Society of Petroleum Engineers Annual Technical Conference: Society of Petroleum Engineers*, (26614), 10.
- Folk, R. L. (1974). Petrologie of sedimentary rocks. *Hemphill Publishing Company, Austin*, 170. <https://doi.org/10.1017/CBO9781107415324.004>
- Galloway, W. E. (1989). Genetic stratigraphic sequence in basin analysis II Application to northwest Gulf of Mexico Cenozoic basin, 2(2).
- Garrett, K. (2015). *High Resolution Basin Modeling of the Permian Capitan Reef, New Mexico: New Insight from Integrated Outcrop LiDAR-XRF-SGR Analysis into Reef Architecture*. Oklahoma.
- Giddens, E. (2016). *Pleistocene Coral Reef Destruction in the Florida Keys: Paleotempestite Evidence from a High Resolution LiDAR XRF Analysis of Windley Key Quarry, FL*.
- Grilli, S. T., Shelby, M., Kimmoun, O., Dupont, G., Nicolsky, D., Ma, G., ... Shi, F. (2017). Modeling coastal tsunami hazard from submarine mass failures: effect of slide rheology, experimental validation, and case studies off the US East Coast. *Natural Hazards*, 86(1), 353–391. <https://doi.org/10.1007/s11069-016-2692-3>
- Haq, B. U., & Schutter, S. R. (2008). A chronology of paleozoic sea-level changes. *Science*, 322(5898), 64–68. <https://doi.org/10.1126/science.1161648>
- Hills, J. M. (1984). Sedimentation, Tectonism, and Hydrocarbon Generation in Delaware Basin, West Texas and Southeastern New Mexico. *American Association of Petroleum Geologists Bulletin*, 68(3), 250–267. <https://doi.org/10.1306/AD460A08-16F7-11D7-8645000102C1865D>
- Hobbs, P. R. N., Gibson, A., Jones, L., Pennington, C., Jenkins, G., Pearson, S., & Freeborough, K. (2010). Monitoring coastal change using terrestrial LiDAR. *Geological Society, London, Special Publications*, 345(1), 117–127. <https://doi.org/10.1144/SP345.12>
- Hornbuckle, J. S. (2017). *Process Sedimentology of the Gueadalupian Rader Limestone, Delaware Basin*. Oklahoma.
- Hunt, D. W., Fitchen, W. M., & Kosa, E. (2003). Syndepositional deformation of the Permian Capitan reef carbonate platform, Guadalupe Mountains, New Mexico, USA. *Sedimentary Geology*, 154(3–4), 89–126. [https://doi.org/10.1016/S0037-0738\(02\)00104-5](https://doi.org/10.1016/S0037-0738(02)00104-5)
- Kerans, C., Fitchen, W. M., Gardner, M. H., Sonnenfeld, M. D., Tinker, S. W., & Wardlaw, B. R. (1992). Styles of sequence development within uppermost leonardian through guadalupian strata of the guadalipe mountains, texas and new mexico. *WTGS*.

- King, P. B. (1948). Geology of the southern Guadalupe Mountains, Texas. *U. S. Geological Survey Professional Paper*, (215), 183.
- Lawson, E. C. (1989). Subaqueous Gravity Flows and Associated Deposits in the Rader Member, Capitan Reef Complex (Permian), Delaware Mountains, West Texas, (806).
- Martinez, F. M., & Naverac, V. S. (1988). An Experimental Study of Harbour Resonance Phenomena. *Coastal Engineering*, 39(5), 270–280.
- Messineo, T. (1989). *Analyzing and Scanalizing Well Logs*.
- Middleton, G. V. (1965). Antidune cross-bedding in a large flume. *Journal of Sedimentary Research*, 35(4), 922–927. <https://doi.org/10.1306/74D713AC-2B21-11D7-8648000102C1865D>
- Mulder, T., Razin, P., & Faugeres, J. C. (2009). Hummocky cross-stratification-like structures in deep-sea turbidites: Upper Cretaceous Basque basins (Western Pyrenees, France). *Sedimentology*, 56(4), 997–1015. <https://doi.org/10.1111/j.1365-3091.2008.01014.x>
- Myrow, P. M., Fischer, W., & Goodge, J. W. (2002). Wave-Modified Turbidites: Combined-Flow Shoreline and Shelf Deposits, Cambrian, Antarctica. *Journal of Sedimentary Research*, 72(5), 641–656. <https://doi.org/10.1306/022102720641>
- Nance, H. S. (2007). Middle Permian basinal siliciclastic deposition in the Delaware Basin: the Delaware Mountain Group (Guadalupian). *Thesis*, 80pp.
- Nance, H. S., & Rowe, H. (2015). Eustatic controls on stratigraphy, chemostratigraphy, and water mass evolution preserved in a Lower Permian mudrock succession, Delaware Basin, west Texas, USA. *Interpretation*, 3(1), SH11-SH25. <https://doi.org/10.1190/INT-2014-0207.1>
- Nicklen, B. L. (2011). *Establishing a Tephrochronologic Framework for the Middle Permian (Guadalupian) Type Area and Adjacent Portions of the Delaware Basin and Northwestern Shelf, West Texas and Southeastern New Mexico, USA*. Cincinnati.
- Nicklen, B. L., Bell, G. L. J., & Huff, W. D. (2015). A new shelf-to-basin timeline for the Middle Permian (Guadalupian) Capitan depositional system, west Texas and southeastern New Mexico, USA. *Stratigraphy*, 12(2), 109–122.
- Osleger, D. A., & Tinker, S. W. (2012). Three-dimensional architecture of upper permian high-frequency sequences, yates-capitan shelf margin, permian basin, U.S.A. *Society of Economic Paleontologists and Mineralogists (SEPM)*.
- Perry, C. T. (2016). Reef Framework Preservation in Four Contrasting Modern Reef Environments , Discovery Bay , Jamaica, 15(3), 796–812.
- Pigott, K. L., Pigott, J. D., Engel, M. H., & Philp, R. P. (2007). High resolution chemical stratigraphy in carbonates: Oxfordian Smackover USA ramp proxy. *AAPG International Convention and Exhibition*.
- Poos, W. J. R. (2011). *Stability Diagram of upper flow regime bedforms . An experimental study*.
- Prave, A. R., & Duke, W. L. (1990). Small-scale hummocky cross-stratification in turbidites: a

form of antidune stratification? *Sedimentology*, 37(3), 531–539.
<https://doi.org/10.1111/j.1365-3091.1990.tb00152.x>

RIEGL. (2012). *RIEGL Laser Instrument Systems Glossary*.

RIEGL. (2013). *RIEGL Laser Instrument Systems VZ-400 Technical Documentation and Users Instructions*.

Sageman, B. B., & Lyons, T. W. (2003). Geochemistry of Fine-grained Sediments and Sedimentary Rocks. *Treatise on Geochemistry*, 7–9, 115–158. <https://doi.org/10.1016/B0-08-043751-6/07157-7>

Saller, A. (2013). Sequence Stratigraphy of Classic Carbonate Outcrops in West Texas and Southeast New Mexico and Application to Subsurface Reservoirs *, 50846.

Saller, A., Barton, J., & Barton, R. (2012). Slope Sediment Associated with a Vertically Building Shelf, Bone Spring Formation, Mescalero Escarpe Field, Southeastern New Mexico. *Society of Economic Paleontologists and Mineralogists (SEPM)*, 44, 275–288.

Sarg, J. F. (1988). *Carbonate sequence stratigraphy. Sea level changes - an integrated approach* (Vol. 42). <https://doi.org/10.2110/pec.88.01.0155>

Schnyder, J. S. D., Eberli, G. P., Kirby, J. T., Shi, F., Tehranirad, B., Mulder, T., ... Wintersteller, P. (2016). Tsunamis caused by submarine slope failures along western Great Bahama Bank. *Scientific Reports*, 6, 1–9. <https://doi.org/10.1038/srep35925>

Scholle, P. A., Goldstein, R. H., & Ulmer-scholle, D. S. (2007). Classic Upper Paleozoic Reefs and Bioherms of West Texas and New Mexico, 1–171.

Shen, L., Farid, H., & Mcpeek, M. A. (2008). Carbonate Apron models: Alternatives to the Submarine Fan Model for Paleoenvironmental Analysis and Hydrocarbon Exploration. *Evolution*, 48, 1–14.

Shiki, T., Yamazaki, T., & Minoura, K. (2009). Introduction: Why a Book on Tsunamiites. *Amsterdam: Elsevier*.

Southard, J. B., & Boguchwal, L. A. (1990). Bed Configurations in Steady Unidirectional Water Flows. Part 2. Synthesis of Flume Data. *Sedimentary Petrology*, 60(5), 658–679.

Standen, A., Finch, S., Williams, R., Lee-Brand, B., & Kirby, P. (2009). Capitan Reef Complex Structure and Stratigraphy. *Texas Water Development Board*, (0804830794), 1–52.

Synolakis, C. E. (1987). The runup of solitary waves. *Journal of Fluid Mechanics*, 185, 523–545. <https://doi.org/10.1017/S002211208700329X>

Tang, C. M. (2015). Permian Basin. Retrieved from <https://www.britannica.com/place/Permian-Basin>

ThermoFisher. (2010). *User's Guide Version 7.0.1*.

Tinker, S. W. (1998). Shelf-To-Basin Facies Distributions and Sequence Stratigraphy of a Steep-Rimmed Carbonate Margin; Capitan Depositional System, McKittrick Canyon, New Mexico and Texas. *Journal of Sedimentary Research*, 68(6), 1146–1174.

<https://doi.org/10.2110/jsr.68.1146>

- Tribovillard, N., Algeo, T. J., Lyons, T. W., & Riboulleau, A. (2006). Trace metals as paleoredox and paleoproductivity proxies: An update. *Chemical Geology*, 232(1–2), 12–32. <https://doi.org/10.1016/j.chemgeo.2006.02.012>
- Turner, B. W., Molinares-blanco, C. E., & Slatt, R. M. (2015). Chemostratigraphic, palynostratigraphic, and sequence stratigraphic analysis of the Woodford Shale, Wyche Farm Quarry, Pontotoc County, Oklahoma, 3(1), 1–9.
- Vail, P. R. (1987). Seismic Stratigraphy Interpretation Using Sequence Stratigraphy. *AAPG Studies in Geology #27, Volume 1: Atlas of Seismic Stratigraphy*, 1(1), 1–10. <https://doi.org/10.1016/j.gaceta.2012.07.008> [doi]
- van Rijn, L. (2018). Bedforms and Roughness. Retrieved from http://www.coastalwiki.org/wiki/Bedforms_and_roughness
- Weiss, R., & Bahlburg, H. (2006). A Note on the Preservation of Offshore Tsunami Deposits. *Journal of Sedimentary Research*, 76(12), 1267–1273. <https://doi.org/10.2110/jsr.2006.110>
- Wentworth, C. K. (1922). A Scale of Grade and Class Terms for Clastic Sediments. *The Journal of Geology*, 30(5), 377–392.
- Williams, M. T. (2013). *Evolution of the Delaware Basin, West Texas and Southeast New Mexico*. University of Oklahoma.
- Wilson, R. D., & Schieber, J. (2015). Sedimentary Facies and Depositional Environment of the Middle Devonian Genesee Formation of New York, U.S.A. *Journal of Sedimentary Research*, 85(11), 1393–1415. <https://doi.org/10.2110/jsr.2015.88>
- Yalcin, E. (2014). *Delaware Basin Thermal Evolution from Constrained Vitrinite Reflectance: Tectonic Versus Flexural Subsidence*. Oklahoma.

Appendix A

The following is a full list of inputs and parameters for NHWAVE | FUNWAVE-TVD modeling program. For a more in-depth explanation of the source code and theory of development, reference *'FUNWAVE-TVD Fully Nonlinear Boussinesq Wave Model with TVD Solver Documentation and User's Manual (Version 3.0)'*, and a link to the source code is here: <https://github.com/fengyanshi/FUNWAVE-TVD>.

! INPUT PARAMETERS FOR NHWAVE

TITLE = TEST_RUN

! -----DIMENSION-----

Mglob = 704

Nglob = 944

Kglob = 3

! -----PROCESSOR NUMBER-----

PX = 2

PY = 2

! -----TIME-----

SIM_STEPS = 100000000

TOTAL_TIME = 500.0

PLOT_START = 0.0

PLOT_INTV = 10.0

SCREEN_INTV = 1.0

! -----GRID-----

DX = 304.8

DY = 304.8

! -----VERTICAL GRID OPTION-----

IVGRD = 1

IVGRD = 1

! -----TIME STEP-----

DT_INI = 0.0100

DT_MIN = 0.00001

DT_MAX = 60.0000

! -----BATHYMETRY-----

DEPTH_TYPE = CELL_CENTER


```

ANA_BATHY = F
DEPTH_FILE = ../data/depth_4x.txt

!-----NUMERICS-----
HIGH_ORDER = SECOND
TIME_ORDER = SECOND

!-----BOTTOM ROUGHNESS-----
Ibot = 1
Ibot = 2
Ibot = 2
Cd0 = 0.00
Zob = 0.0

!-----NON-HYDRO-----
NON_HYDRO = T

!-----COURANT_NUMBER-----
CFL = 0.5

!-----VISCOSITY-----
VISCOUS_FLOW = F
IVTURB = 10
IHTURB = 10
VISCOSITY = 1.e-6
Chs = 0.20
Cvs = 0.20

!-----VISCOUS NUMBER-----
VISCOUS_NUMBER = 0.1666667

!-----WET-DRY-----
MinDep = 0.10

!-----POISSON SOLVER-----
ISOLVER = 2 (Incomplete Cholesky GMRES)
ITMAX = 1000
TOL = 1.e-8

!-----PERIODIC BC-----
PERIODIC = F

!-----BOUNDARY_TYPE-----
BC_X0 = 1 (free slip)
BC_Xn = 1
BC_Y0 = 1

```

BC_Yn = 1
BC_Z0 = 1
BC_Zn = 1

!-----WAVEMAKER-----

WAVEMAKER = nothing
BoundaryFile = boundary.txt
Nudging = F
AMP = 1.0
PER = 10.0
DEP = 10.0
THETA = 0.0

!-----INTERNAL WAVEMAKER-----

Xsource_West = 30.0
Xsource_East = 35.0
Ysource_Suth = 0.0
Ysource_Nrth = 100.0

!----- SPONGE LAYER -----

SPONGE_ON = F

!-----PROBE OUTPUT-----

NSTAT = 0
PLOT_INTV_STAT = 0.01

!----- LANDSLIDE PARAMETERS -----

H_slide = 34.0
L_slide = 600.0
W_slide = 400.0
e_slide = 0.717 (parameter e in Enet and Grilli)
Angle_slide = 10.0
X0_slide = 950.0
Y0_slide = 8650.0
Slope_slide = 14.0
TermV_slide = 36.71 (calculated using Enet and Grilli)

!-----DEFORMABLE SLIDE-----

SLIDE_FILE = ../data/slide_4x_nw.txt
SLIDE_DENSITY = 1980.0 kg/m³
! Kinematic viscosity (Jiang's Ph.D. Thesis, p. 29)
! River coastal mud = 0.002-0.2 m²/s
! Mudslide and debris flows = 0.2-0.6 m²/s
SLIDE_VISCOSITY = .035
! Manning's coefficient for the viscous slide
SLIDE_ROUGHNESS = 0.05

! A tiny diffusivity for the mass equation
SLIDE_DIFF = 0.10
! The minimum slide thickness, m
SLIDE_MINTHICK = 0.0001

! -----OUTPUT-----
! (water depth)
OUT_H = T
! (surface elevation)
OUT_E = T
! (velocity in x direction)
OUT_U = T
! (velocity in y direction)
OUT_V = T
! (velocity in z direction)
OUT_W = T
! (dynamic pressure)
OUT_P = F
! (turbulent kinetic energy)
OUT_K = F
! (turbulent dissipation rate)
OUT_D = F
! (shear production)
OUT_S = F
! (eddy viscosity)
OUT_C = F
! (bubble void fraction)
OUT_B = F
OUT_2DUV = F
OUT_preview = F